

2009

Synthesis, characterization, and application of surface-functionalized ordered mesoporous nanoparticles

Po-wen Chung
Iowa State University

Follow this and additional works at: <https://lib.dr.iastate.edu/etd>

 Part of the [Chemistry Commons](#)

Recommended Citation

Chung, Po-wen, "Synthesis, characterization, and application of surface-functionalized ordered mesoporous nanoparticles" (2009).
Graduate Theses and Dissertations. 11075.
<https://lib.dr.iastate.edu/etd/11075>

This Dissertation is brought to you for free and open access by the Iowa State University Capstones, Theses and Dissertations at Iowa State University Digital Repository. It has been accepted for inclusion in Graduate Theses and Dissertations by an authorized administrator of Iowa State University Digital Repository. For more information, please contact digirep@iastate.edu.

Synthesis, characterization, and application of surface-functionalized ordered mesoporous nanoparticles

by

Po-Wen Chung

A dissertation submitted to the graduate faculty
in partial fulfillment of the requirements for the degree of
DOCTOR OF PHILOSOPHY

Major: Chemistry

Program of Study Committee:
Victor Shang-Yi Lin, Major Professor
George Kraus
Marek Pruski
Matthew Kramer
Aaron Sadow

Iowa State University

Ames, Iowa

2009

Copyright © Po-Wen Chung, 2009. All rights reserved.

TABLE OF CONTENTS

CHAPTER 1. GENERAL INTRODUCTION	1
Dissertation Organization	1
Introduction	2
References	7
CHAPTER 2. TEMPERATURE RESPONSIVE SOLUTION PARTITION OF ORGANIC-INORGANIC HYBRID POLY(N-ISOPROPYLACRYLAMIDE)-COATED MESOPOROUS SILICA NANOSPHERE	8
Abstract	8
1. Introduction	9
2. Results and discussion	11
2.1. Synthesis of PNiPAm-MSN	11
2.2. Solid-state NMR study of PNiPAm-MSNs	12
2.3. Powder X-ray diffraction patterns of PNiPAm-MSN	18
2.4. Nitrogen sorption properties of PNiPAm-MSNs	19
2.5. Transmission electron microscopy study of PNiPAm-MSNs	21
2.6. Temperature-responsive partition study of PNiPAm-MSNs	22
2.7. Thermogravimetric analysis study of PNiPAm-MSNs	24
2.8. Dynamic light scattering study of PNiPAm-MSNs	25
3. Conclusions	26
4. Experimental	27
Reference	31
CHAPTER 3. STRUCTURALLY ORDERED MESOPOROUS CARBON NANOPARTICLES AS TRANSMEMBRANE DELIVERY VEHICLE IN HUMAN CANCER CELLS	33
Abstract	33
Results and discussions	34
Acknowledgment	39
Reference	39
Supporting Information	47
Experimental Section	47
CHAPTER 4. ORDERED MESOPOROUS CARBON NANOPARTICLES AS A SUPPORT FOR THE CONVERSION OF SYNGAS TO ALCOHOL	53
Abstract	53
Introduction	54
Results and Discussion	56
Conclusion	62
Experimental	62
Preparations of Materials	62
Preparation of Catalytic Reaction	64
General Characterization	65
References	74
CHAPTER 5. FACILE SYNTHESIS OF MONODISPERSED SPHERICAL MCM-48 MESOPOROUS SILICA NANOPARTICLES WITH CONTROLLED PARTICLE SIZE	75

Abstract	75
1. Introduction	76
2. Experimental	78
2.1. Preparation of MCM-48	78
2.2. Preparation of metal oxide nanoparticles	79
2.3. Characterization	80
3. Results and discussion	81
3.1. Effect of CTAB concentration, stirring rate and time	81
3.2. Effect of F127 as a dispersion agent	86
3.3. Pore size control	89
3.4. Mesoporous metal oxide nanoparticles	92
4. Conclusions	94
References	95
Supporting Information	110
CHAPTER 6. GENERAL CONCLUSIONS	122
ACKNOWLEDGEMENTS	125

CHAPTER 1. GENERAL INTRODUCTION

Dissertation Organization

The dissertation begins with Chapter 1, which is a general introduction of the fundamental synthesis of mesoporous silica materials, the selective functionalization of mesoporous silica materials, and the synthesis of nanostructured porous materials via nanocasting. In Chapter 2, the thermo-responsive polymer coated mesoporous silica nanoparticles (MSN) was synthesized via surface-initiated polymerization and exhibited unique partition activities in a biphasic solution with the thermally induced change. In Chapter 3, the monodispersed spherical MSN with different mesoporous structure (MCM-48) was developed and employed as a template for the synthesis of mesoporous carbon nanoparticles (MCN) via nanocasting. MCN was demonstrated for the delivery of membrane impermeable chemical agents inside the cells. The cellular uptake efficiency and biocompatibility of MCN with human cervical cancer cells were also investigated. In addition to the biocompatibility of MCN, MCN was demonstrated to support Rh-Mn nanoparticles for catalytic reaction in Chapter 4. Owing to the unique mesoporosity, Rh-Mn nanoparticles can be well distributed inside the mesoporous structure and exhibited interesting catalytic performance on CO hydrogenation. In Chapter 5, the synthesis route of the aforementioned MCM-48 MSN was discussed and investigated in details and other metal oxide nanoparticles were also developed via nanocasting by using MCM-48 MSN as a template. At last, there is a general conclusion summarized in Chapter 6.

Introduction

Recent progress in the synthesis of morphologically defined mesoporous silica materials, such as FSM-,^{1,2} MCM-^{3,4} and SBA-type silicas^{5,6} with high surface area ($> 900 \text{ m}^2/\text{g}$) and pore volume ($> 1 \text{ cm}^3/\text{g}$) has attracted much research attention on the utilization of these materials for selective absorption, separation, catalysis, delivery, and sensor applications.⁷⁻¹⁸ An upsurge began in 1992 with the development by the Mobil Oil Company of the class of periodic mesoporous silica known as M41S phase and the most well known representatives of this class include the silica solids MCM-41 (with a hexagonal arrangement of the mesopores, space group $p6mm$), MCM-48 (with a cubic arrangement of the mesopores, space group $Ia-3d$), and MCM-50 (with a laminar structure, space group $p2$). The use of supramolecular aggregates of ionic surfactants (long-chain alkyltrimethylammonium halides) as structure-directing agents (SDAs) was revolutionary in the synthesis of these materials. These SDAs, in the form of a lyotropic liquid-crystalline phase, lead to the assembly of an ordered mesostructured composite during the condensation of the silica precursors under basic conditions. The mesoporous materials are obtained by subsequent removal of the surfactant by extraction or calcination.

The investigations have found that two different mechanisms are involved.¹⁹ One is the liquid-crystal template pathway, the concentration is so high that under certain conditions (temperature, pH) a liquid-crystal phase is formed without the presence of inorganic precursor (generally tetraethyl- (TEOS) or tetramethylorthosilica (TMOS)). Then the condensation of inorganic precursors is improved owing to the confined growth around the surfactants and thus ceramic-like frameworks are formed. After the condensation, the organic templates can be removed by calcination or extraction. The inorganic materials cast the

mesostructures, pore sizes, and the symmetries from the liquid-crystal scaffolds. The other pathway is cooperative self-assembly of surfactant and silica source.²⁰ Silicate polyanions such as silicate oligomers interact with positively charged groups in cationic surfactants driven by Coulomb forces. The silicate species at the interface polymerize and cross-link and further change the charge density of the inorganic layers. The arrangements of surfactants and the charge density between inorganic and organic species influence each other with the proceeding of the condensation. Therefore the compositions of inorganic-organic hybrids differ to some degree. It is the matching of charge density at the organic/inorganic interfaces that governs the assembly process.

However, the original mesoporous silicates exhibited a number of limitations, including lower hydrothermal stability and lower reactivity than zeolites with comparable mesoporous silicates has been the incorporation of organic components, either selectively on the silicate surface, as part of the silicate walls, or trapped within the channels. Organic modification of the silicates permits precise control over the surface properties for specific application.²¹ In the past few years, mesoporous silica materials have been functionalized at specific sites, and were demonstrated to exhibit improved activity, selectivity, and stability in a large number of catalytic reactions and sorption processes. Two of the major pathways for functionalization of mesoporous silica materials are: 1) the subsequent modification on the pore surface of a purely inorganic silica materials (“grafting”), 2) the simultaneous condensation of corresponding silica and organosilica precursors (“co-condensation”).

Grafting refers to the subsequent modification of the inner surfaces of mesostructured silica phases with organic groups. This process is carried out primarily by reaction of organosilanes of the type $(R'O)_3SiR$, or less frequently chlorosilanes $ClSiR_3$, with the free

silanol groups of the pore surfaces. In principle, functionalization with a variety of organic groups can be immobilized in this way by variation of the organic residue R. This type of modification is advantageous of preserving the mesostructure of the starting silica phase during reaction, whereas the lining of the walls is compromised by a reduction in the porosity of the hybrid material.

An alternative method to functionalize mesoporous silica materials is so called co-condensation, meaning that tetraethyl- or tetramethylorthosilica (TEOS or TMOS) are co-condensed with terminal trialkoxyorganosilanes of the type $(R'O)_3SiR$ in the presence of structure-directing agents leading to materials with organic residues anchored covalently to the pore walls. Since the organic functionalities are direct components of the silica matrix, pore blocking is not a problem in the co-condensation method. Furthermore, the organic units are generally more homogeneously distributed than in materials synthesized with the grafting process. However, the co-condensation method also has a number of disadvantages. In general, the degree of mesoscopic order of the products decreases with increasing concentration of $(R'O)_3SiR$ in the reaction mixture, which ultimately leads to totally disordered products. Furthermore, the portion of terminal organic groups immobilized on the pore-wall network was generally lower than the starting concentration of the reaction mixture. These observations can be explained by the fact that an increasing proportion of $(R'O)_3SiR$ in the reaction mixture favors homocondensation reactions—at the cost of cross-linking co-condensation reactions with the silica precursors. The tendency towards homocondensation reactions, which is caused by the different hydrolysis and condensation rates of the structurally different precursors, is a constant problem in co-condensation

because the homogeneous distribution of different organic functionalities in the framework cannot be guaranteed.

However, the most spectacular works in the area of subsequent organic functionalization of silica phases was demonstrated by Mal et al.,^{22,23} who successfully functionalized the target organic moiety selectively on the pore openings of MCM-41 silica material. The construction strategy was to use as-synthesized MCM-41 in which the templates were still present. Therefore, the target functionality $(R'O)_3SiR$ can only react with the silanol groups around the pore opening and the exterior surface. Then the templates was removed by solvent extraction instead calcination to preserve the organic moieties on silica surface. The approach can allow the selective functionalization either on the exterior/interior surface of mesoporous silica materials and is exactly the way I demonstrated the selective functionalization in Chapter 2..

As aforementioned, MCM-48 is another well-defined porous material in M41S family and possesses a cubic structure indexed in the space group $Ia3d$. MCM-48 seems to be a more interesting candidate as an adsorbent in separation techniques and as a catalyst support than MCM-41. This is because of its interwoven and branched pore structure, which provides more favourable mass transfer kinetics in catalytic and separation application than MCM-41 with its unidirectional pore system.²⁴ In addition, MCM-48 can be used as a hard template for other nanostructured materials via nanocasting. In general, nanocasting involves three main steps: i) formation of the template ii) the casting step with target precursors, including the conversion of the precursor—which is typically molecular—to a solid; and iii) removal of the template.²⁵ In order to be able to control the morphology and structural parameters of the replicas, templates with a controllable morphology and structure are highly advantageous.

One of the most versatile hard templates is ordered mesoporous silica, since it can be prepared in different morphologies.

The successful synthesis of carbon with an ordered pore structure was first demonstrated by Ryoo's group in 1999, whereby MCM-48 was used as a template to create a carbon material (CMK-1).²⁶ Generally, the synthetic procedure for ordered mesoporous carbon (OMC) can be described as follows: Mesoporous silica with a specific structure (as a template) is impregnated with a carbon precursor(s) (including monomer and polymer) to give the desired composition. Subsequent polymerization (in some cases, curing or stabilization steps are needed) and carbonization of the precursor in the pore system result in a carbon-silica composite. Finally, a replica mesoporous carbon can be obtained after removing the silica template by HF or NaOH. Mesoporous carbon nanoparticles (MCN) and non-siliceous templated by MCM-48 nanoparticles were developed and discussed mainly in Chapter 3 and 5.

References

- (1) Yanagisawa, T.; Shimizu, T.; Kuroda, K.; Kato, C. *Bull. Chem. Soc. Jpn.* **1990**, *63*, 988-92.
- (2) Inagaki, S.; Fukushima, Y.; Kuroda, K. *J. Chem. Soc., Chem. Commun.* **1993**, 680-682.
- (3) Beck, J. S.; Vartuli, J. C.; Roth, W. J.; Leonowicz, M. E.; Kresge, C. T.; Schmitt, K. D.; Chu, C. T. W.; Olson, D. H.; Sheppard, E. W.; et al. *J. Am. Chem. Soc.* **1992**, *114*, 10834-10843.
- (4) Kresge, C. T.; Leonowicz, M. E.; Roth, W. J.; Vartuli, J. C.; Beck, J. S. *Nature (London, United Kingdom)* **1992**, *359*, 710-12.
- (5) Zhao, D. Y.; Feng, J. L.; Huo, Q. S.; Melosh, N.; Fredrickson, G. H.; Chmelka, B. F.; Stucky, G. D. *Science* **1998**, *279*, 548-552.
- (6) Zhao, D. Y.; Huo, Q. S.; Feng, J. L.; Chmelka, B. F.; Stucky, G. D. *J. Am. Chem. Soc.* **1998**, *120*, 6024-6036.
- (7) Lin, V. S. Y.; Lai, C.-Y.; Huang, J.; Song, S.-A.; Xu, S. *J. Am. Chem. Soc.* **2001**, *123*, 11510-11511.
- (8) Lai, C.-Y.; Trewyn, B. G.; Jęftinija, D. M.; Jęftinija, K.; Xu, S.; Jęftinija, S.; Lin, V. S. Y. *J. Am. Chem. Soc.* **2003**, *125*, 4451-4459.
- (9) Radu, D. R.; Lai, C.-Y.; Jęftinija, K.; Rowe, E. W.; Jęftinija, S.; Lin, V. S. Y. *J. Am. Chem. Soc.* **2004**, *126*, 13216-13217.
- (10) Ciesla, U.; Schuth, F. *Microporous Mesoporous Mater.* **1999**, *27*, 131-149.
- (11) Ying, J. Y. M., C. P.; Wong, M. S. *Angew. Chem. Int. Ed. Engl.* **1999**, *38*, 56.
- (12) Schüth, F. *Chem. Mater.* **2001**, *13*, 3184.
- (13) Scott, B. J. W., G.; Stucky, G. D. *Chem. Mater.* **2001**, *13*, 3140.
- (14) Schmidt, W. S., F. *Adv. Mater.* **2002**, *14*, 629.
- (15) Soler-Illia, G. J. A. A. P., J.; Lebeau, B.; Sanchez, C. *Chem. Rev.* **2002**, *102*, 4093.
- (16) Stein, A. A. M., 15, 763. *Adv. Mater.* **2003**, *15*, 763.
- (17) Sanchez, C. S.-I., G. J. A. A.; Ribot, F. G., D. S. C. R. *Chimie* **2003**, *6*, 1131. *Chimie* **2003**, *6*, 1131.
- (18) Taguchi, A. S., F. *Microporous Mesoporous Mater.* **2005**, *77*, 1.
- (19) Hoffmann, F.; Cornelius, M.; Morell, J.; Froba, M. *Angew. Chem. Int. Ed.* **2006**, *45*, 3216-3251.
- (20) Wan, Y.; Zhao, D. *Chem. Rev.* **2007**, *107*, 2821-2860.
- (21) A. Stein; B. J. Melde; R. C. Schrodin *Adv. Mater.* **2000**, *12*, 1403-1419.
- (22) Mal, N. K.; Fujiwara, M.; Tanaka, Y. *Nature* **2003**, *421*, 350-353.
- (23) Mal, N. K.; Fujiwara, M.; Tanaka, Y.; Taguchi, T.; Matsukata, M. *Chem. Mater.* **2003**, *15*, 3385-3394.
- (24) Schumacher, K.; Gr,n, M.; Unger, K. K. *Microporous Mesoporous Mater.* **1999**, *27*, 201-206.
- (25) Lu, A.-H.; Schuth, F. *Adv. Mater.* **2006**, *18*, 1793-1805.
- (26) Ryoo, R.; Joo, S. H.; Jun, S. *J. Phys. Chem. B* **1999**, *103*, 7743-7746.

CHAPTER 2. TEMPERATURE RESPONSIVE SOLUTION PARTITION OF ORGANIC-INORGANIC HYBRID POLY(N- ISOPROPYLACRYLAMIDE)-COATED MESOPOROUS SILICA NANOSPHERE

¹A paper published in *Advance Functional Materials*, **2008**, *18*, 1390-1398

*Po-Wen Chung*², *Rajeev Kumar*, *Marek Pruski*, and *Victor S.-Y. Lin*³

Abstract

A series of poly(*N*-isopropylacrylamide)-coated mesoporous silica nanoparticle materials (PNiPAm-MSNs) was synthesized via a surface-initiated living radical polymerization with a reversible addition-fragmentation chain transfer (RAFT) reaction. The structure and the degree of polymerization of the PNiPAm-MSN were characterized by a variety of techniques, including nitrogen sorption analysis, ²⁹Si and ¹³C solid-state NMR spectroscopy, transmission electron microscopy (TEM), and power X-ray diffraction (XRD). The thermally induced changes of surface properties of these polymer-coated core-shell nanoparticles were determined by examining their partition activities in a biphasic solution (water/toluene) at different temperatures.

¹ Reprinted with permission of Wiley-VCH Verlag GmbH & Co. KGaA, Weinheim

² Primary researcher and author

³ Author of correspondence

1. Introduction

Recent progress in the synthesis of morphologically defined mesoporous silica materials, such as FSM-^[1, 2] MCM-^[3, 4] and SBA-type silicas^[5, 6] with high surface area ($> 900 \text{ m}^2/\text{g}$) and pore volume ($> 1 \text{ cm}^3/\text{g}$) has attracted much research attention on the utilization of these materials for selective absorption, separation, catalysis, delivery, and sensor applications.^[7-18] An important prerequisite for the realization of these goals is to tune the surface properties of these mesoporous silica materials, so that the diffusion of different molecules in-and-out of the pores can be regulated. One promising approach is the selective functionalization of the exterior particle and/or interior pore surfaces of these structurally uniform materials with different organic functionalities that can modulate mass transport and pore penetration. Among the different inorganic-organic hybrid mesoporous nanodevices that have been reported,^[8, 19-26] polymer-coated, core-shell mesoporous silicas^[19, 27, 28] have shown some interesting and unique substrate selectivity that is difficult to achieve in other systems functionalized with only small organic moieties. For example, we have recently demonstrated that, by covalently anchoring a layer of poly(lactic acid) on the exterior surface of a mesoporous silica nanoparticle (MSN) sensor system,^[27] the polymer coating serves as a gatekeeping layer and controls the pore-penetration for selective detection of neurotransmitters.

While these recent breakthroughs bring exciting potential for the construction of new stimuli-responsive nanodevices,^[19-21, 23, 25, 26] the investigation on how the selective surface functionalization of mesoporous nanomaterials would impact the macroscopic behavior of these organic-inorganic hybrid particles in different environments has just begun. It is foreseeable that the different surface properties, such as the zeta potential and hydrophobicity

would affect the partition, circulation, and agglomeration of these materials in different solutions.^[29] For example, recent reports by Lopez and Zhu^[19, 30, 31] on poly(*N*-isopropylacrylamide)-functionalized mesoporous silica materials have shown an interesting temperature-dependent controlled release property. However, to precisely control the aforementioned surface properties, it is important to develop synthetic methods that would allow controllable and selective surface functionalization of MSN. Herein, we report on the synthesis of a series of poly(*N*-isopropylacrylamide)-coated mesoporous silica nanoparticle material (PNiPAm-MSN) via a surface-initiated controlled/living radical polymerization with a reversible addition-fragmentation chain transfer (RAFT) reaction. We demonstrated that the degree of polymerization on the exterior surface of mesoporous silica nanospheres could be controlled and fine-tuned. Nitrogen sorption analysis, ²⁹Si and ¹³C solid-state NMR spectroscopy, transmission electron microscopy (TEM), and power X-ray diffraction (XRD) were used to characterize the structure and the degree of polymerization of the PNiPAm-MSN.

It has been demonstrated that the conformation of PNiPAm undergoes a change between a hydrated (coiled and soluble) and a dehydrated (collapsed and insoluble) state in water at ~32 °C.^[32] While the lower critical solution temperature (LCST) of PNiPAm itself in water is well-studied, to the best of our knowledge, there is no prior investigation on whether or not the solubility and partitioning behavior of PNiPAm-coated nanoparticles would display any temperature-dependency. To realize our goal of using surface-anchored organic functional groups to manipulate the solubility, circulation, and partition behavior of MSN materials, the temperature dependent aqueous solubility of these core-shell PNiPAm-MSN

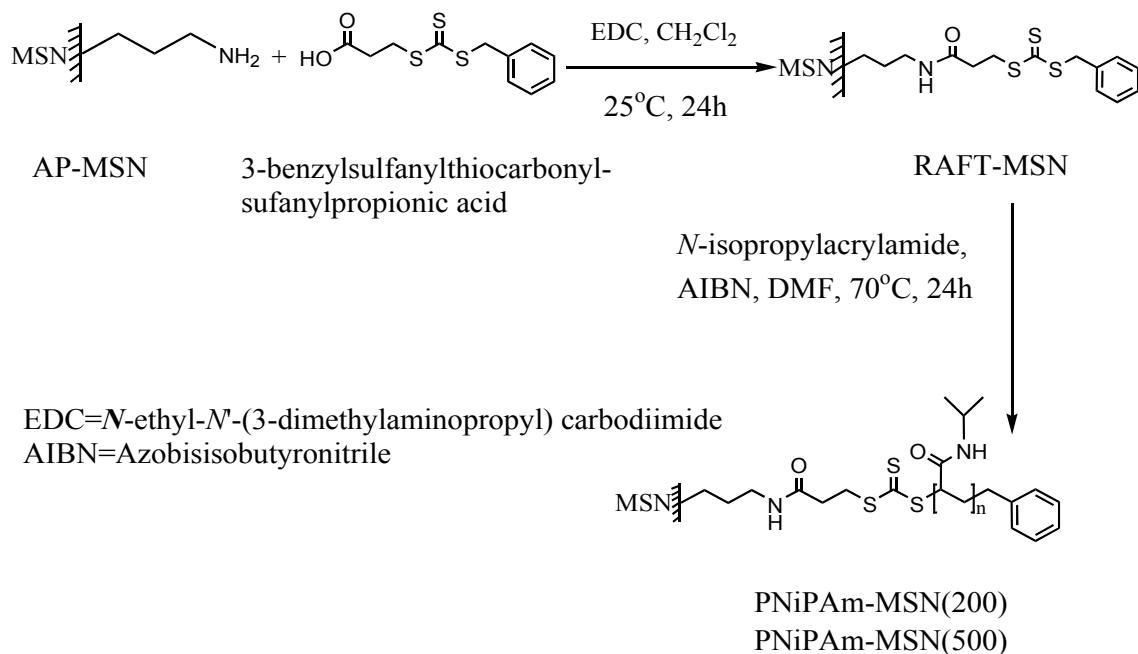
nanoparticles and their partitioning behaviors in a biphasic solution consisting of water and toluene were investigated.

2. Results and discussion

2.1. Synthesis of PNiPAm-MSN

To control the degree of polymerization of the thermal responsive PNiPAm polymer on the exterior surface of MSN, we first synthesized a cetyltrimethylammonium bromide (CTAB) containing mesoporous silica nanoparticle (MSN) material grafted with a 3-aminopropyl group on the exterior particle surface via a procedure outlined in the experimental section.^[27] The CTAB surfactant molecules were removed from this organically functionalized MSN to yield an AP-MSN material by a previously reported method.^[27, 33] As depicted in **Scheme 1**, the aminopropyl group of the AP-MSN material was reacted with 3-benzylsulfanylthiocarbonylsufanylpropionic acid^[34] to give rise to a RAFT-MSN material. The thiocarbonate functional group served as a chain transfer agent (CTA) for the RAFT living radical polymerization of PNiPAm on the MSN surface, which was accomplished in the presence of radical initiator, azobisisobutyronitrile (AIBN) and *N*-isopropylacrylamide. The resulting PNiPAm-MSN material was isolated and purified via the procedure described in the experimental section. To demonstrate that the degree of polymerization could indeed be regulated by using different concentrations of the *N*-isopropylacrylamide monomer, we synthesized two PNiPAm-MSN materials (PNiPAm-MSN (200) and PNiPAm-MSN (500)) with the molar ratio of 200 and 500 between *N*-isopropylacrylamide monomer and the thiocarbonate RAFT agent, respectively.

Scheme 1.



2.2. Solid-state NMR study of PNiPAm-MSNs

To determine the structures and concentrations of organic functional groups, the surface-derivatized MSNs were analyzed by solid-state NMR spectroscopy at various stages of the synthetic process. The main goal of these studies was to find out whether the degree of polymerization could be regulated by establishing favorable conditions for the RAFT polymerization involving NiPAm. To this end, we examined the following samples, AP-MSN, RAFT-MSN, PNiPAm-MSN (200), and PNiPAm-MSN (500).

The ^{13}C and ^{29}Si NMR spectra of samples 1-4 are shown in Figures 1 and 2. Tables 1 and 2 summarize the assignments of the observed ^{13}C resonance lines and the relative concentrations of silicon functionalities, respectively. The ^1H - ^{13}C cross-polarization magic angle spinning (CPMAS) spectrum of sample 1 (Figure 1a) exhibits three dominant resonances, which can be readily assigned to carbons C1, C2 and C3 in the aminopropyl

group (AP). By measuring the carbon intensities as a function of t_{CP} , we found that the cross polarization time constant τ_{CP} was of the order of 50 μ s for all three carbons, which implies that the AP groups are bound rigidly on the MSN surface. Based on the ^{29}Si NMR spectra of the same sample (see Figure 2a), we estimated that the degree of functionalization was substantial (11 ± 2 %). Since the AP groups in sample 1 were grafted on the silica surface while the mesopores were still filled with the CTAB surfactant, such high accumulation of T sites can be only explained by multilayer condensation of grafted species on outer surfaces of the MSN's. This kind of multilayer condensation of 3-aminopropylmethoxysilane on silica

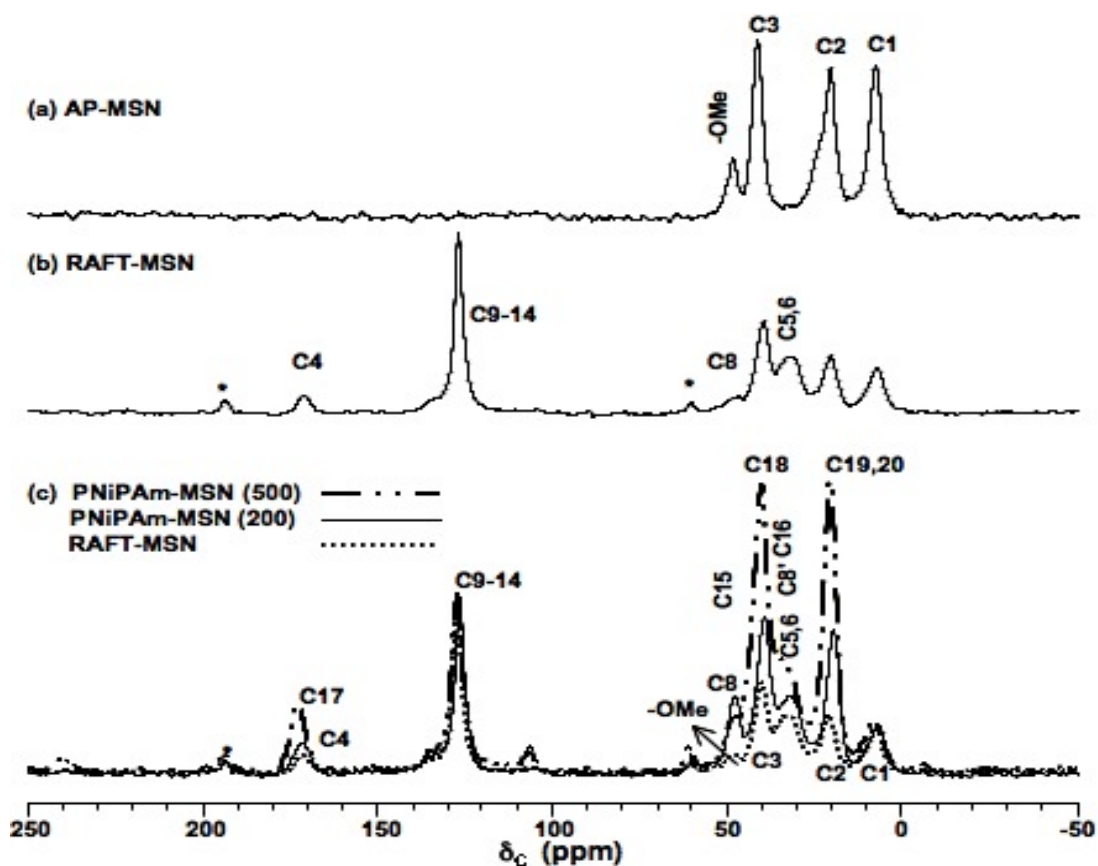
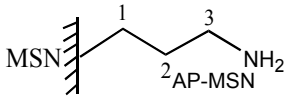
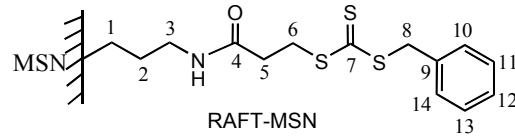
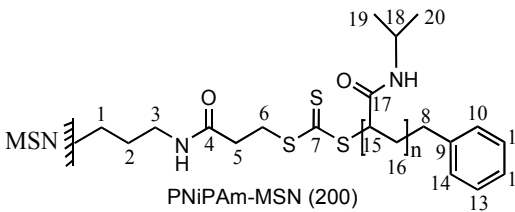


Figure 1. $^1\text{H} \rightarrow ^{13}\text{C}$ CPMAS spectra of (a) AP-MSN, (b) RAFT-MSN and (c) PNiPAm-MSN (500) (top spectrum), PNiPAm-MSN (200) (middle spectrum) and RAFT-MSN (bottom spectrum). Asterisks denote the spinning sidebands.

surface by the grafting method has been well documented in literature.^[35] Also present in ¹³C spectrum is a peak at around 50 ppm, representing the methoxy groups associated with T2 silicon sites.^[36]

Table 1. Summary of ¹³C CPMAS spectral assignments and the molecular structures identified in MSN materials.

sample	spectral assignments ^a (δ_c in ppm)
 AP-MSN	C1: 8; C2: 21; C3: 42
 RAFT-MSN	C1: 9; C2: 22; C3: 42; C4: 173; C5,6: 33,36; C8: 49; C9-14: 128
 PNiPAm-MSN (200) PNiPAm-MSN (500)	C1: 9; C2: 21; C3: 42; C4: 173; C5,6: 33,36; C8: 37; C9-14: 128; C15: 48; C16: 36; C17: 174; C18: 41; C19,20: 21

[a] As explained in the text, the observed species also included the methoxy groups (~ 50 ppm)

benzylsulfanylthiocarbonylsufanylpropionic acid. By comparing the intensities associated with carbons C1 and C2 in AP with those of the carbonyl groups C4 (at 173 ppm) and carbons in the phenyl rings C9-C14 (at 128 ppm), we estimated that 20 ± 4 % of AP linkers reacted with the 3-benzylsulfanylthiocarbonylsufanylpropionic acid molecules. This estimate took into account the substantial differences in CP dynamics between carbons C1 and C2 ($\tau_{CP} \approx 50 \mu s$), C4 ($\tau_{CP} \approx 1.25$ ms) and C10-C14 ($\tau_{CP} \approx 140 \mu s$). As expected, the ²⁹Si CPMAS and DPMAS spectra of the RAFT-MSN (Figure 2b) remained essentially the same as those

The ¹³C CPMAS spectrum of RAFT-MSN (Figure 1b) features several additional resonances, which were assigned to carbons C4-C14 in the trithiocarbonate CTA functionality (Table 1), based on the spectrum of a neat compound of 3-

of AP-MSN. Similar measurements, performed with a sample exposed to 3-benzylsulfanylthiocarbonylsufanylpropionic acid without earlier functionalization with AP,

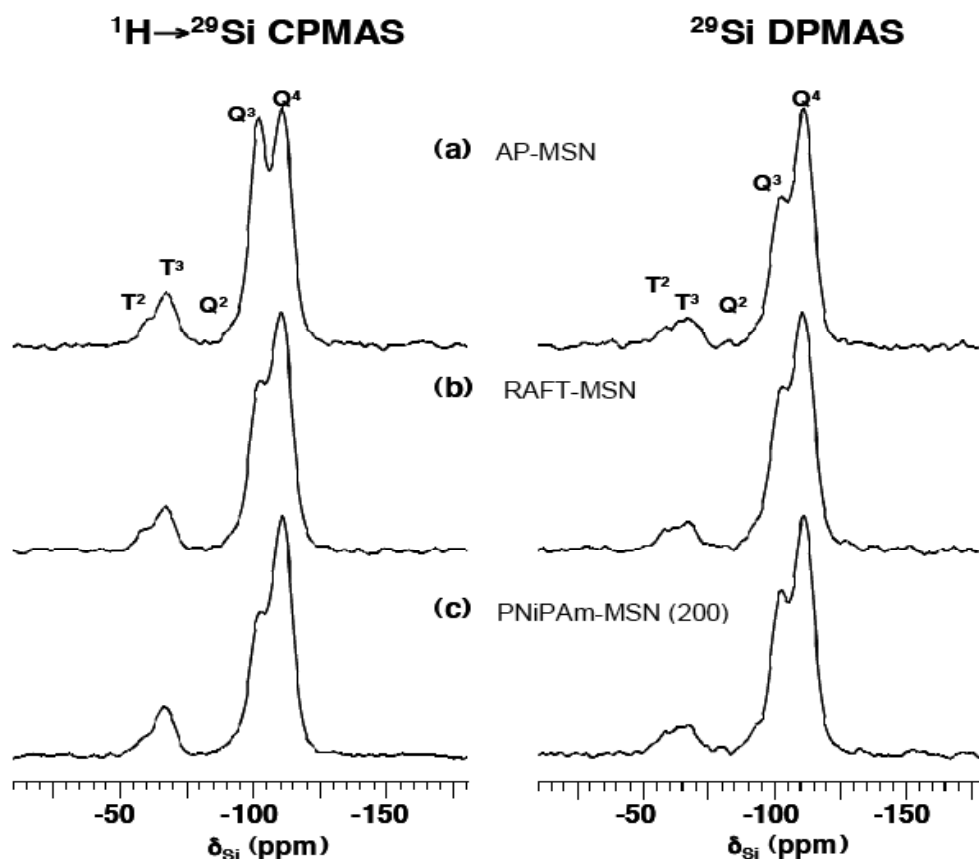


Figure 2. $^1\text{H} \rightarrow ^{29}\text{Si}$ CPMAS and ^{29}Si DPMAS spectra of (a) AP-MSN; (b) RAFT-MSN and (c) PNiPAm-MSN (200).

showed no evidence of reactivity between the CTA molecules and the silica surface.

In Figure 1c, the ^{13}C CPMAS spectrum of RAFT-MSN is compared with the spectra of samples coated with the PNiPAm polymer (PNiPAm-MSN (200) and PNiPAm-MSN (500)). The spectra provide evidence that the polymerization reaction indeed took place. Again, the concentration of T sites remained unaltered by this reaction (see Figure 2c and Table 1). During polymerization the fragmentation path is determined by relative stability of the carbon centered radicals generated by trithiocarbonate dissociation.^[37, 38] In the present

study, the benzyl radicals, which are more stable than the primary alkyl radicals, directed the fragmentation toward the benzyl group. When the first NiPAm unit was inserted via the RAFT process, carbon C8 (attached to the benzyl radical) was moved away from the CTA center and its resonance position shifted from 48 ppm to around 37 ppm (it is denoted as C8' in Figure 1c). This site was replaced by carbons C15 and C16 of the polymer backbone, resonating at 48 and 36 ppm, respectively. Addition of the second unit created a new site in the polymer backbone (C21), whose resonance (at 36 ppm, not marked) overlaps with carbons C5, C6, C8' and C16. The peak at around 174 ppm, which in sample 2 was solely due to carbon C4 in CTA, has intensified due to the contributions from carbonyl carbons C17 in each of the NiPAM monomer units. The resonance signals attributed to carbon C18 contributed to the increased intensity at 41 ppm, whereas carbons C19 and C20 amplified the peak at 21 ppm, which previously represented only carbon C2. As the RAFT polymerization reaction progressed, by increasing the NiPAm concentration, the intensities attributed to carbons C16-C21 increased as well, as Figure 1c demonstrates.

Table 2. Quantification of silicon group from ^{29}Si DPMAS NMR data

Sample	Relative concentration of silicon groups [%]				Relative Conc. mmol/g
	T ⁿ	Q ²	Q ³	Q ⁴	
AP-MSN	11	3	28	61	1.55
RAFT-MSN	10	5	27	58	1.06
PNiPAm-MSN (200)	11	6	27	57	0.99

The relative intensities of selected ^{13}C resonances were used to estimate the average number n_{av} of NiPAm units per CTA initiator. The spectra in Figure 1c

were plotted such that the peak representing the phenyl carbons C9-C14 was normalized to the same height. The concentration of these groups on the surface should remain fixed, thus the absolute contribution of carbon C4 to the resonance centered at 174 ppm should remain constant, as well. Since the carbonyl carbons in the CTA and in the polymer were polarized with similar efficiency, n_{av} could be estimated from the relative contributions of carbons C4 and C17 to this resonance. In the case of PNiPAm-MSN (500), we obtained $n_{av} = 4.0$.

The NMR measurements can be summarized as follows: 1) approximately 10% of silicon sites in the samples are of type T, 2) one out of five of these sites reacted with RAFT molecules to form the CTA, and 3) the average polymer length corresponded to $n_{av} \cdot 1/44.0$. Based on this information we established the overall organic content in PNiPAm-MSN(500) to be approximately 35 (± 3) wt%, and the polymer content in the same sample to be equal to 10 (± 2) wt%. These results agree very well with the TGA analysis data shown in Section 2.7. They must also be reconciled with the TEM micrograph image of the spherical PNiPAm-MSN(500) particle, which shows a 19 nm thick rim as a result of the PNiPAm coating of its outer surface (Fig. 5c and 5d). This thickness corresponds to relatively long polymer chains composed of a large number (of the order of 50) of NiPAm units. Since solid-state NMR yielded an n_{av} value of 4.0, we must assume that only a small fraction ($\sim 10\%$) of RAFT centers present on the outer surface of the MSNs participated in the addition-fragmentation polymerization reaction. Presumably, the isopropylamidyl side chains that formed initially during polymerization rendered most of the neighboring sites inaccessible, which favored the formation of longer chains. This type of limited chemical accessibility during surface reactions has been observed in many surface reactions of self-assembled monolayer systems.^[39]

2.3. Powder X-ray diffraction patterns of PNiPAm-MSN

Figure 3 shows the powder X-ray diffraction patterns of RAFT-MSN, PNiPAm-MSN (200), and PNiPAm-MSN (500). These XRD spectra feature an intense (100) reflection peak corresponding to lattice spacings in the range of 38.5 to 42.0 Å. The well-resolved diffraction patterns characteristic of hexagonal MCM-41 type of mesoporous silicas,

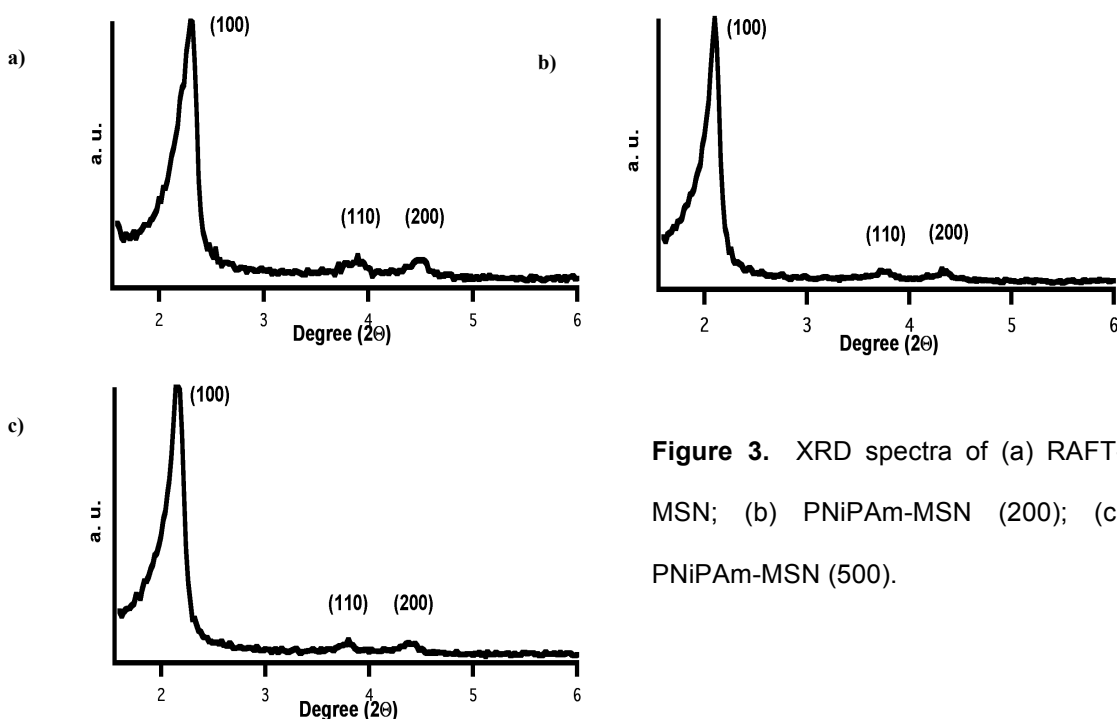


Figure 3. XRD spectra of (a) RAFT-MSN; (b) PNiPAm-MSN (200); (c) PNiPAm-MSN (500).

including (100), (110), and (200) peaks, were clearly observed. The results indicated that the parallel cylindrical channel-like mesoporous structure of the MSN material was unaltered by the different degree of RAFT polymerization of NiPAm on the silica surface.^[40-44]

Here one particular part of the hypothesis that is currently being explained is examined and particular elements of that part are given careful scrutiny.

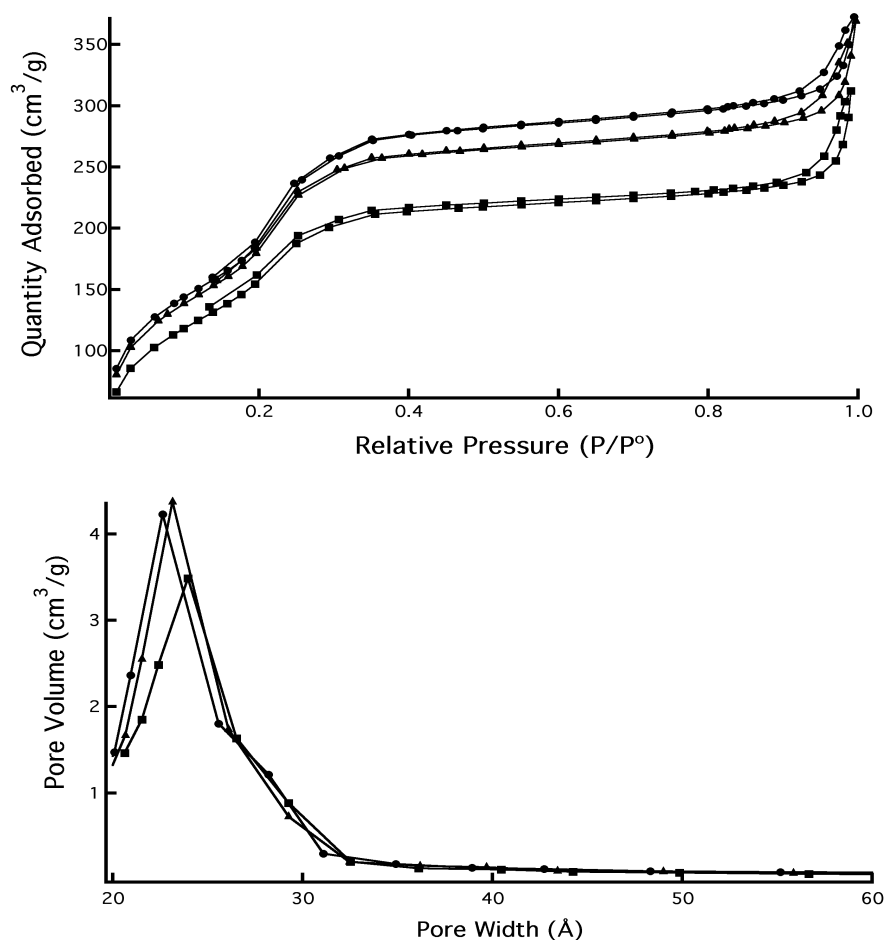
2.4. Nitrogen sorption properties of PNiPAm-MSNs

To confirm that the polymerization took place exclusively on the exterior surface of the MSN, we analyzed the N₂ sorption properties of RAFT-MSN as well as the polymer-coated PNiPAm-MSN(200) and PNiPAm-MSN(500). As summarized in Table 3, the total surface areas and the average pore diameters of RAFT-MSN, PNiPAm-MSN(200) and PNiPAm-MSN(500) were determined by the BET and BJH methods, respectively. The BET isotherms of these three materials exhibited the characteristic Type IV adsorption/desorption patterns, which indicated the presence of cylindrical channel-like porous structure (Figure 4a). Also, only small decreases ($< 100 \text{ m}^2/\text{g}$) in the total surface area were observed after the NiPAm polymerization. These results indicated that the NiPAm polymer did not fill up the mesopores. The BJH analysis (Figure 4b) of all three materials showed narrow pore size distributions confirming that the mesopores remain accessible by nitrogen gas even after the polymerization. Again, these data strongly suggest that the PNiPAm is present predominantly on the exterior surface of the MSN particles after the polymerization.

Table 3. Structural properties of surface-functionalized MSNs

Sample	$S_{\text{BET}}^{[a]}$ [m ² g ⁻¹]	$W_{\text{BJH}}^{[a]}$ [Å]	$V_p^{[a]}$ [cm ³ g ⁻¹]	V_p (at P/P ₀ =0.25) [cm ³ g ⁻¹]
Raft-MSN	696.7	22.6	0.50	0.37
PNiPAm-MSN (200)	683.3	23.1	0.48	0.35
PNiPAm-MSN (500)	597.7	24.0	0.40	0.28

^[a] S_{BET} represents the surface area; W_{BJH} represents the pore diameter; V_p represents the pore volume.

**Figure 4.** (a) BET isotherm (left) and (b) BJH pore size distribution(right).

(-●-) indicates RAFT-MSN; (-▲-) indicates PNiPAm-MSN (200); (-■-) indicates PNiPAm (500))

2.5. Transmission electron microscopy study of PNiPAm-MSNs

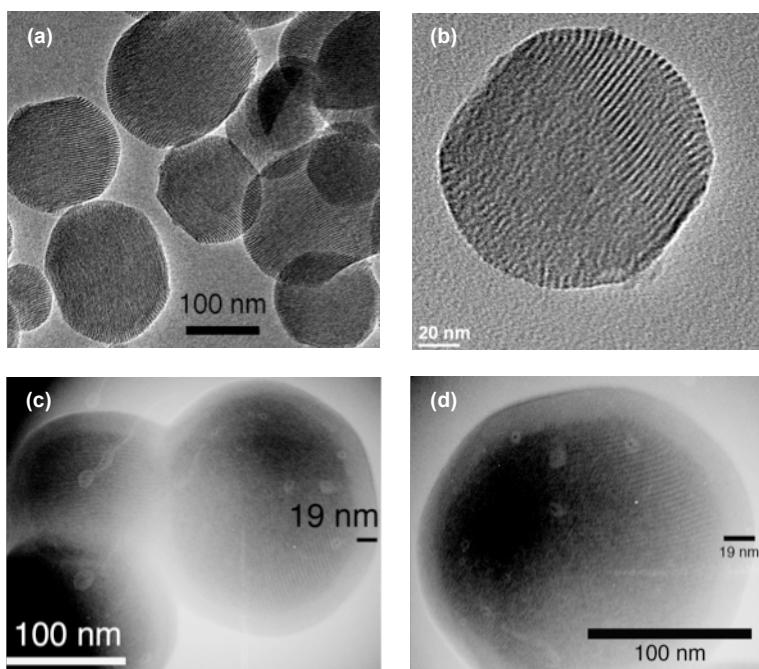


Figure 5. TEM micrographs of AP-MSN (a) and (b); PNiPAm-MSN (500) (c) and (d).

mesoporous structure of AP-MSN (Figure 5b) was not destroyed by the NiPAm polymerization. This result is consistent with those of N_2 sorption studies (*vide supra*). An amorphous rim-like coating was also observed in Figure 5d. Many literature reports^[27, 28, 45] have attributed this type of structures to the presence of polymers on the exterior MSN surface. The thickness of NiPAm polymer coating of PNiPAm-MSN (500) was determined to be 19 nm by measuring the width of the amorphous rim around the spherical MSN particle.

TEM was employed for direct visualization of the pore geometry of the PNiPAm-MSN materials. As shown in Figure 5a, the PNiPAm-MSN (500) material exhibited an interesting core-shell type of structure. The observed parallel stripes in the core area clearly indicated the MCM-41 type of cylindrical channel-like

2.6. Temperature-responsive partition study of PNiPAm-MSNs

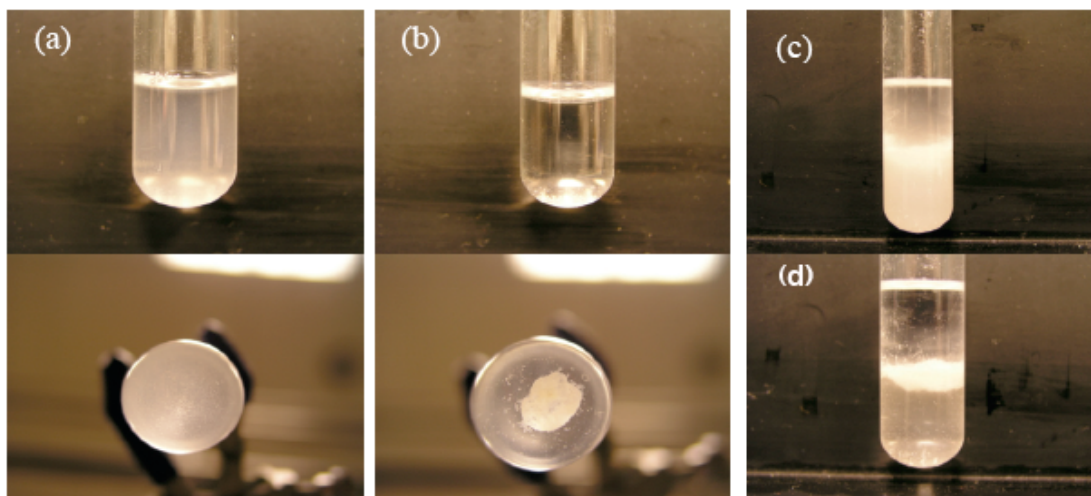


Figure 6. (a) Side and bottom views of the dispersion of PNiPAm-MSN (500) in water at room temperature, (b) the precipitate of PNiPAm-MSN (500) in water after elevating temperature to 40 °C, (c) side view of the dispersion of PNiPAm-MSN (500) in toluene/water at room temperature and (d) the movement of PNiPAm-MSN (500) in toluene/water after elevating temperature to 40 °C.

While PNiPAm is a well-studied thermal responsive polymer,^[32] it is unclear whether by coating of this polymer on the outside of MSNs, any temperature dependency could be introduced for the manipulation of the water solubility and the solution partition behavior of these core-shell nanoparticles. To answer this question, we examined the water solubility of PNiPAm-MSNs and their partition behaviors in a biphasic water/toluene solution at various temperatures. First, the polymer-coated MSNs were introduced to water. In contrast to the pure inorganic, non-functionalized MSN material, where these nanoparticles would precipitate after a period of time (~10 minutes) in water, the PNiPAm-coated MSNs were dispersed completely and formed a homogeneous suspension in water at room temperature as shown in Figure 6a. No precipitate could be observed even after 24 hours suspending in

water. When the temperature of water was elevated to 40 °C, it is interesting to note that the PNiPAm-MSN (500) underwent complete dehydration and became hydrophobic as indicated by the precipitates formed at the bottom of test tube shown in Figure 6b. These results strongly suggested that the thermal responsive NiPAm polymer coating could indeed dictate the water solubility of these MSN nanoparticles.

To further understand how the temperature dependent conformational changes of NiPAm polymers would influence the partition properties of these core-shell nanoparticles, PNiPAm-MSNs were introduced to a toluene/water biphasic solution. We found that these PNiPAm-MSNs exhibited an interesting temperature-dependent partition behavior. For example, at room temperature, PNiPAm-MSN (500) was dispersed evenly in the water layer as shown in figure 6c. However, these nanoparticles were able to move upward into the hydrophobic toluene layer when the temperature of the biphasic solution reached above 40 °C as depicted by the cloudy layer formed in the toluene layer (Figure 6d). In contrast, the non-functionalized MSN particles remained as precipitates at the bottom of the water layer even when the temperature was elevated from 25 to 60 °C. These results clearly indicated that the conformational changes of the NiPAm polymer layer on the exterior surface of MSN has a major impact on altering the hydrophobicity of the whole organic-inorganic hybrid PNiPAm-MSN material.

2.7. Thermogravimetric analysis study of PNiPAm-MSNs

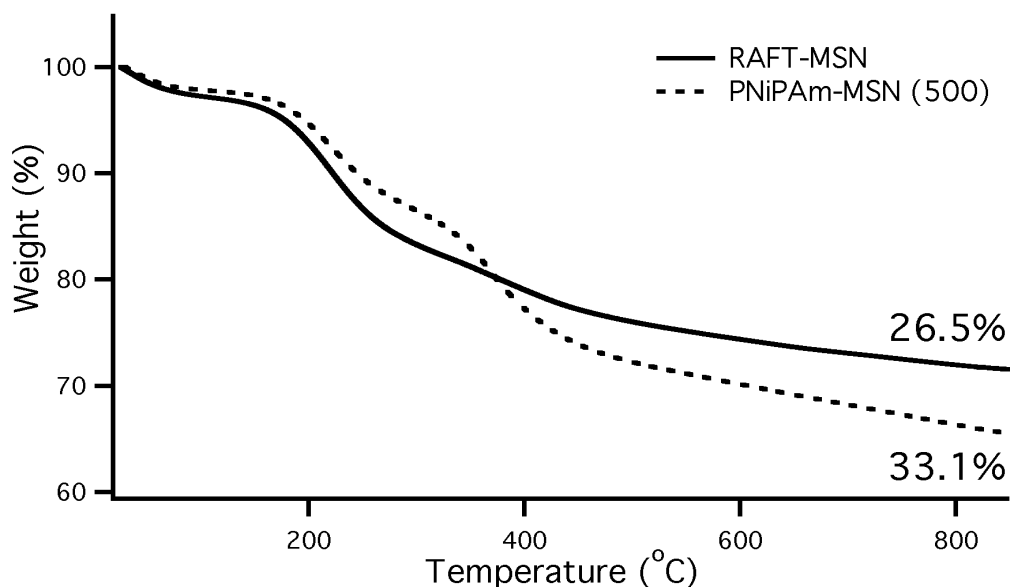


Figure 7. Thermogravimetric Analyses of RAFT-MSN (solid line) and PNiPAm-MSN (500) (dashed line).

Thermogravimetric (TGA) analyses of PNiPAm-MSN(500) and RAFT-MSN showed weight losses of 33.1% and 26.5%, respectively, when the materials were heated up to 850 °C.(Figure 7) The difference in weight loss between these two materials was only about 7%. The weight ratio of PNiPAm/silica is determined to be 0.1, which is consistent with the aforementioned solid NMR data. Furthermore, the pore volumes of the PNiPAm-MSN(500) and RAFT-MSN at a low relative pressure ($P/P_0=0.25$) were found to be 0.28 cm^3/g and 0.37 cm^3/g , respectively, as determined by the N_2 porosimetry. Given that the pore volumes measured at this low are based on the amounts of N_2 adsorbed inside the mesopores and not between the particles, the observed small difference in pore volumes before and after the polymerization suggest that PNiPAm polymers do not fill up the mesopores, which is consistent with the aforementioned NMR results.

2.8. Dynamic light scattering study of PNIPAm-MSNs

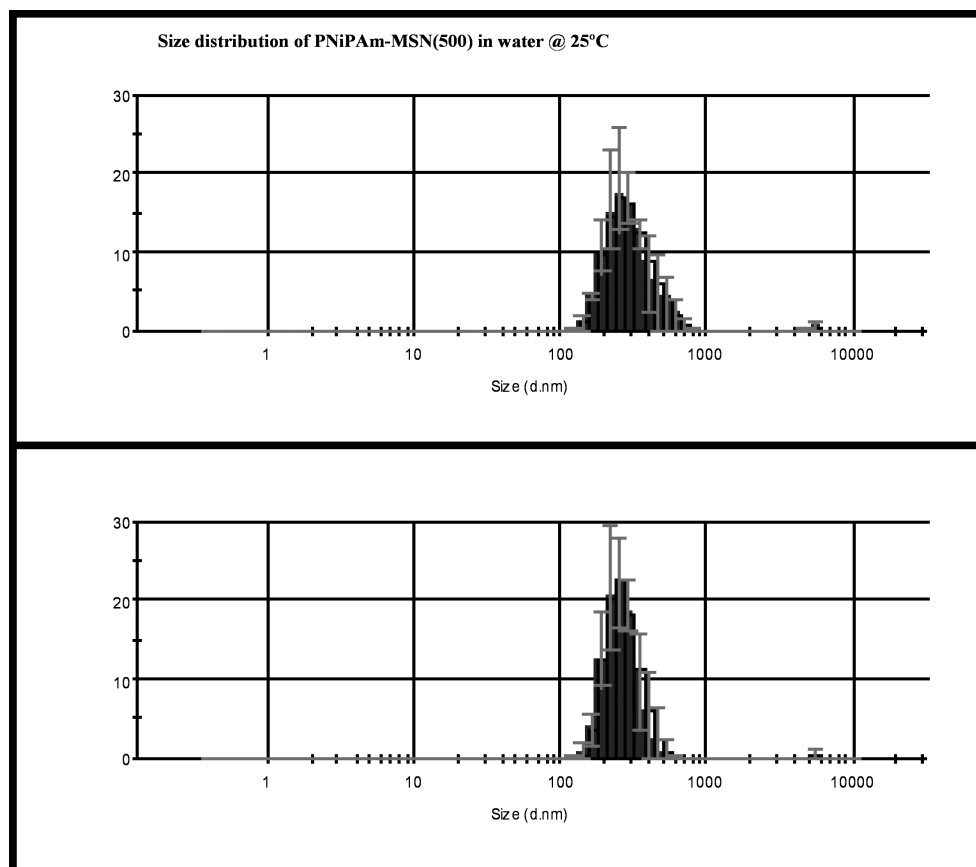


Figure 8. The size distribution of PNIPAm-MSN(500) in water at 25°C (top); the size distribution of PNIPAm-MSN(500) in water at 25°C after one heating cycle (bottom)

In order to investigate the redispersability of PNIPAm-MSN material, we used the DLS to measure the size distribution of PNIPAM-MSN in water solution. As shown below in figure 8, the PNIPAM-MSN(500) exhibited narrow size distribution with average particle size about 314 nm at 25 °C. After elevating the temperature above 40 °C and cooling down to 25 °C, the PNIPAm-MSN(500) particles still were well dispersed with average particle size about 340 nm in water after sonication. Therefore, the PNIPAM-MSN particles can be well

dispersed in water with the assistance of PNiPAm at room temperature and be redispersed again after the thermal response with the increase of temperature.

3. Conclusions

In summary, we have demonstrated the successful synthesis and characterization of a series of poly(*N*-isopropylacrylamide)-coated mesoporous silica nanoparticle materials. We discovered that the surface-initiated RAFT polymerization of NiPAm on the MSN surface could be controlled and the degree of polymerization could also be tuned. The chemical structure and surface densities of the NiPAm polymers on the MSN surface were measured by ^{29}Si and ^{13}C solid-state NMR spectroscopy. The transmission electron microscopy (TEM) and N_2 sorption studies of these PNiPAm-MSNs showed that the polymers did not fill up the mesopores and the NiPAm, in fact, formed a rim-like coating on the exterior surface of MSN. Also, we found that the thermally induced conformational changes of NiPAm polymer layer indeed altered the surface properties of these organic-inorganic hybrid nanoparticles, as manifested by the temperature dependent solution partition behavior of these core-shell materials in a biphasic toluene/ water solution. These results suggest that the strategy of using an organic polymer coating to manipulate the solution behaviors of the MSN material could lead to new nanodevices for unique thermal sensitive controlled release and circulation properties in different solution environments.

4. Experimental

AP-MSN: 3-Aminopropyltrimethoxysilane (APTMS, 179.3 mg) was added to a toluene suspension (80 mL) of the CTAB surfactant-containing MSN (1.0 g). The mixture was refluxed for 8 h under nitrogen. The resulting material was filtered, washed extensively with toluene, methylene chloride, and methanol. The resulting material was dried under vacuum overnight. To remove the CTAB surfactant, the 3-aminopropyl-grafted MSN (1.0 g) was added to a methanolic solution of 1.0 mL concentrated hydrochloric acid, followed by refluxing at 64.7 °C for 6 h. The surfactant-removed AP-MSN material was washed with water/methanol solution of sodium bicarbonate and pure methanol, then dried under vacuum.

RAFT-MSN: AP-MSN (1.0 g) was reacted with 3-benzylsulfanylthiocarbonylsufanylpropionic acid^[34] (272.4 mg) in the presence of *N*-Ethyl-*N'*-(3-dimethylaminopropyl)carbodiimide (EDC; 300 mg) in 20 mL methylene chloride at room temperature for 24 h. After reaction, the solution was filtered and the particles were washed by copious amount of methylene chloride and methanol to remove the physisorbed RAFT agents. The resulting yellowish material was dried under vacuum overnight.

PNiPAm-MSN(200): RAFT-MSN (200 mg), azobisisobutyronitrile (0.7 mg), *N*-isopropylacrylamide (0.9 g), and DMF (5 mL) were mixed in a Schlenk tube, followed by sonication for 5 min. The tube was subjected to three cycles of freeze-pump-thaw degas process to remove oxygen. The tube was then placed in an oil bath preset at 70 °C for 24 h. The polymerization was terminated by opening the tube to atmosphere and then diluted with methanol. The resulting PNiPAM-MSN was obtained by centrifuging the solution. The

solid product was isolated by filtration and washed with copious amount of methanol to remove any unreacted monomers and physisorbed NiPAm polymer.

PNiPAm-MSN(500): RAFT-MSN (200 mg), azobisisobutyronitrile (0.7 mg), *N*-isopropylacrylamide (2.26 g), and DMF (5 mL) were mixed in a Schlenk tube, followed by sonication for 5 min. The tube was subjected to three cycles of freeze-pump-thaw degas process to remove oxygen. The tube was then placed in an oil bath preset at 70 °C for 24 h. The polymerization was terminated by opening the tube to atmosphere and then diluted with methanol. The resulting PNiPAM-MSN was obtained by centrifuging the solution. The solid product was isolated by filtration and washed with copious amount of methanol to remove any unreacted monomers and physisorbed NiPAm polymer.

Solution Partition Experiment: Particle partition experiments were conducted in water/toluene biphasic system. In a typical experiment, PNiPAm-MSN(500) (5 mg) was suspended in a culture tube with 3 mL nanopure water and the solution was sonicated for 30 min. The solution was added 3 mL toluene on top of the water layer, followed by another 30 min sonication. After that, the tube was put in an oil bath at 40 °C. The physical behaviors of the PNiPAm-MSN particles were recorded by a digital camera.

Solid-state NMR spectroscopy: The experiments were performed on a Varian/Chemagnetics Infinity 400 spectrometer at the frequencies of 79.5, 100.6 and 400.0 MHz for ^{29}Si , ^{13}C and ^1H , respectively. All measurements were carried out using a triple tuned 5-mm magic angle spinning (MAS) T3 probe and tightly capped zirconia rotors. ^{13}C and ^{29}Si nuclei were observed using direct polarization (DP) or by variable amplitude cross polarization (CP)^[46, 47] from the neighboring protons.

During ^1H - ^{13}C CPMAS measurements, the ^1H RF magnetic field $\nu_{\text{RF}}^{\text{H}}$ was ramped between 19 and 30 kHz using 1 kHz increments, whereas $\nu_{\text{RF}}^{\text{C}}$ was set at a constant level of 36 kHz. The $\nu_{\text{RF}}^{\text{H}}$ value of 55 kHz was used for initial excitation and TPPM decoupling.^[48] The samples were spun at a rate $\nu_{\text{R}} = 6.7$ kHz to minimize overlap between the centerband resonance signals and the spinning sidebands. The ^1H longitudinal relaxation time T_1 in the studied samples did not exceed 1.2 s. Typically 12,000 scans were collected using a pulse delay of 1.5 s and a contact time τ_{CP} between 0.1 and 1.0 ms. In the case of CPMAS, the intensity observed for each carbon species is influenced by the spin-lattice relaxation processes in the rotating frame and the CP kinetics, which, in turn, depends on sample spinning, molecular motions and site-dependent ^1H - ^{13}C distances.^[49] However, the relative change in concentrations of different functional groups could be determined with good accuracy by acquiring the ^{13}C CPMAS spectra under identical conditions. To ensure that, the magnitudes of the applied RF fields were verified between the measurements using a reference sample of hexamethylbenzene. The DPMAS measurements, which are preferred for quantitative analysis, could not be carried out because the T_1 values for ^{13}C nuclei were of the order of several minutes. The assignments of ^{13}C resonances observed in functionalized samples were based on the spectra of neat compounds and on the results reported earlier in the literature.

The ^{29}Si DPMAS experiments were performed in order to quantify various silicon groups. The ^{29}Si longitudinal relaxation times T_1 were between 30 s and 60 s, therefore a pulse delay of 300 s was used in these measurements. A total of 304 scans were accumulated for each spectrum, using $\nu_{\text{R}} = 8$ kHz and $\nu_{\text{RF}}^{\text{Si}} = 50$ kHz. The Carr-Purcell-Meiboom-Gill (CPMG) train of π pulses was implemented during the acquisition period to enhance the

intensity of ^{29}Si resonance. By acquiring 25 CPMG echoes with 8 ms intervals, a five-fold increase in sensitivity without quantitative distortions was obtained.^[49] The ^{29}Si spectra consisted of several resonances representing $(\equiv\text{SiO})_n\text{Si}(\text{OH})_{4-n-m}\text{R}_m$ sites with $m = 0$ and $m = 1$, denoted as Q^n and T^n . The signals at around -93, -101 and -111 ppm are known to represent silicon sites Q^2 (geminal silanol), Q^3 (single silanol) and Q^4 (siloxane), whereas the T^2 and T^3 functionalities typically resonate around -59 and -68 ppm, respectively.^[50-53] The degree of functionalization $T/Q = [(T^2+T^3)/(T^2+T^3+Q^2+Q^3+Q^4)]$ was evaluated based on the deconvolution of ^{29}Si DPMAS NMR spectra. The $^1\text{H} \rightarrow ^{29}\text{Si}$ CPMAS experiments were also carried out, using the following experimental conditions: $\nu_{\text{RF}}^{\text{H}} = 52$ to 60 kHz (ramped in 1 kHz increments), $\nu_{\text{RF}}^{\text{Si}} = 56$ kHz (during CP), $\nu_{\text{RF}}^{\text{H}} = 71$ kHz (during initial excitation), $\nu_{\text{RF}}^{\text{H}} = 36$ kHz (during TPPM decoupling) and $\tau_{\text{CP}} = 8$ ms. Each ^{29}Si CPMAS spectrum consisted of 640 scans, acquired with a pulse delay of 2 s and the CPMG detection scheme as described above in the case of DPMAS. The non-quantitative, albeit more intense, $^1\text{H} \rightarrow ^{29}\text{Si}$ CPMAS spectra were merely used to more accurately determine the positions and line shapes associated with the T^n sites. The ^{13}C and ^{29}Si chemical shifts were referenced to HMB and SiMe_4 , respectively.

Other characterization methods: For transmission electron microscopy (TEM) studies, a small aliquot was taken from a suspension of water and placed in a lacey carbon film coated 400 mesh copper grid, which was allowed to dry in air. The TEM image was examined using a Philips model CM-30 TEM operated at 300 kV. The specimen was given no further treatment, as it appeared stable under beam bombardment. Powder XRD experiments were performed on a Scintag XDS 2000 diffractometer using a $\text{Cu K}\alpha$ radiation source. Low angle diffraction with 2θ range of 1 to 10° was used to investigate the long-

range order of the materials. The surface area and median pore diameter were measured using N₂ adsorption/desorption measurements in a Micromeritics ASAP 2000 BET surface analyzer system. The data were evaluated using the Brunauer-Emmett-Teller (BET) and Barrett-Joyner-Halenda (BJH) methods to calculate the surface area and pore volumes/pore size distributions, respectively. Samples were prepared by degassing at 90°C for overnight before analysis. For thermogravimetric analysis, samples were tested with TA Instruments, Model 2950 Thermogravimetric Analyzer. The tests were normally performed in an air atmosphere and the heating rate was 2 °C/min, from ambient to 850 °C. The data was analyzed by Universal Analysis 2000 software. For dynamic light scattering study, sample was prepared in concentration 0.1 mg/mL and measured by the DLS of Malvern Nano HT Zetasizer. Each task was tested in triplicate.

Reference

- [1] T. Yanagisawa, T. Shimizu, K. Kuroda, C. Kato, *Bull. Chem. Soc. Jpn.* **1990**, *63*, 988.
- [2] S. Inagaki, Y. Fukushima, K. Kuroda, *J. Chem. Soc., Chem. Commun.* **1993**, 680.
- [3] J. S. Beck, J. C. Vartuli, W. J. Roth, M. E. Leonowicz, C. T. Kresge, K. D. Schmitt, C. T. W. Chu, D. H. Olson, E. W. Sheppard, *J. Am. Chem. Soc.* **1992**, *114*, 10834.
- [4] C. T. Kresge, M. E. Leonowicz, W. J. Roth, J. C. Vartuli, J. S. Beck, *Nature* **1992**, *359*, 710.
- [5] D. Y. Zhao, J. L. Feng, Q. S. Huo, N. Melosh, G. H. Fredrickson, B. F. Chmelka, G. D. Stucky, *Science* **1998**, *279*, 548.
- [6] D. Y. Zhao, Q. S. Huo, J. L. Feng, B. F. Chmelka, G. D. Stucky, *J. Am. Chem. Soc.* **1998**, *120*, 6024.
- [7] V. S. Y. Lin, C.-Y. Lai, J. Huang, S.-A. Song, S. Xu, *J. Am. Chem. Soc.* **2001**, *123*, 11510.
- [8] C.-Y. Lai, B. G. Trewyn, D. M. Jeftinija, K. Jeftinija, S. Xu, S. Jeftinija, V. S. Y. Lin, *J. Am. Chem. Soc.* **2003**, *125*, 4451.
- [9] D. R. Radu, C.-Y. Lai, K. Jeftinija, E. W. Rowe, S. Jeftinija, V. S. Y. Lin, *J. Am. Chem. Soc.* **2004**, *126*, 13216.
- [10] U. Ciesla, F. Schüth, *Micropor. Mesopor. Mater.* **1999**, *27*, 131.
- [11] J. Y. Ying, C. P. Mehnert, M. S. Wong, *Angew. Chem. Int. Ed.* **1999**, *38*, 56.
- [12] F. Schüth, *Chem. Mater.* **2001**, *13*, 3184.
- [13] B. J. Scott, G. Wirnsberger, G. D. Stucky, *Chem. Mater.* **2001**, *13*, 3140.
- [14] W. Schmidt, F. Schüth, *Adv. Mater.* **2002**, *14*, 629.
- [15] G. J. A. A. Soler-Illia, J. Patarin, B. Lebeau, C. Sanchez, *Chem. Rev.* **2002**, *102*, 4093.
- [16] A. Stein, *Adv. Mater.* **2003**, *15*, 763.
- [17] C. Sanchez, G. J. A. A. Soler-Illia, F. Ribot, D. S. Grosso, *C. R. Chim* **2003**, *6*, 1131.
- [18] A. Taguchi, F. Schüth, *Micropor. Mesopor. Mater.* **2005**, *77*, 1.
- [19] Q. Fu, G. V. R. Rao, L. K. Ista, Y. Wu, B. P. Andrzejewski, L. A. Sklar, T. L. Ward, G. P. Lopez, *Adv. Mater.* **2003**, *15*, 1262.
- [20] N. K. Mal, M. Fujiwara, Y. Tanaka, *Nature* **2003**, *421*, 350.
- [21] N. K. Mal, M. Fujiwara, Y. Tanaka, T. Taguchi, M. Matsukata, *Chem. Mater.* **2003**, *15*, 3385.
- [22] R. Hernandez, H.-R. Tseng, J. W. Wong, J. F. Stoddart, J. I. Zink, *J. Am. Chem. Soc.* **2004**, *126*, 3370.

- [23] T. D. Nguyen, H.-R. Tseng, P. C. Celestre, A. H. Flood, Y. Liu, J. F. Stoddart, J. I. Zink, *Proc. Natl. Acad. Sci. U.S.A.* **2005**, *102*, 10029.
- [24] K. C. F. Leung, T. D. Nguyen, J. F. Stoddart, J. I. Zink, *Chem. Mater.* **2006**, *18*, 5919.
- [25] T. D. Nguyen, K. C. F. Leung, M. Liong, C. D. Pentecost, J. F. Stoddart, J. I. Zink, *Org. Lett.* **2006**, *8*, 3363.
- [26] S. Giri, B. G. Trewyn, M. P. Stellmaker, V. S. Y. Lin, *Angew. Chem. Int. Ed.* **2005**, *44*, 5038.
- [27] D. R. Radu, C.-Y. Lai, J. W. Wiench, M. Pruski, V. S. Y. Lin, *J. Am. Chem. Soc.* **2004**, *126*, 1640.
- [28] Y. Zhu, J. Shi, *Micropor. Mesopor. Mater.* **2007**, *103*, 243.
- [29] I. Slowing, B. G. Trewyn, V. S. Y. Lin, *J. Am. Chem. Soc.* **2006**, *128*, 14792.
- [30] Q. Fu, G. V. RamaRao, T. L. Ward, Y. Lu, G. P. Lopez, *Langmuir* **2007**, *23*, 170.
- [31] Z. Zhou, S. Zhu, D. Zhang, *J. Mater. Chem.* **2007**, *17*, 2428.
- [32] Y. Ono, T. Shikata, *J. Am. Chem. Soc.* **2006**, *128*, 10030.
- [33] S. Huh, J. W. Wiench, J.-C. Yoo, M. Pruski, V. S. Y. Lin, *Chem. Mater.* **2003**, *15*, 4247.
- [34] M. H. Stenzel, T. P. Davis, A. G. Fane, *J. Mater. Chem.* **2003**, *13*, 2090.
- [35] J. Trebosc, J. W. Wiench, S. Huh, V. S. Y. Lin, M. Pruski, *J. Am. Chem. Soc.* **2005**, *127*, 7587.
- [36] J. C. Hicks, R. Dabestani, A. C. Buchanan, C. W. Jones, *Chem. Mater.* **2006**, *18*, 5022.
- [37] R. T. A. Mayadunne, J. Jeffery, G. Moad, E. Rizzardo, *Macromolecules* **2003**, *36*, 1505.
- [38] R. H. Lambeth, S. Ramakrishnan, R. Mueller, J. P. Poziemski, G. S. Miguel, L. J. Markoski, C. F. Zukoski, J. S. Moore, *Langmuir* **2006**, *22*, 6352.
- [39] C. C. Wu, M. D. Porter, *J. Electrochem. Soc.* **1987**, *134*, C504.
- [40] B. Marler, U. Oberhagemann, S. Vortmann, H. Gies, *Micropor. Mater.* **1996**, *6*, 375.
- [41] W. H. Zhang, J. L. Shi, L. Z. Wang, D. S. Yan, *Chem. Mater.* **2000**, *12*, 1408.
- [42] W. H. Zhang, J. L. Shi, H. R. Chen, Z. L. Hua, D. S. Yan, *Chem. Mater.* **2001**, *13*, 648.
- [43] C. Schiesser, U. Wille, H. Matsubara, I. Ryu, *Acc. Chem. Res.* **2007**, *40*, 303.
- [44] H. Winkler, A. Birkner, V. Hagen, I. Wolf, R. Schmechel, H. v. Seggern, R. A. Fischer, *Adv. Mater.* **1999**, *11*, 1444.
- [45] M. Kim, K. Sohn, H. B. Na, T. Hyeon, *Nano Lett.* **2002**, *2*, 1383.
- [46] A. Pines, M. G. Gibby, J. S. Waugh, *J. Chem. Phys.* **1973**, *59*, 569.
- [47] O. B. Peersen, X. L. Wu, I. Kustanovich, S. O. Smith, *J. Magn. Reson. A* **1993**, *104*, 334.
- [48] A. E. Bennett, C. M. Rienstra, M. Auger, K. V. Lakshmi, R. G. Griffin, *J. Chem. Phys.* **1995**, *103*, 6951.
- [49] M. Mehring, in *Principles of High Resolution NMR in Solids*, Springer, Berlin **1983**, Chapter 4.3.
- [50] G. E. Maciel, D. W. Sindorf, *J. Am. Chem. Soc.* **1980**, *102*, 7606.
- [51] D. W. Sindorf, G. E. Maciel, *J. Am. Chem. Soc.* **1983**, *105*, 3767.
- [52] G. E. Michael, D. W. Sindorf, V. J. Bartuska, *J. Chromatogr. A* **1981**, *205*, 438.
- [53] G. E. Maciel, in *Encyclopedia of Nuclear Magnetic Resonance*, Vol. 7 (Eds: D. M. Grant, R. K. Harris), John Wiley & Sons Ltd Chichester **1996**, 4370.

CHAPTER 3. STRUCTURALLY ORDERED MESOPOROUS CARBON NANOPARTICLES AS TRANSMEMBRANE DELIVERY VEHICLE IN HUMAN CANCER CELLS

¹A paper published in *Nano Letters*, **2008**, 8, 3724-3727

*Tae-Wan Kim*², *Po-Wen Chung*², *Igor I. Slowing*, *Makoto Tsunoda*, *Edward S. Yeung*, and *Victor S.-Y. Lin*³

Abstract

A structurally ordered, CMK-1 type mesoporous carbon nanoparticle (MCN) material was successfully synthesized by using a MCM-48 type mesoporous silica nanoparticle as template. The structure of MCN was analyzed by a series of different techniques, including the scanning and transmission electron microscopy (SEM and TEM), powder X-ray diffraction (XRD), and N₂ sorption analysis. To the best of our knowledge, no study has been reported prior to our investigation on the utilization of these structurally ordered mesoporous carbon nanoparticles for the delivery of membrane impermeable chemical agents inside of eukaryotic cells. The cellular uptake efficiency and biocompatibility of MCN with human cervical cancer cells (HeLa) were investigated. Our results show that the inhibitory concentration (IC₅₀) value of MCN is very high (> 50 µg/mL per million cells) indicating that MCN is fairly biocompatible *in vitro*. Also, a membrane impermeable fluorescence dye, Fura-2, was loaded to the mesoporous matrix of MCN. We demonstrated that the MCN

¹ Reprinted with permission of Americal Chemical Society

² Primary researcher and author

³ Author of correspondence

material could indeed serve as a transmembrane carrier for delivering Fura-2 through the cell membrane to release these molecules inside of live HeLa cells. We envision that further developments of this MCN material will lead to a new generation of nanodevices for transmembrane delivery and intracellular release applications.

Results and discussions

Recent developments in designing structurally defined carbonaceous nanoporous materials, such as single-walled carbon nanotubes (SWNTs), have shown potential for various biomedical and biotechnological applications, such as cell/tissue imaging, gene transfection, and drug delivery.¹⁻³ However, the hydrophobic nature of these materials often leads to a random agglomeration in water under physiological conditions. This problem severely complicates the biocompatibility, circulation, and endocytosis properties of these carbon-based nanomaterials *in vitro* or *in vivo*. To circumvent this aggregation issue, a key prerequisite is to control the surface properties and particle morphology of these materials for efficient uptakes by various cell types. While exciting progress has been made in functionalizing the graphitic surface of SWNT with water-soluble and biologically active moieties for cellular uptakes,¹⁻¹¹ to the best of our knowledge, no prior report on the endocytosis and biocompatibility of other structurally ordered carbonaceous nanoporous materials, such as ordered mesoporous carbons (OMCs).

The high surface area ($> 1000 \text{ m}^2/\text{g}$), large pore volume ($> 1 \text{ cm}^3/\text{g}$), and uniform mesoporous structures of OMC materials offer many advantages for biotechnological applications.¹²⁻¹⁸ However, the particle size and shape of most OMCs are not well defined. The conventional OMCs are amorphous polydisperse materials with a large average particle

size ($> 1 \mu\text{m}$), which cannot be endocytosed by live cells. Also, given that the typical size of OMCs is within the size window of bacteria, these materials could potentially trigger acute immune response *in vivo*. This morphological deficiency of OMCs derives from the fact that these carbonaceous materials are typically the replications from the hard template silicas with interconnecting mesopores. In general, OMC is prepared by infiltrating the mesopores of a silica template with a carbon precursor, followed by a high-temperature carbonization to yield a silica-carbon composite material.¹²⁻¹⁴ The silica template is later dissolved and removed under either acidic or basic conditions.¹²⁻¹⁴ Based on this synthetic approach, the morphology of OMCs is dictated by the size and shape of the silica “mold.”

To overcome this morphology issue and to develop an OMC material with high biocompatibility, we report herein on the synthesis of a monodisperse, CMK-1 type mesoporous carbon nanoparticle (MCN) material with an average particle size of 150 nm. As detailed below, we have discovered that MCN is biocompatible and could be efficiently endocytosed by human cervical cancer cells (HeLa). Furthermore, our experimental data indicated that this MCN material could serve as a transmembrane delivery vehicle for the intracellular release of a cell membrane impermeable fluorescence dye, Fura-2, inside human cervical cancer cells (HeLa) as depicted in Scheme 1. While we and other groups have demonstrated that mesoporous silica nanoparticles can serve as effective carriers for efficient transmembrane drug delivery,¹⁹⁻²⁸ mesoporous carbon nanoparticles have higher surface areas and pore volumes compared to mesoporous silicas, which are advantageous for drug loading. In addition, a recent report has shown that the cytotoxicity of carbon nanoparticles is lower than that of silica nanoparticles.^{29,30} In contrast to the hydrophilic silicate surface of mesoporous silicas, the surface of MCN is comprised of graphenes and is hydrophobic. Most

of hydrophobic drug molecules could be easily loaded inside of the mesoporous matrix of MCN in large quantities.

To prepare the MCN material, we first synthesized a MCM-48 type mesoporous silica nanoparticle (MSN) material as the structure-directing template via a modified Stöber method.³¹ Cetyltrimethylammonium bromide (CTAB; 1.0 g) and a triblock copolymer (Pluronic F127, EO₁₀₆PO₇₀EO₁₀₆; 4.0 g) were mixed in 298 mL of H₂O/NH₃/EtOH solution (NH₄OH(aq) (2.8 wt%) / EtOH = 2.5 / 1 (v/v)). Tetraethyl orthosilicate (TEOS; 3.6 g) was added into the solution at room temperature. After vigorous stirring for 1 min, the reaction mixture was kept under static condition for 1 d at room temperature for the complete condensation of silica. The resulting solid MSN product was isolated by centrifuge, washed with copious water, and dried at 70 °C in air. To synthesize MCN, the surface of MSN was first converted to an aluminosilicate form via a previously reported method.³² As described in the Experimental Section in supporting information, the aluminated MSN was infiltrated by furfuryl alcohol at room temperature, followed by polymerization and carbonization at elevated temperatures under vacuum. The silica template was removed by washing the composite with HF(aq) to yield the desired MCN material.

The structure of MCN was analyzed by a series of different techniques, including the scanning and transmission electron microscopy (SEM and TEM), powder X-ray diffraction (XRD), and N₂ sorption analysis. As depicted in Figure 1, the MCN material is consisted of monodisperse (100—200 nm) spherical nanoparticles. As showed in Figure 1a, the TEM micrograph of MCN showed the exact replication of the whole particle morphology (spherical particles). Also, a tetragonal *I4₁/a* (or lower) mesoporous structure, which is the replication of the cubic *Ia-3d* porous morphology of MSN template, was also observed in

Figure 1b. The high-magnification TEM images of MSN and MCN materials (Figure 1c and d) confirmed the highly ordered mesoporous structures throughout the entire particle of these materials. As depicted in Figure 2a, the XRD patterns of MSN and MCN further revealed the successful transformation from the cubic $Ia-3d$ (MCM-48 type) to the tetragonal $I4_1/a$ (or lower) mesoporous structure after the carbon replication process.³² The N_2 sorption isotherm (Figure 2b) exhibited two capillary condensation steps at $P/P_0 = 0.18-0.3$ and > 0.95 , which could be attributed to the N_2 condensation that took place at the internal mesopores and the interparticle voids, respectively. We found that MCN has large BET surface area (~ 2000 m^2/g) and pore volume (1.2 cm^3/g) (Table 1). The BJH pore size distribution showed an average pore diameter of 2.4 nm.

To investigate the cell membrane permeability of MCN, we introduced an aqueous suspension of MCN (10 $\mu g/mL$) to a culture ($\sim 1 \times 10^5$ cells) of human cervical cancer cells (HeLa) in D-10 media. The endocytosis of MCN was examined by a differential interference contrast (DIC) microscopy.³³ After 24 h incubation, DIC images (Figure 3) of the live cells with different focal depth along the Z-axis showed that MCNs (black aggregates) were indeed internalized by HeLa cells. The biocompatibility of MCN was evaluated by incubating HeLa cells with MCN suspensions of different concentrations ($0, 1, 10, 25$ and 50 $\mu g/mL$) in growth media for 48 h. These cells were analyzed by flow cytometry as detailed in the Experimental Section. Interestingly, no growth inhibition was found at concentrations below 10 $\mu g/mL$. As shown in Figure 4a, the high inhibitory concentration (IC_{50}) value (> 50 $\mu g/mL$ per million cells) indicated that MCN is very biocompatible *in vitro*.

To investigate the efficacy of using MCN as a transmembrane delivery carrier for intracellular release of drugs or other biogenic molecules, a cell membrane impermeable

fluorescent dye (Fura-2) was loaded into MCN to yield a composite material (Fura-2/MCN). As shown in Figure 4b, Fura-2 could indeed be released efficiently from MCN in D-10 medium. A fast release of Fura-2 was observed within the initial 20 min, followed by a slow concentration increase before reaching the plateau in 2 h. A large amount (10.6 $\mu\text{mol/g}$) of Fura-2 was released from MCN over the period of 2 h. These results suggested that the release of Fura-2 was governed by a simple diffusion process from a uniformed mesoporous matrix.

To investigate the property of intracellular release, the Fura-2/MCN nanoparticles were suspended in PBS (pH 7.4) at a concentration of 1 mg/mL. The suspension (150 μL) was added to a cell culture of HeLa in 3 mL growth media, followed by a 12 h incubation at 37 °C under 5% CO₂ atmosphere. The cells were then isolated, washed with copious PBS buffer, and transferred to a microscope slide with 20 μL fresh growth media for immediate observation under a confocal fluorescent microscope. As depicted in Figure 5a, the bright-field micrograph showed that the MCN particles were indeed internalized by HeLa cells and formed aggregates in the cytoplasm. The intense green fluorescence illustrated in the confocal fluorescence image (Figure 5b) clearly indicated that Fura-2 molecules were indeed delivered through the cell membrane of HeLa by MCN and were released inside the cells. To confirm this result, Fura-2 was introduced to the HeLa cell culture without the presence of MCN. The cells were examined under the same experimental condition by confocal fluorescence microscopy. No fluorescence was observed inside the cell bodies.

In conclusion, we have demonstrated that a structurally stable mesoporous carbon nanoparticle (MCN) material with high surface area and defined particle and pore morphology could be successfully synthesized. We discovered that this carbonaceous

nanoparticle material could efficiently penetrate the plasmic membrane of live HeLa cells with low cytotoxicity. Also, our data indicated that these MCN nanoparticles could serve as effective transmembrane delivery carriers for intracellular release of a cell-membrane impermeable fluorescence dye, Fura-2. We envision that further developments of this type of MCN materials will lead to a new generation of nanodevices for a variety of biotechnological and biomedical applications.

Acknowledgment

This study was supported by the U.S. National Science Foundation (CHE-0239570 and CHE-0809521) and the U.S. DOE Ames Laboratory through the office of Basic Energy Sciences under Contract No. DE-AC02-07CH11358.2.1.2 Second Hypothesis

Reference

1. Bianco, A.; Kostarelos, K.; Partidos, C. D.; Prato, M. *Chem. Commun.* **2005**, (5), 571-577.
2. Kam, N. W. S.; Dai, H. *Phys. Stat. Sol. B* **2006**, 243, (13), 3561-3566.
3. Liu, Y.; Wang, H. *Nature Nanotech.* **2007**, 2, (1), 20-21.
4. Pantarotto, D.; Briand, J.-P.; Prato, M.; Bianco, A. *Chem. Commun.* **2004**, (1), 16-17.
5. Kam, N. W. S.; Jessop, T. C.; Wender, P. A.; Dai, H. *J. Am. Chem. Soc.* **2004**, 126, (22), 6850-6851.
6. Kam, N. W. S.; Dai, H. *J. Am. Chem. Soc.* **2005**, 127, (16), 6021-6026.
7. Bottini, M.; Cerignoli, F.; Dawson, M. I.; Magrini, A.; Rosato, N.; Mustelin, T. *Biomacromolecules* **2006**, 7, (8), 2259-2263.
8. Kam, N. W. S.; Liu, Z.; Dai, H. *Angew. Chem. Int. Ed.* **2006**, 45, (4), 577-581.
9. Feazell, R. P.; Nakayama-Ratchford, N.; Dai, H.; Lippard, S. J. *J. Am. Chem. Soc.* **2007**, 129, (27), 8438-8439.
10. Liu, Z.; Sun, X.; Nakayama-Ratchford, N.; Dai, H. *ACS Nano* **2007**, 1, (1), 50-56.
11. Liu, Y.; Wu, D.-C.; Zhang, W.-D.; Jiang, X.; He, C.-B.; Chung, T. S.; Goh, S. H.; Leong, K. W. *Angew. Chem. Int. Ed.* **2005**, 44, (30), 4782-4785.
12. Ryoo, R.; Joo, S. H.; Kruk, M.; Jaroniec, M. *Adv. Mater.* **2001**, 13, (9), 677-681.
13. Ryoo, R.; Joo, S. H. *Stud. Surf. Sci. Catal.* **2004**, 148, 241-260.
14. Lee, J.; Kim, J.; Hyeon, T. *Adv. Mater.* **2006**, 18, (16), 2073-2094.
15. Hartmann, M. *Chem. Mater.* **2005**, 17, (18), 4577-4593.

16. Vinu, A.; Miyahara, M.; Mori, T.; Ariga, K. *J. Porous Mater.* **2006**, 13, (3-4), 379-383.
17. Vinu, A.; Hossain, K. Z.; Satish Kumar, G.; Ariga, K. *Carbon* **2006**, 44, (3), 530-536.
18. Ariga, K.; Vinu, A.; Miyahara, M.; Hill, J. P.; Mori, T. *J. Am. Chem. Soc.* **2007**, 129, (36), 11022-11023.
19. Radu, D. R.; Lai, C.-Y.; Jeftinija, K.; Rowe, E. W.; Jeftinija, S.; Lin, V. S. Y. *J. Am. Chem. Soc.* **2004**, 126, (41), 13216-13217.
20. Giri, S.; Trewyn, B. G.; Stellmaker, M. P.; Lin, V. S. Y. *Angew. Chem., Int. Ed.* **2005**, 44, (32), 5038-5044.
21. Slowing, I.; Trewyn, B. G.; Lin, V. S.-Y. *J. Am. Chem. Soc.* **2006**, 128, (46), 14792-14793.
22. Slowing, I. I.; Trewyn, B. G.; Giri, S.; Lin, V. S. Y. *Adv. Funct. Mater.* **2007**, 17, (8), 1225-1236.
23. Slowing, I. I.; Trewyn, B. G.; Lin, V. S. Y. *J. Am. Chem. Soc.* **2007**, 129, (28), 8845-8849.
24. Torney, F.; Trewyn, B. G.; Lin, V. S. Y.; Wang, K. *Nat. Nanotechnol.* **2007**, 2, (5), 295-300.
25. Slowing, I. I.; Vivero-Escoto, J. L.; Wu, C.-W.; Lin, V. S. Y. *Adv. Drug Delivery Rev.* **2008**, 60, (11), 1278-1288.
26. Liu, H.-M.; Wu, S.-H.; Lu, C.-W.; Yao, M.; Hsiao, J.-K.; Hung, Y.; Lin, Y.-S.; Mou, C.-Y.; Yang, C.-S.; Huang, D.-M.; Chen, Y.-C. *Small* **2008**, 4, (5), 619-26.
27. Lu, J.; Liong, M.; Sherman, S.; Xia, T.; Kovichich, M.; Nel, A. E.; Zink, J. I.; Tamanoi, F. *NanoBiotechnology* **2007**, 3, (2), 89-95.
28. Lu, J.; Choi, E.; Tamanoi, F.; Zink, J. I. *Small* **2008**, 4, (4), 421-426.
29. Yan, A.; Lau, B. W.; Weissman, B. S.; Kulaots, I.; Yang, N. Y. C.; Kane, A. B.; Hurt, R. H. *Adv. Mater. (Weinheim, Ger.)* **2006**, 18, (18), 2373-2378.
30. Xu, Z. P.; Zeng, Q. H.; Lu, G. Q.; Yu, A. B. *Chem. Eng. Sci.* **2006**, 61, (3), 1027-1040.
31. Schumacher, K.; Ravikovitch, P. I.; Du Chesne, A.; Neimark, A. V.; Unger, K. K. *Langmuir* **2000**, 16, (10), 4648-4654.
32. Kim, T.-W.; Solovyov, L. A. *J. Mater. Chem.* **2006**, 16, (15), 1445-1455.
33. Li, H.-W.; McCloskey, M.; He, Y.; Yeung, E. S. *Anal. Bioanal. Chem.* **2007**, 387, (1), 63-69.

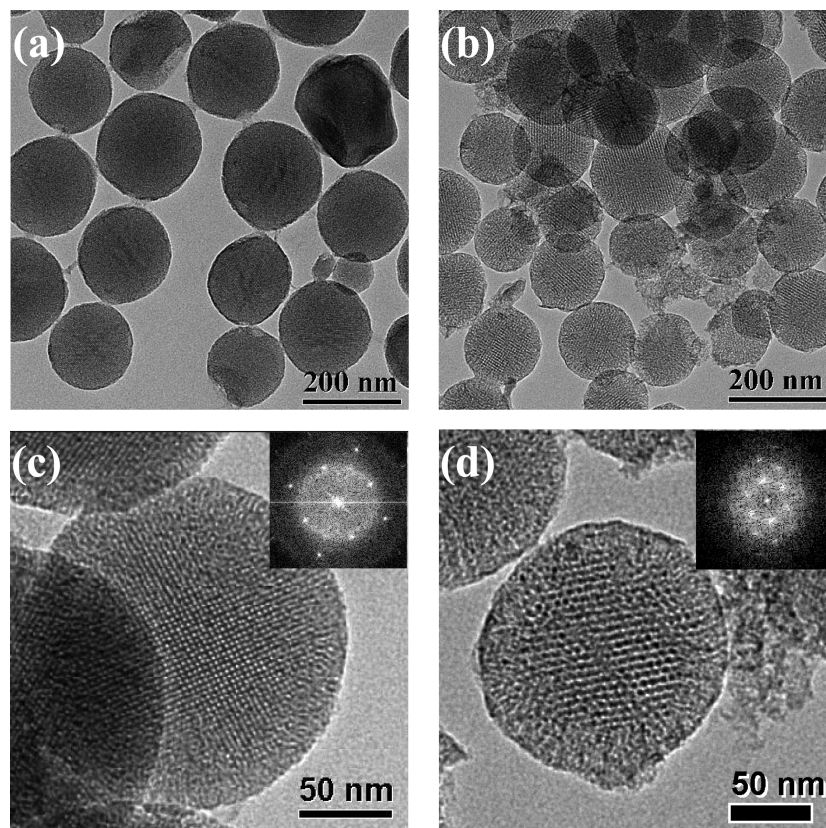


Figure 1. Low magnification TEM images of (a) mesoporous silica MCM-48 nanoparticles and (b) mesoporous carbon nanoparticle (MCN) materials. High magnification TEM images of (c) MCM-48 nanoparticle and (d) MCN material with the corresponding Fourier diffactograms (insets).

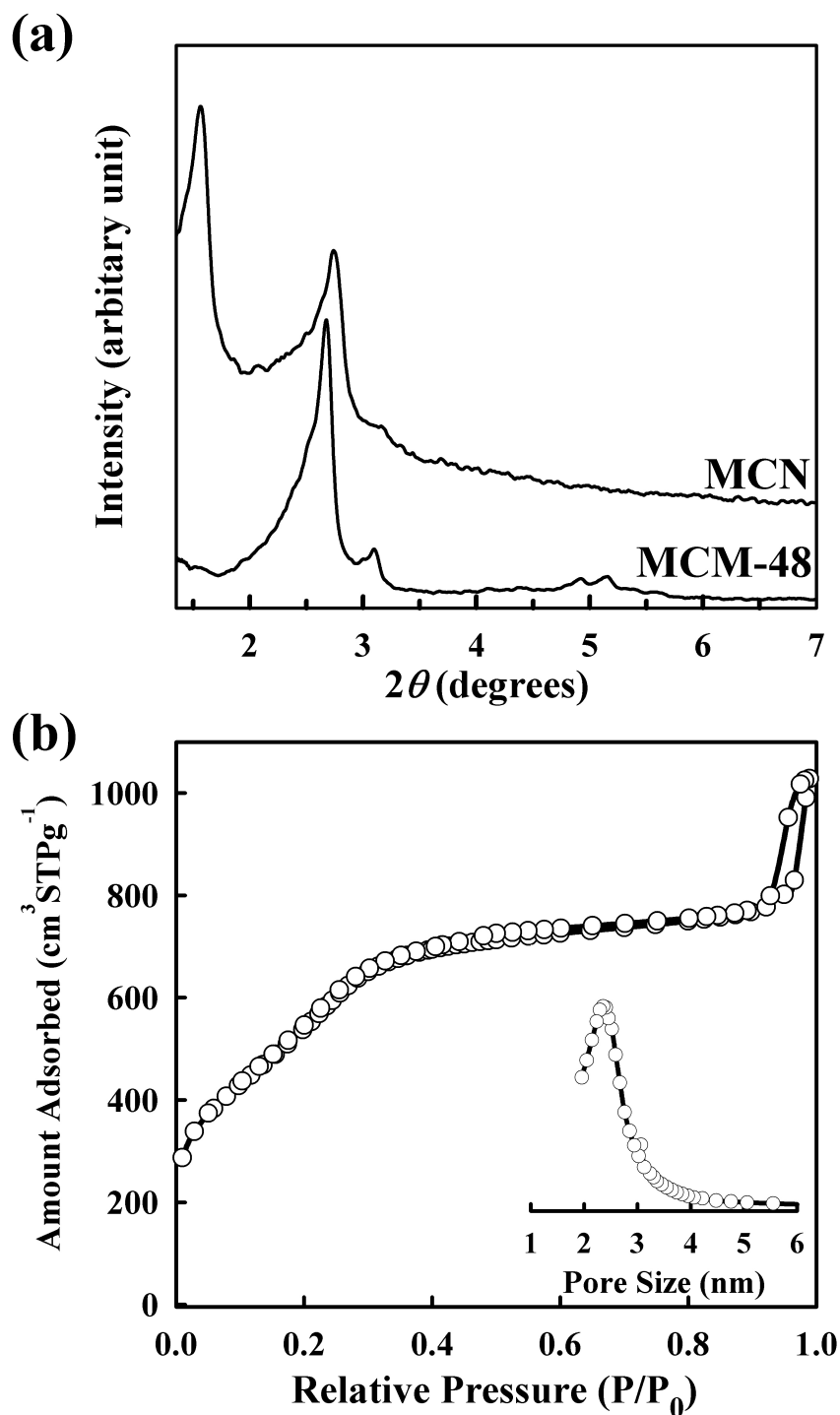


Figure 2. (a) Powder XRD patterns of MCN (top) and the calcined, MCM-48 type MSN silica template (bottom). (b) N_2 sorption isotherm and the pore size analysis with adsorption branch using the BJH algorithm (inset) of MCN.

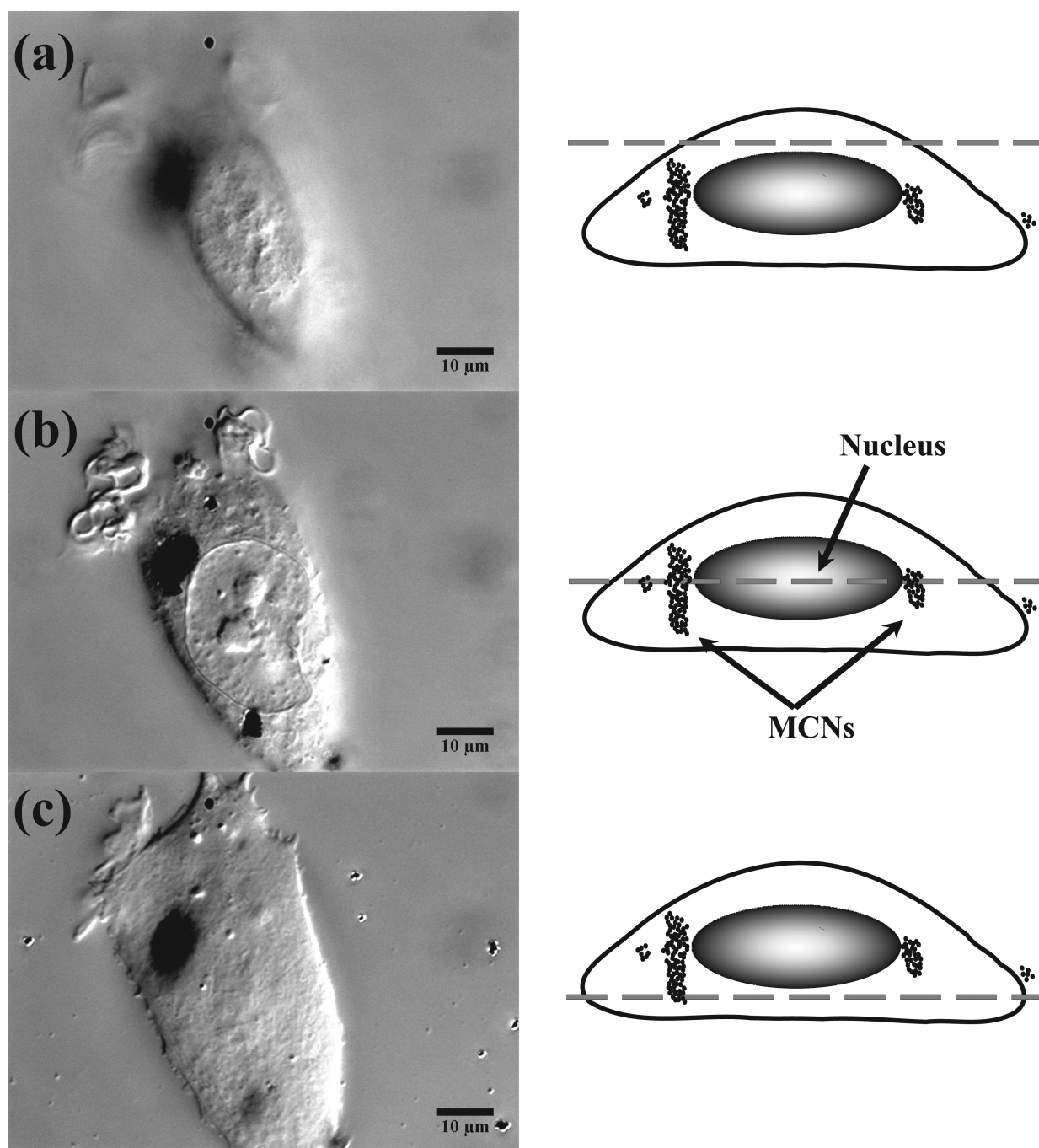


Figure 3. DIC micrographs and schematic representations of MCNs endocytosed by a HeLa cell. The focal plane was varied along the Z-axis from the top a) to bottom c) of the cell.

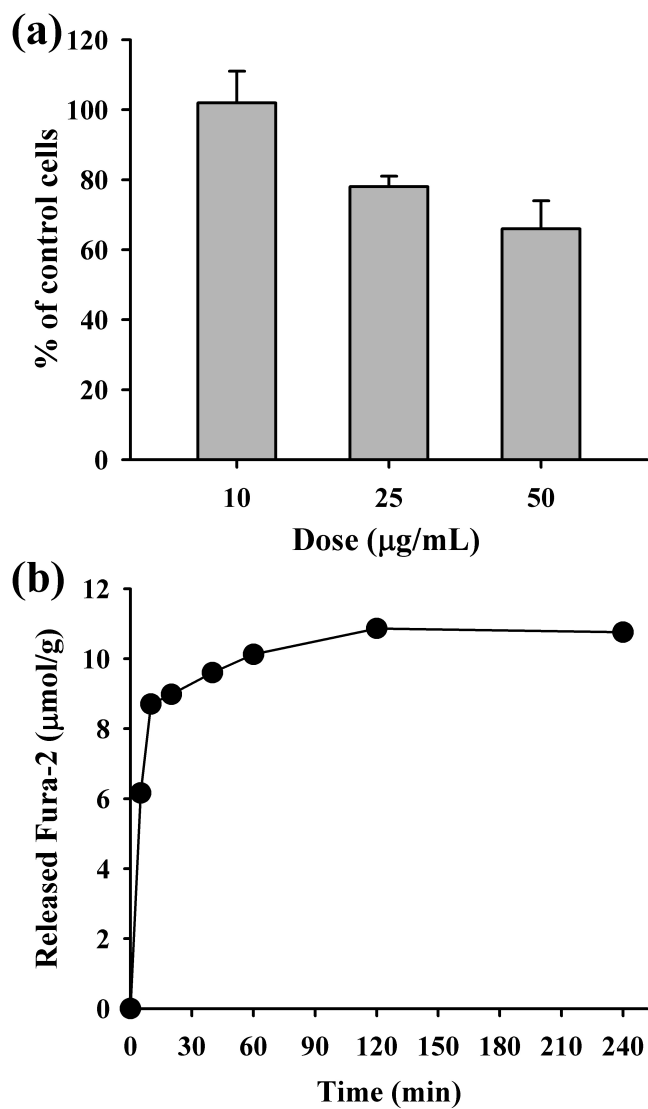


Figure 4. (a) Viability test of HeLa cells with different concentrations of MCN after 48 h incubation. (b) Release profile of Fura-2 fluorescein from MCNs in D-10 medium at room temperature.

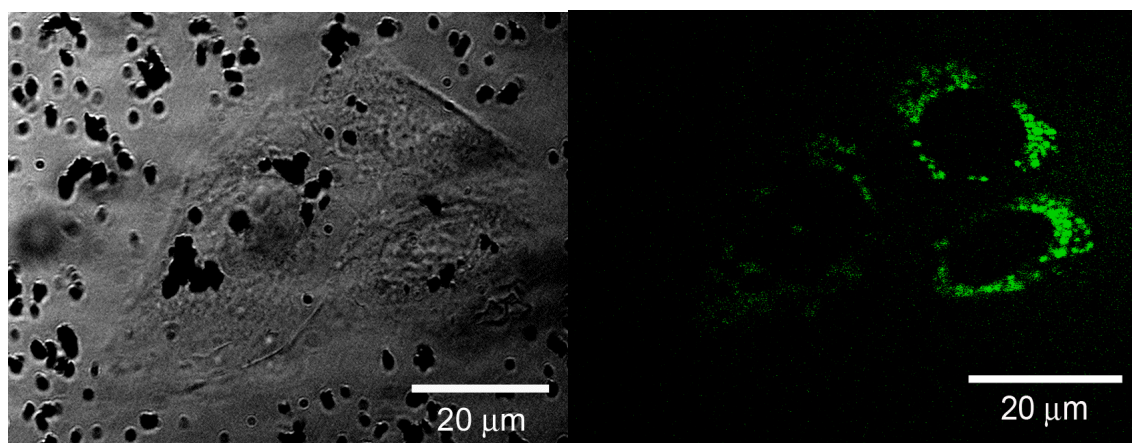
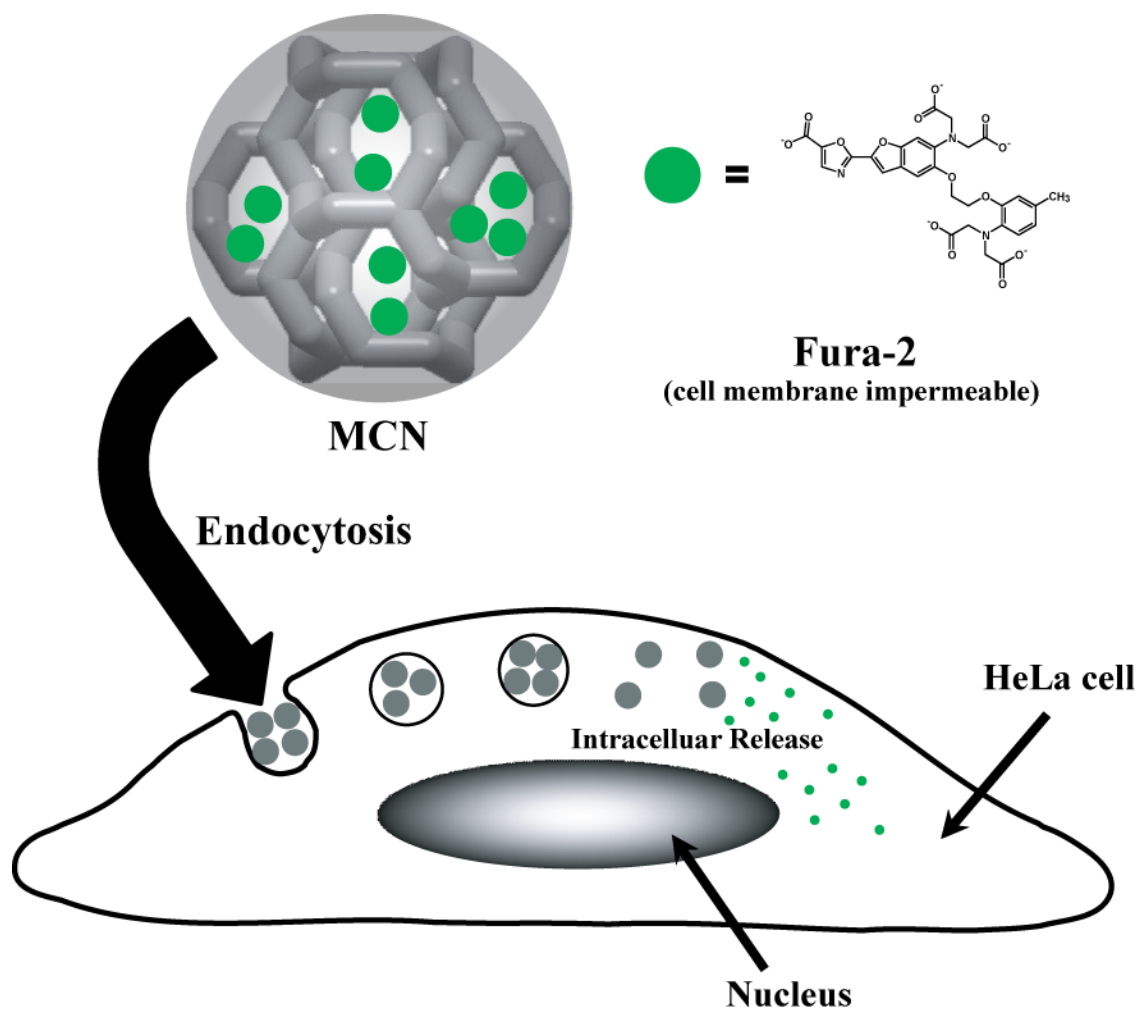


Figure 5. (a) Brightfield image and (b) confocal fluorescence microscopy image of Fura-2/MCN containing HeLa cells.



Scheme 1. Schematic representation of the endocytosis of mesoporous carbon nanoparticles (MCNs) and the intracellular release of Fura-2 molecules.

Table 1. Structural properties of MCM-48 mesoporous silica nanoparticles and ordered mesoporous carbon nanoparticle MCNs from nitrogen adsorption data.^a

Sample	S_{BET} [m ² g ⁻¹]	V_t [cm ³ g ⁻¹]	w_{BJH} [nm]
MCM-48	1278	0.96	2.3
MCN	2034	1.2	2.4

^a S_{BET} - the BET specific surface area calculated in the range of relative pressures from 0.05 to 0.2; V_t - the total pore volume calculated at the relative pressure of about 0.95; w_{BJH} - the diameter of mesopores calculated using the BJH method.

Supporting Information

Experimental Section

Materials

Preparation of aluminosilicate MCM-48: For synthesis of OMC, the silica was converted to an aluminosilicate form using a solution of AlCl₃ following the post-synthesis procedure: as-synthesized MCM-48 material was calcined at 550 °C to remove the surfactant. The calcined sample was mixed with distill water to make surface silanol groups, and then completely dried at 150 °C. The dried sample was slurried in ethanol solution of the anhydrous AlCl₃ (Si/Al = 20). The ethanol solvent was completely evaporated by rotary evaporator. The dried sample was calcined again at 550 °C.

Preparation of MCN

Ordered mesoporous carbon nanoparticles MCNs were prepared using furfuryl alcohol (Aldrich) as a carbon source. 1g of aluminated MCM-48 nanoparticles were infiltrated with 0.91 mL of furfuryl alcohol by impregnation method. The mixture was moved into Schlenk reactor, and subjected to freeze-vacuum-thaw three times using liquid N₂. The mixture was kept under vacuum at 35 °C for 1 h. After opened schlenk reactor, the mixture was heated for 6 h at 100 °C for polymerization of furfuryl alcohol, and then partially carbonized at 350 °C for 3 h under vacuum. After cooled to room temperature, the sample was added with 0.58 mL of furfuryl alcohol, and repeated freeze-vacuum-thaw and polymerization again. Further carbonization was accomplished by heating to 900 °C under vacuum condition. The carbon product was collected by HF washing. (10 wt% HF in EtOH/H₂O solution)

Measurement of ordered mesoporous nanoparticles

XRD patterns were recorded on a Scintag XDS-2000 instrument operated at 1.21 kW, using Cu K α radiation. The nitrogen adsorption isotherms were measured at liquid nitrogen temperature (77 K) using a Micromeritics ASAP2000 volumetric adsorption analyzer. The Brunauer-Emmett-Teller (BET) equation was used to calculate the apparent surface area from adsorption data obtained at P/P₀ between 0.05 and 0.2. The total volume of micro- and mesopores was calculated from the amount of nitrogen adsorbed at P/P₀ = 0.95, assuming that adsorption on the external surface was negligible compared to adsorption in pores. The pore size distributions (PSD) were calculated by analyzing the adsorption branch of the N₂ sorption isotherm using the Barret-Joyner-Halenda (BJH) method. SEM images and energy dispersive X-ray (EDX) analysis were obtained with a JEOL 840A scanning electron microscope operating at 10 kV. The SEM samples were coated with gold before SEM measurement. TEM images were taken on a copper grid supported with carbon film, using a Tecnai G2 F20 equipment operated at 200 kV.

Endocytosis experiments

DIC microscopy of HeLa cells with MCN: For DIC microscopy measurement, HeLa cells were incubated in Dubelcco's Modified Eagle Medium supplemented with 10% horse serum, gentamicin, penicillin, streptomycin and L-alanylglutamine (D-10) at 37 °C in 5% CO₂. The cells were seeded at 0.5×10^5 cells/mL in six-well plates containing 3 mL of D-10 and glass coverslips in the bottom. The cells were incubated for 24 hours in order to attach. After attachment the D-10 medium was replaced with a suspension of 10 g/mL of MCN in D-10 and incubated for times ranging from 3 to 24 hours. After the desired time the media was removed, the coverslips were washed with fresh D-10 media and set upside down on top of microscope slides provided with 0.15 mm thick spacers (Secure-Seal, Grace BioLabs, Inc. Bend, OR) and 15 mL of D-10. The slides were then examined by DIC microscopy.

The system used for DIC microscopy consisted of an upright Nikon Eclipse 80i microscope equipped with DIC prisms, 1.4 NA condenser, and 100×/1.40 NA DIC Plan Apo objective. A CCD (CoolSNAP ES, Photometrics, Tucson, AZ, USA, pixel size 6.45 mm) camera was mounted on top of the microscope. Winview 32 (Roper Scientific, Princeton, NJ, USA) was used for image collection and data processing.

Viability test (Flow Cytometry)

Cell proliferation and viability of the HeLa cells in the presence and absence of MCN were studied by Guava ViaCount assay (Guava Technologies, Inc.; Hayward, CA). HeLa cells were seeded in three six-well plates at a density of 1×10^5 cells/mL in 3 mL of D-10 medium and were incubated at 37 °C and 5% CO₂ for 24 hours for attaching. After that the media was removed from all the wells and replaced with D-10 containing different concentrations of MCN (0, 1, 10, 25 and 50 µg/mL). Each concentration was tested in triplicate. After addition of the MCN suspensions the plates were set back in the incubator at 37 °C and 5% CO₂ for 48 additional hours. After that time the media was removed from each well and the cells were washed two times with phosphate buffered saline solution (pH

7.2), they were harvested by trypsinization into 15 mL tubes and centrifuged at 1000 rpm for 10 minutes. The supernatant was discarded and the cells were resuspended in 1 mL of fresh D-10 medium. The cells in the resuspended media were then counted and their viability determined by the Guava ViaCount cytometry assay.

Fura-2 release test

Fura-2 (1.0 mg, Aldrich) was dissolved in 1.33 mL PBS in a 1.5 mL centrifuge tube. MCN (1.4 mg) was added to 0.75 mL of PBS solution and sonicated for 5 min. After addition of 0.75 mL of Fura-2 in PBS to MCN in PBS, the mixture was sonicated for 5 additional min. After that the mixture was stirred for 1 hour. The final mixture was then centrifuged for 10 min at 14000 rpm and dried under vacuum overnight at room temperature. HeLa cells were seeded at the density of 0.5×10^5 cells/mL in 6 well plates and allowed to attach for 24 h in 3 mL of D-10 medium. A suspension of Fura-2 loaded MCN material (1 mg/mL in PBS; 150 μ L) was then added to each well and the cells were set in the incubator for additional 12 h at 37 °C and 5% CO₂. The media was then removed, the coverslips were washed twice with PBS and set upside down on top of microscope slides provided with 0.15 mm thick spacers (Secure-Seal, Grace BioLabs, Inc. Bend, OR) and 20 μ L of D-10. The slides were then examined by confocal fluorescence microscopy. The brightfield images were obtained with a CCD camera and the confocal fluorescence images were taken with a Leica TCS NT confocal system with a 0.35 micron resolution in the z-axis. For the fluorescence imaging the sample was excited with a UV laser (340-365 nm) and the acquisition was obtained with a 525/50 bandpass filter.

Release profile of Fura-2 from MCN in D-10 medium was carried out at room temperature without HeLa cell using the same amount of Fura-2 and MCN. The Fura-2/MCN in medium solution was centrifuge at predetermined time and the supernatant was collected. The concentration and amount of Fura-2 in D-10 medium was determined using the fluorometer (FluoroMax-2, Instruments S.A., Inc.).

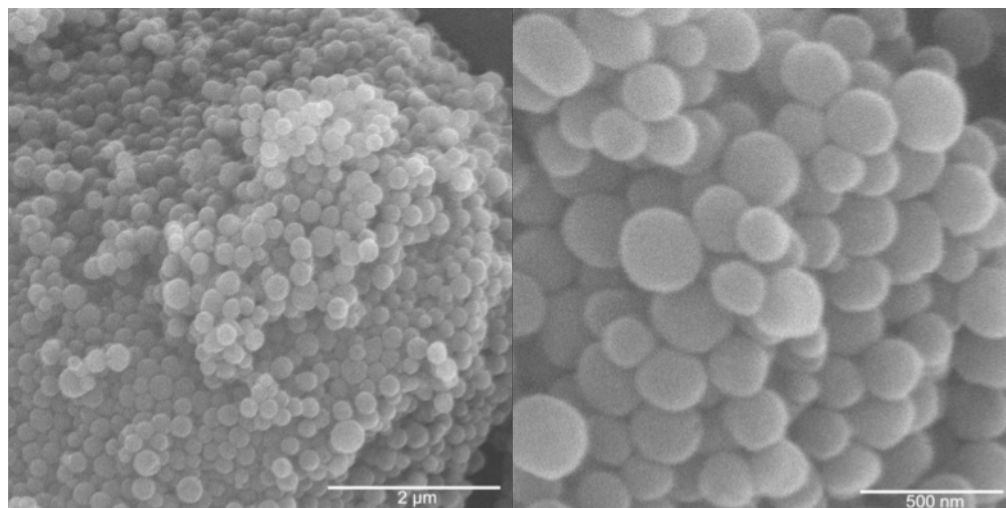


Figure S1. Calcined ordered mesoporous MCM-48 silica nanoparticles. (a) low and (b) high magnification of SEM.

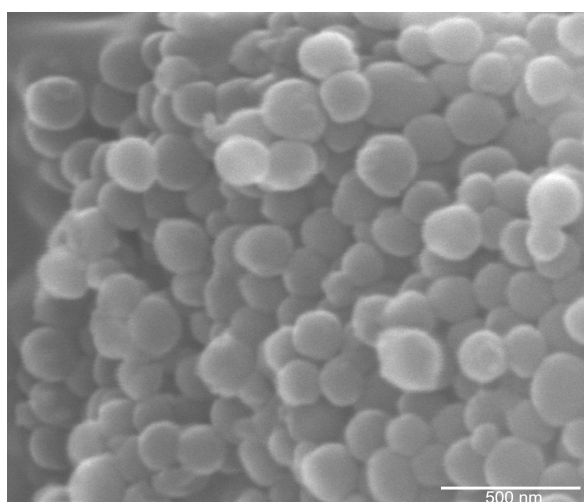


Figure S2. SEM image of the ordered mesoporous carbon MCN materials.

Table S1. EDX quantification of MCN

Element	Atomic %
C	90.73
O	9.11
Si	0.02
Cu	0.13

CHAPTER 4. ORDERED MESOPOROUS CARBON NANOPARTICLES AS A SUPPORT FOR THE CONVERSION OF SYNGAS TO ALCOHOL

A paper to be submitted *Journal of the America Chemical Society*

*Po-Wen Chung, Tae-Wan Kim, Yulin Hunag, Weihua Deng, Robert Brown, Victor S.-Y. Lin**

Abstract

The catalytic conversion of synthesis gas (syngas, CO/H₂) obtained by gasification of coal or biomass has attracted much attention in the past few years, owing the growing demand for oxygenated products, especially ethanol, which can be used a fuel additive and an energy carrier. Due to the unique carbon monoxide adsorption behavior on Rh, Rh-based catalysts mainly supported by inorganic oxides have been applied to selectively produce the C₂₊ oxygenates with high activity. However, methane is the most thermodynamically favored product of the CO hydrogenation and is unlikely to be suppressed unless the size and the dispersion of catalytic metal particles are well regulated over the support. Herein, mesoporous carbon nanoparticle (MCN) possessing well-ordered mesoporosity was developed in Lin group, and ordered mesoporous carbon material was unprecedentedly introduced as a support for the conversion of syngas to alcohol. The catalyst (Rh-Mn/MCN) was characterized by a series of different techniques, including transmission electron microscopy (TEM), powder X-ray diffraction (XRD), N₂ sorption analysis, and X-ray photoelectron spectroscopy (XPS) and the catalytic performance was tested in both micro-tubular reactor and pilot-scale fixed bed reactor. Indeed, Rh-Mn/MCN exhibited interesting

impact on the suppression of the selectivity of methane and it could be attributed to favorable diffusivity confined by the mesoporosity of MCN.

Introduction

Dwindling petroleum resources, combined with an increased demand for petroleum by emerging economies, as well as environmental concerns about fossil fuels are driving researchers to look for new sources of fuel alternatives.¹ Ethanol has been used widely as both an energy carrier and a fuel additive.² The catalytic conversion of synthesis gas (syngas, CO/H₂) obtained by gasification of coal or biomass has attracted much attention in the past few years, owing the growing demand for oxygenated products, particularly C₂ oxygenates such as ethanol, acetaldehyde, and acetic acid.³ Rh-based catalysts have been applied to selectively produce the C₂₊ oxygenates with high activity due to the unique carbon monoxide adsorption behavior on Rh.⁴⁻⁷ It is concluded that CO hydrogenation is a structure-sensitive reaction, meaning that the product distribution strongly relies on the metal components, the size of metal particles, the distribution of metal particles over the support and the nature of support.^{8,9} Extensive research efforts have been devoted to investigate the influence of supports and additives including La₂O₃, SiO₂, TiO₂, Al₂O₃, ZrO₂, CeO₂, MgO, V₂O₃, alkali metals, Fe, Mn, Ag and Mo on the catalytic activity of Rh for CO hydrogenation. In addition, porous silica supported Rh catalysts were found to affect the catalytic activity and selectivity significantly owing to the control of the size and the distribution of Rh particles.¹⁰

It is widely concluded that CO dissociation and hydrogenation to produce CH_x species is likely the first step for the synthesis of C₂₊ oxygenates from syngas on Rh-based catalyst.

Then the CH_x species can go through three possible reactions: the formation of C_2 oxygenates by CO insertion, the production of CH_4 by hydrogenation, and the chain growth with another CH_x to produce C_{2+} hydrocarbons.¹¹ Methane is the most thermodynamically favored product and is undesirable economically. In order to suppress methane production and improve the selectivity toward C_{2+} oxygenates, metal dispersion over the supports has a striking influence for CO hydrogenation.¹²

Carbon is able to exhibit different properties compared to conventional refractory oxide such as Al_2O_3 and SiO_2 .¹³ Recently Bao's group has demonstrated that carbon nanotubes containing catalytic particles is capable of improving the ethanol production for CO hydrogenation due to the favorable thermal and electron conductive properties, as well as defined nanochannel morphology.¹⁴ However, no other carbonaceous materials have been employed as supports for CO hydrogenation.

It has been well studied that on graphitic carbonaceous materials, alloy surfaces can be created which cannot be produced on refractory oxides. That is, there is always metal segregation instead of alloy phase formation on refractory oxides. Second, on properly prepared carbonaceous materials, it is likely to directly bond the metal to carbon atoms in surface, meaning it can also create sintering-resistant metal particles of a unique structure and catalytic potential.¹³ Herein, a structurally ordered, CMK-1 type mesoporous carbon nanoparticles (MCN) was successfully developed by Lin's group¹⁵ and used to support catalytic particles via surface mediated organometallic reaction. After subsequent functionalization, Rh-Mn/MCN possesses highly-ordered tetragonal mesoporous structure as well as MCN and metal catalysts are well-dispersed inside the mesopores. The curved mesoporosity of Rh-Mn/MCN might not only provide a well-confined environment for metal

catalysts but also quickly dissipate the local heating generated from the extremely exothermic C_{2+} oxygenate formation. Therefore, we also reported the reactivity and selectivity of CO hydrogenation reaction over Rh-Mn/MCN, which was investigated both in micro-tubular reactor and pilot scale fix-bed reactor.

Results and Discussion

Mesoporous carbon nanoparticles (MCN) were first prepared *via* hard-template synthesis developed in Lin group. The MCN material is consisted of monodisperse (100–200 nm) spherical nanoparticles, possessing a highly ordered mesoporous structures ($I4_1/a$) and a narrowly distributed pore diameter (2.3 nm) throughout the entire particle. It has been well known that carbon based materials are highly hydrophobic and chemical treatment or modification on the surface of carbonaceous materials was found to be useful for manipulating their hydrophobic or hydrophilic character.¹⁶ Furthermore, there is a strong interaction observed between the metals and the functional groups generated by oxidation on the surface of carbonaceous materials.¹⁷ Among a variety of chemical treatments on carbon based materials, oxidation with nitric acid is the most effective one. Abundant carboxylic acid groups will be created and assist the coordination of metal precursors through the oxygen atoms on the surface of carbon materials.¹⁸ In order to obtain the highly dispersed Rh-Mn nanoparticles, MCN was carried out in concentrated nitric acid to produce carboxylic acids on the surface (COOH-MCN), followed by the deprotonation in sodium carbonate solution (COONa-MCN). Through surface mediated organometallic reaction,¹⁹ COONa-MCN was reacted with Rh(I) complex in toluene, followed by the addition of manganese

nitrate ethanolic solution under nitrogen. The metal complex MCNs were subsequently reduced at 300°C under hydrogen gas flow to obtain Rh-Mn/MCN. (Scheme 1.)

In order to investigate the catalytic reactivity, we tested the CO hydrogenation catalyzed by the Rh-Mn/MCN under the pressure of 450 psi at 300°C with a total flow rate 33 mL/min ($H_2/CO=2/1$) in a high-pressure micro-tubular reactor. (Figure 6.) All the gas/liquid products generated from the reaction were analyzed by GC. As shown in task 5 of Table 1., we discovered that no significant methane production was observed in GC analysis. In addition, Rh-Mn/MCN exhibited considerable selectivity toward C_{2+} oxygenates after reaction for 21 hr. Moreover, we also demonstrated the catalytic performance by using pilot-scale fixed bed reactor, which is collaborated with Dr. Brown's group. (Figure. x)

The results from task 1 to task 4 in Table 1 are collected by pilot-scale fixed bed reactor. (describe a bit about exp) Based the results from task 1 to task 3, we discovered that the space time yield (STY) of C_{2+} oxygenate is highly correlated to the gas hourly space velocity (GHSV). The higher GHSV is, the less the formation of C_{2+} oxygenates. (Figure. 1a) However, there is no methane production with lower CO conversion in task 3, which was carried out with the highest GHSV. It could be attributed to the short contact between the adsorbents and catalytic metal particles, meaning that there is no huge quantity of dissociative CO adsorption taking place on metal particles for the formation of active CH_x species, followed by the CO insertion to produce C_{2+} oxygenates. Therefore, task 1 has the highest observed STY of C_{2+} oxygenates owing to the lowest GHSV. As aforementioned, methane is the most thermodynamically favored product and will increase while increasing reaction temperature; nevertheless, the selectivity toward methane production appeared not to increase over Rh-Mn/MCN while the temperature was elevated from 300°C to 325°C. In

addition, the STY of C_{2+} oxygenates of Rh-Mn/MCN also increases at higher temperature while CO conversion did not vary so much. (Figure. 1b) The change of selectivity could be attributed to the diffusivity of gas and/or products in the meso-pores of carbonaceous materials.²⁰ If the diffusion rate is high enough, the heat produced from the extremely exothermic CO hydrogenation on the active sites might be removed effectively through the well-ordered pores, resulting in prevention of local overheating inside the catalyst. In addition, owing to the hydrophobic nature of carbonaceous materials, the hydrophilic products such as methanol, ethanol and propanol could be easily transported through the catalyst system. To understand more how Rh-Mn/MCN affect the catalytic performance, Rh-Mn/MCN was characterized by a series of different techniques, including transmission electron microscopy (TEM), powder X-ray diffraction (XRD), N_2 sorption analysis, and X-ray photoelectron spectroscopy (XPS).

Many research activities have been investigated to understand the influence of the catalyst nature on the catalytic performance. Among those factors, the size and the dispersion of metal particles over the supports are of great importance because CO hydrogenation is a structure-sensitive reaction.^{8,9} In general, reactions involving either bond breaking or formation of carbon-carbon bond are usually structure sensitive, implying that the formation of supported particles with suitable size should be critical to enhance the catalytic activity and selectivity to C_2 oxygenates.²¹ From the reported results, higher CO conversion and C_2 -oxygenates selectivity were obtained over Rh particles between 2-6 nm.⁹ As shown in Figure 1(a), in spite of successive functionalization on the surface of MCN, Rh-Mn/MCN possessed monodisperse spherical particles and highly ordered mesoporous structure without obvious dark spots indicating the location of metal particles under low magnification of TEM bright

field mode. We assumed the metallic particles are too small to be observed under TEM bright field mode. However, Rh-Mn nanoparticles would be likely to be scoped under STEM (scanning transmission electron microscopy) mode, which is highly sensitive to the discrepancy among light and heavy elements. Consequently, as shown in HAADF-STEM (high angle annular dark field) micrographs (Figure 2(a).), Rh-Mn nanoparticles are able to exhibit stronger contrast than carbon support and are distinguishable from MCN. The size of Rh-Mn nanoparticles is 2-3 nm in diameter and the Rh-Mn nanoparticles are well allocated over MCN. This homogeneous dispersion of Rh-Mn nanoparticles over MCNs is likely to be attributed to the surface mediated organometallic reaction.

After catalytic reaction, the growth of Rh-Mn nanoparticles is noteworthy as shown in Figure 2(b).. The size of Rh-Mn nanoparticles before syngas reaction was 2-3 nm large in diameter and some of them increased up to 6 nm after reaction (Figure 2(b).) owing to the thermal sintering along with high temperature reaction. However, most of the nanoparticles have maintained the size 2-3nm, which is about the size of the pore diameter. (Figure 2(a) and 2(b).) Although some metal particles have grown larger than the pore size, neither the TEM images nor BET isotherms (shown below) provide evidence for destruction of the porous structure of MCN. After the sample was ultramicrotomed into 60 nm thick slices, the distribution of Rh-Mn nanoparticle inside the mesopores was illustrated in Figure 1(c).. It was found that those metal particles were highly dispersed over MCN. Herein, it appears that the growth of most Rh-Mn nanoparticles is confined by the pore diameter, which is consistent with the conclusion reported in literature.^{9,22} They have discovered that the catalytic particles are uniformly deposited inside the support pores and limited by the pore size. To our knowledge, thermal sintering processes involve either migration of adatoms of

metal (Ostwald ripening) or migration and coalescence of metal nanoparticles. Metal nanoparticles of the size range investigated here are quite mobile even at room temperature.²³ Therefore, it comes out that the circuitous pore arrangements within the spherical MCN assisted to restrict the mobility of Rh-Mn nanoparticles and prevent them from a high degree of sintering.²³

In order to confirm that the porous structure of Rh-Mn/MCN is unlikely to be damaged after consecutive surface functionalization and is well preserved after catalytic reactions, the nitrogen sorption properties of Rh-Mn/MCN(rxn) (after catalytic reaction) as well as Rh-Mn/MCN, COOH-MCN and MCN were analyzed. As summarized in Table 2., the total surface areas and the average pore diameters were determined by the Brunauer–Emmett–Teller (BET) and Barrett–Joyner–Halenda (BJH) methods, respectively. The BET isotherms of these four materials exhibited the characteristic Type IV adsorption/desorption pattern, indicating the presence of highly ordered mesoporous structure. (Figure 3.) In addition, Rh-Mn/MCN still exhibited high surface area ($>1400 \text{ cm}^2\text{g}^{-1}$) and high pore volume ($>0.8 \text{ cm}^3\text{g}^{-1}$). Nevertheless, it is worth mentioning that the surface area of Rh-Mn/MCN(rxn) decreased as shown above in Figure 3.. Rh-Mn nanoparticles would grow as a result of thermal sintering and were likely to be restricted by the porous structure of MCN, meaning that the size of Rh-Mn nanoparticles is likely to be limited as large as pore diameter. Therefore, the decrease of surface area and total pore volume could be attributed to the partially impeded pore accessibility by Rh-Mn nanoparticles. In addition, Rh-Mn/MCN(rxn) possessed narrow pore size distribution as well as Rh-Mn/MCN, indicating that catalytic sites were mostly distributed inside the pores.

Figure 4. demonstrated power X-ray diffraction patterns of MCN, COOH-MCN, Rh-Mn/MCN and Rh-Mn/MCN(rxn). (top to bottom, respectively) After oxidation with nitric acid, COOH-MCN still possessed the three characteristic peaks (110), (211) and (220) of CMK-1, the same as MCN, indicating that carboxylic acid functionality did not alter the pore symmetry of MCN after oxidation. On the other hand, the intensities of Rh-Mn/MCN and Rh-Mn/MCN(rxn) decreased dramatically after the immobilization of Rh-Mn nanoparticles and syngas reaction. The decrease could be attributed to the partial pore-filling effect caused by the growth of Rh-Mn nanoparticles, which is also consistent with the results of TEM and nitrogen sorption.

In order to learn the correlation between metal nanoparticles and the reactivity/selectivity of CO hydrogenation, XPS (X-ray Photoelectron Spectroscopy) was employed to determine the oxidation states of Rh and Mn before and after hydrogen reduction, which are shown in Table x and Figure x. According to the XPS analysis, we realized the greater binding energy of the component, the higher oxidation state. It can be found that the binding energy of the $Rh3d_{5/2}$ of Rh-Mn/MCN before hydrogen reduction is 307.0 eV, less than the one after reduction (308.3 eV), which is consistent with the reported value of Rh^0 .²⁴ This indicates that pretreatment is sufficient and necessary to reduce easily-oxidized Rh complex into Rh^0 and Rh mainly existed in the metallic state (Rh^0) on the carbon surface during CO hydrogenation. In other words, Rh^0 is active for the formation of C_{2+} oxygenates. However, Rh^+ might exist during the reaction owing to an unstable intermediate derived from Rh^0 after oxidation by oxygen atom dissociated from CO molecules. The role of Rh^+ playing in CO hydrogenation has been well studied^{25,26} and it is well known as well that chemisorbed-CO on Rh^0 at room

temperature would reduce isolated Rh^+ to Rh^0 after CO desorption. Therefore, there should be only negligible amounts of Rh^+ on the supported catalyst.

For the oxidation state of Mn in Rh-Mn/MCN, it was determined that the binding energies of Mn species were close (641.0 eV and 641.8 eV), indicating that Mn existed in the state of Mn^{2+} or higher valence states (Mn^{3+} and Mn^{4+}) before and after reduction.²⁴ Mn^{2+} was unlikely to be reduced to its metallic state and could influence the selectivity effectively with its high valence states as a promotor during CO hydrogenation.

Conclusion

In conclusion, ordered mesoporous carbon nanoparticles (MCN) have been successfully demonstrated as a catalytic support for CO hydrogenation and exhibited interesting effect on catalytic performance. Owing to the unique mesoporosity, catalytic metal particles were highly distributed over MCN and Rh-Mn/MCN might be able to suppress methane production at higher temperature. In order to study the impact of mesostructures, the reactivity and selectivity of CO hydrogenation on Rh-supported mesoporous carbon materials with different porous structures such as CMK-3, CMK-5 and CMK-8 are currently under investigation.

Experimental

Preparations of Materials

Preparation of aluminosilicate MCM-48: For synthesis of OMC, the silica was converted to an aluminosilicate form using a solution of AlCl_3 following the post-synthesis procedure: as-synthesized MCM-48 material was calcined at 550 °C to remove the surfactant. The

calcined sample was mixed with distill water to make surface silanol groups, and then completely dried at 150 °C. The dried sample was slurried in ethanol solution of the anhydrous AlCl_3 (Si/Al = 20). The ethanol solvent was completely evaporated by rotary evaporator. The dried sample was calcined again at 550 °C.

Preparation of MCN: Ordered mesoporous carbon nanoparticles MCNs were prepared using furfuryl alcohol (Aldrich) as a carbon source. 1g of aluminated MCM-48 nanoparticles were infiltrated with 0.91 mL of furfuryl alcohol by impregnation method. The mixture was moved into Schlenk reactor, and subjected to freeze-vacuum-thaw three times using liquid N_2 . The mixture was kept under vacuum at 35 °C for 1 h. After opened schlenk reactor, the mixture was heated for 6 h at 100 °C for polymerization of furfuryl alcohol, and then partially carbonized at 350 °C for 3 h under vacuum. After cooled to room temperature, the sample was added with 0.58 mL of furfuryl alcohol, and repeated freeze-vacuum-thaw and polymerization again. Further carbonization was accomplished by heating to 900 °C under vacuum condition. The carbon product was collected by HF washing. (10 wt% HF in EtOH/ H_2O solution)¹⁵

Preparation of COOH-MCN: 300mg of MCNs were placed in a 100mL round-bottom flask with 30mL nitric acid (1M) and the solution was refluxed at 110°C for 1.5 h, then followed by hot filtration and washed with copious of water till the pH value of aqueous filtrate reached 7. The as-synthesized carbon material was dried under vacuum at 100°C for 8h before further usage.

Preparation of COONa-MCN: 150mg of COOH-MCNs were mixed with sodium carbonate aqueous solution (80mg Na_2CO_3 /20mL H_2O) and the solution was stirred at 30°C

for 6h, followed by filtration and washed with considerable amount of water. Likewise, the as-synthesized carbon material was dried under vacuum at 100°C for 8h before further usage.

Preparation of Rh-Mn/MCN: 148.3mg of COONa-MCNs were placed in 50mL double-neck round-bottom flask and mixed with 2.8mg of $\text{Rh}_2\text{Cl}_2\text{CO}_4$ (2 wt % of Rh loading over Rh-Mn/MCN) in 5mL toluene under nitrogen. The solution was stirred at 60°C for 3h. After three hour reaction, the prepared 9.6mg $\text{Mn}(\text{NO}_3)_2/5\text{mL}$ ethanol solution (2 wt % Mn loading over Rh-Mn/MCN) was added in the flask with three further hour reaction at 60°C. The metal complex MCNs were filtered, washed with hexane and dried under vacuum overnight. In order to obtain Rh-Mn/MCNs, the metal complex MCNs were reduced under hydrogen with a gas flow rate (1.67mL/s) at 300°C for 3h with heating ramp (2°C/min). The as-synthesized Rh-Mn/MCN was washed with water to remove NaCl then dried under vacuum at 100°C for 8h before the catalytic reaction.¹⁹

Preparation of Catalytic Reaction

Rh-Mn/MCN (0.3g) was placed in a micro-tubular reactor to examine CO hydrogenation under the pressure of 450 psi at 300°C for 21 h with syngas of $\text{H}_2/\text{CO}=2/1$ and a total flow 33 mL/min. (GHSV = 6600 h^{-1}) Prior to reaction, the catalyst was reduced at 300°C in a flow of H_2 (10 mL/min) under 450psi for 2 h. The effluent flew through a condenser filled with 10 mL nano-pure water. The tail gas was analyzed on-line by Varian GC (CP 3900) equipped with a packed column and a TCD detector. The dissolved oxygenate products were analyzed off-line by the GC (CP 3900) equipped with a CP-PoraBOND Q Fuse Silica capillary column and a FID detector.

General Characterization

XRD patterns were recorded on a Scintag XDS-2000 instrument operated at 1.21 kW, using Cu K α radiation. The nitrogen adsorption isotherms were measured at liquid nitrogen temperature (77 K) using a Micromeritics ASAP2000 volumetric adsorption analyzer. The Brunauer-Emmett-Teller (BET) equation was used to calculate the apparent surface area from adsorption data obtained at P/P₀ between 0.05 and 0.2. The total volume of micro- and mesopores was calculated from the amount of nitrogen adsorbed at P/P₀ = 0.95, assuming that adsorption on the external surface was negligible compared to adsorption in pores. The pore size distributions (PSD) were calculated by analyzing the adsorption branch of the N₂ sorption isotherm using the Barret-Joyner-Halenda (BJH) method. SEM (scanning electron microscopy) images were obtained with a JEOL 840A scanning electron microscope operating at 10 kV. The samples were coated with gold before SEM measurement. TEM (transmission electron microscopy) images were taken from particles supported on a porous carbon grid, using a Tecnai G2 F20 equipment operated at 200 kV. The catalytic performance was carried out in a micro-tubular reactor and the tail gas was analyzed on-line by Varian GC (CP 3900) equipped with a packed column and a TCD detector. The dissolved oxygenate products were analyzed off-line by the GC (CP 3900) equipped with a CP-PoraBOND Q Fuse Silica capillary column and a FID detector with hydrogen as carrier gas, and 1-butanol as internal standard. XPS (X-ray photoelectron spectroscopy) measurements of the samples were completed on a PHI 5500 Physical Electronic Multitechnique system. The testing conditions were as follows: radiation source, Al standard X-ray source (Al K α radiation, $h\nu = 1486.6$ eV), PE=58.7 eV; detection area = 1.5 mm², pressure in the analysis

chamber= 10^{-9} Torr. Binding energies (BEs) were determined with an accuracy of ± 0.1 eV.

The charging effects were measured against adventitious carbon of C1s (284.8 eV).

Scheme 1. Synthesis of Rh-Mn/MCN

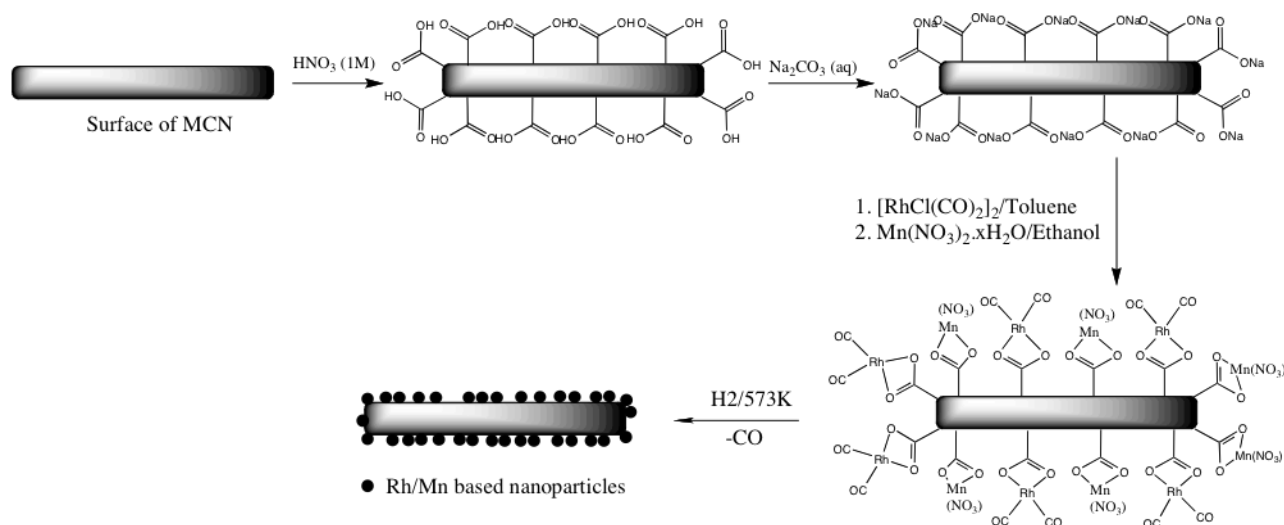


Table 1. The catalytic performance and the selectivity of products

Task	Temperature (°C)	GHSV ($\text{g}^{-1} \cdot \text{h}^{-1}$)	CO Conversion (%)	Selectivity (C %)					STY of C_{2+} oxygenates (g/kg-hr)
				CH_4	C_{2+} HC	CO_2	MeOH	C_{2+} oxygenates	
1	300	9,300	N/A	N/A	N/A	N/A	N/A	N/A	43.01
2	300	18,600	18.00	41.00	7.00	26.00	11.76	14.24	25.91
3	300	37,200	5.00	0	9.00	14.00	42.80	34.20	18.78
4	325	18,600	17.00	34.00	8.00	20.00	20.80	17.20	35.96
5	300	6,607	3.27	36.97	0	20.31	19.69	28.04	27.16

N/A: Accurate gas composition is not able to be obtained due to the low flow rate.

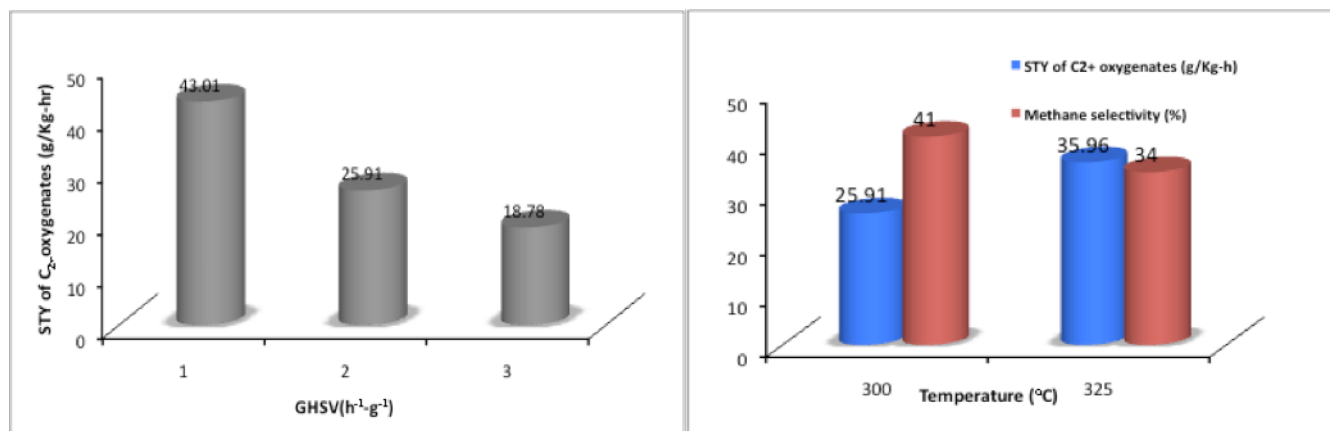


Figure 1. (a) The correlation between GHSV and STY of C₂⁺ oxygenates; (b) The comparison of methane selectivity and STY of C₂⁺ oxygenates

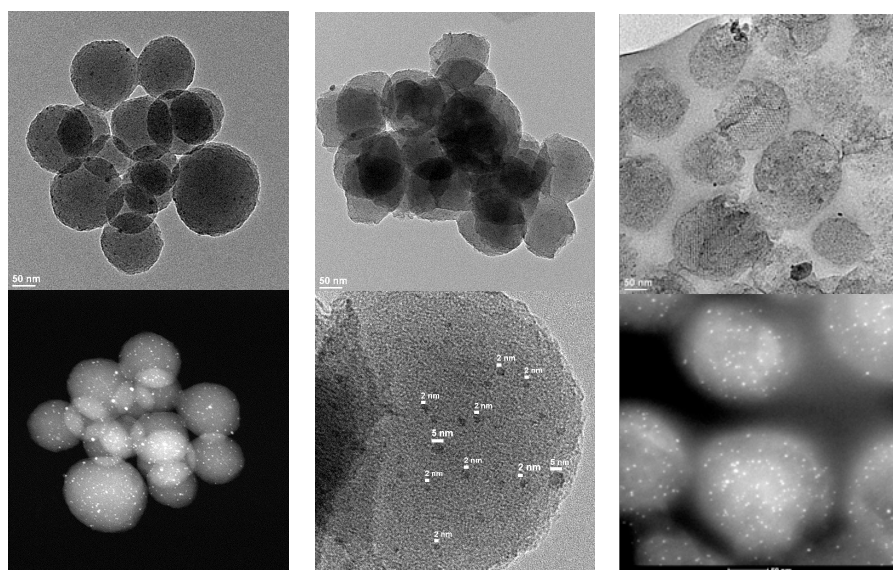


Figure 2. TEM and STEM micrographs of Rh-Mn/MCN (a); Rh-Mn/MCN(rxn) (b); ultramicrotomed Rh-Mn/MCN (rxn) (c)

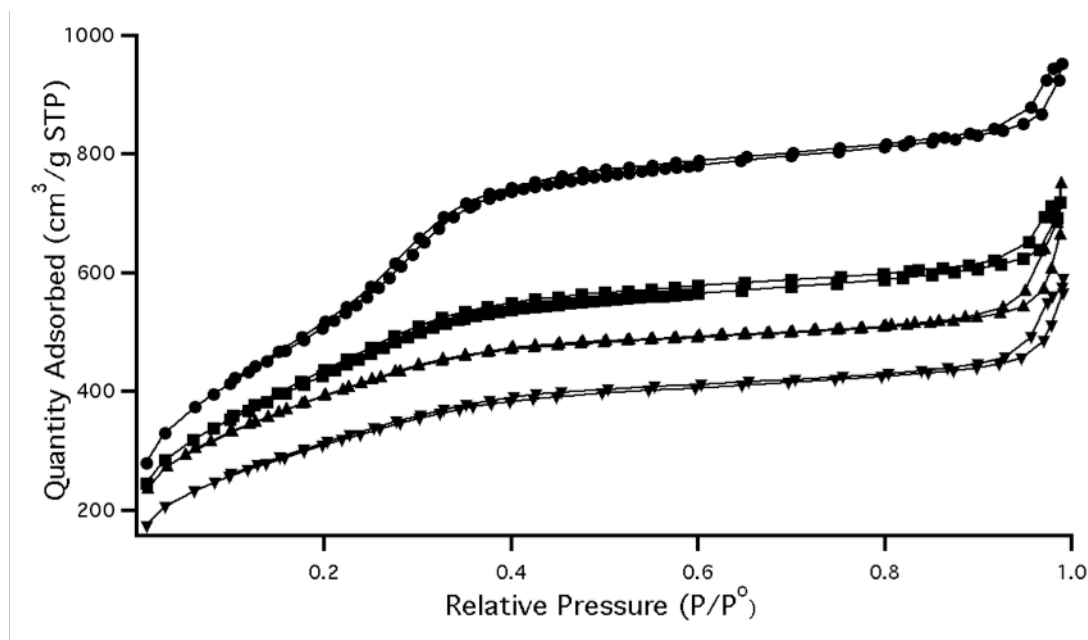


Figure 3. BET isotherms of surface functionalized MCN, -●- MCN; -■- COOH-MCN; -▲- Rh-Mn/MCN; -▼- Rh-Mn/MCN (rxn)

Table 2. Structural properties of surface-functionalized MCN^a

Samples	S_{BET} (m^2g^{-1})	W_{BJH} (nm)	V_p (cm^3g^{-1})
MCN	1874.3	2.9	1.32
COOH-MCN	1567.2	2.3	0.97
Rh-Mn/MCN	1419.6	<1.8	0.84
Rh-Mn/MCN (after reaction)	1131.7	<1.8	0.71

^a: S_{BET} stand for surface area; W_{BJH} stand for pore diameter; V_p stand for total pore volume

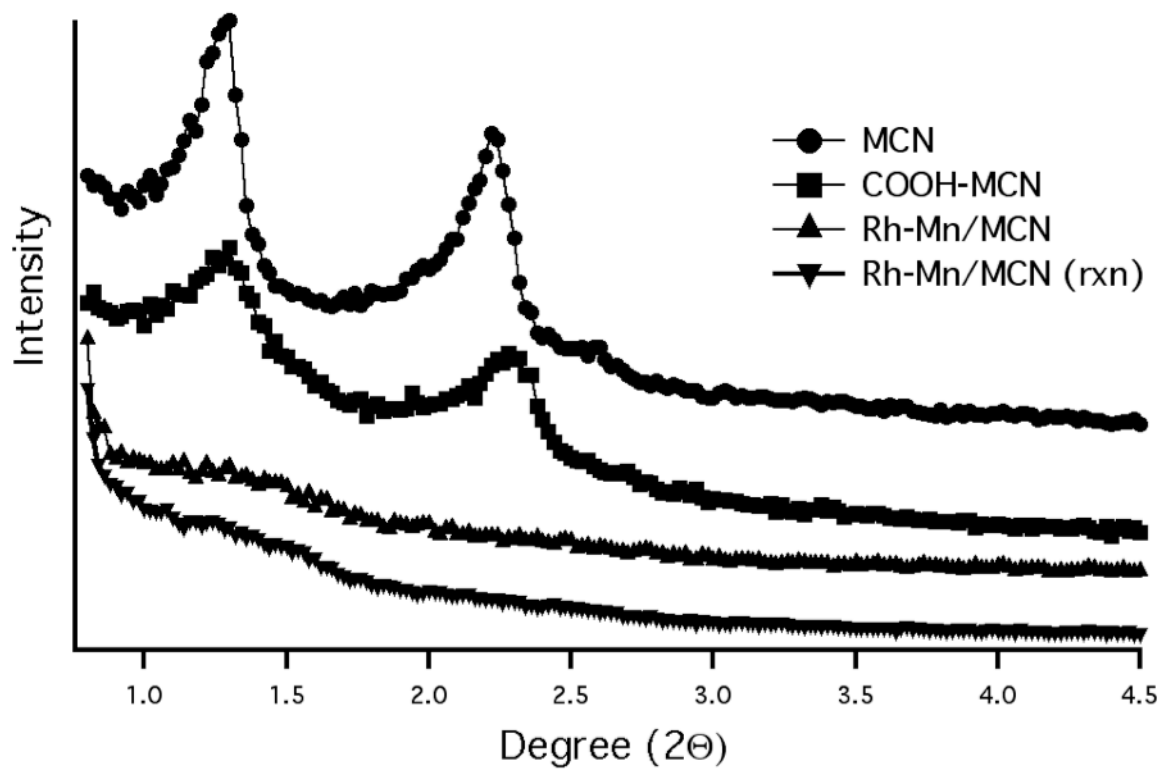


Figure 4. Powder X-ray patterns of surface-functionalized MCN and Rh-Mn/MCN after reaction)

Table 3. Binding energies of Rh-Mn/MCN before and after reduction

Sample	Testing conditions	Binding energies (eV)	
		Mn2p _{3/2}	Rh3d _{5/2}
Rh-Mn/MCN ^a	Before reduction	641.0	308.3
	After reduction	641.8	307.0

a: In order to obtain higher resolution of XPS, the sample was prepared with higher metal loading (4 wt % Rh-4 wt% Mn/MCN)

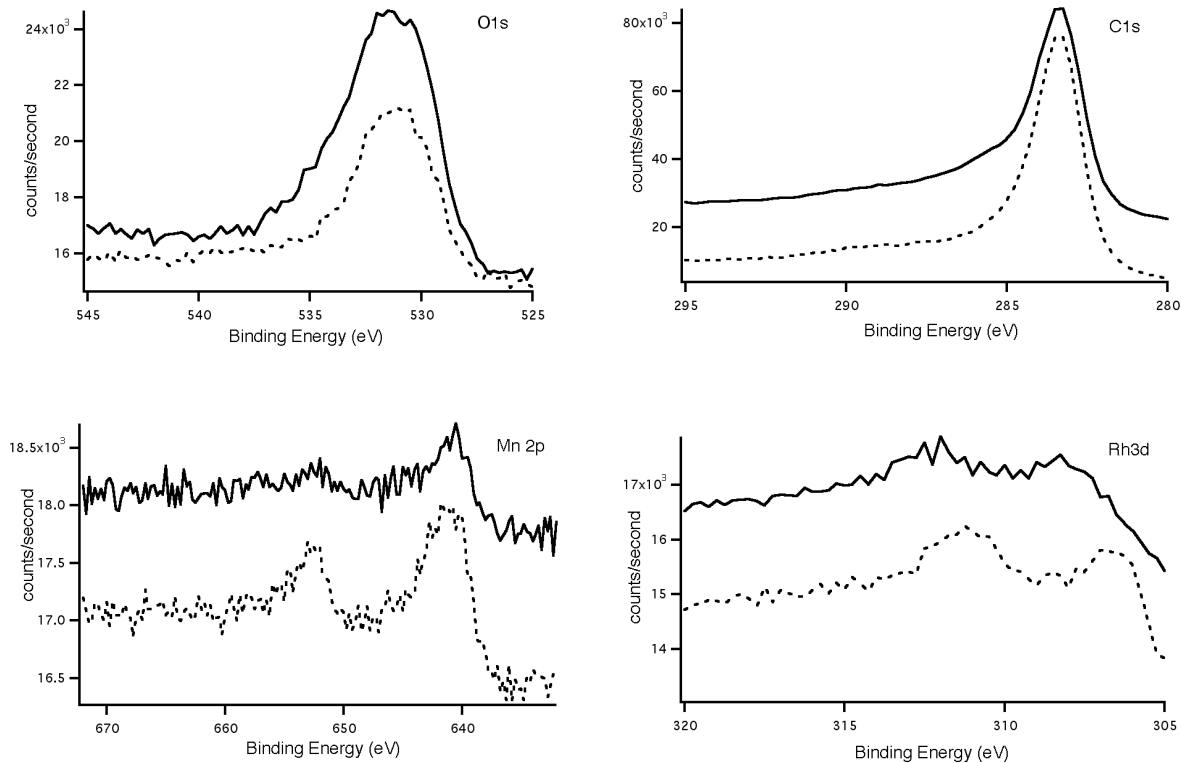


Figure 5. Binding energies of various components on Rh-Mn/MCN (Solid line represents Rh-Mn/MCN before hydrogen reduction; dashed line represents Rh-Mn/MCN after hydrogen reduction)

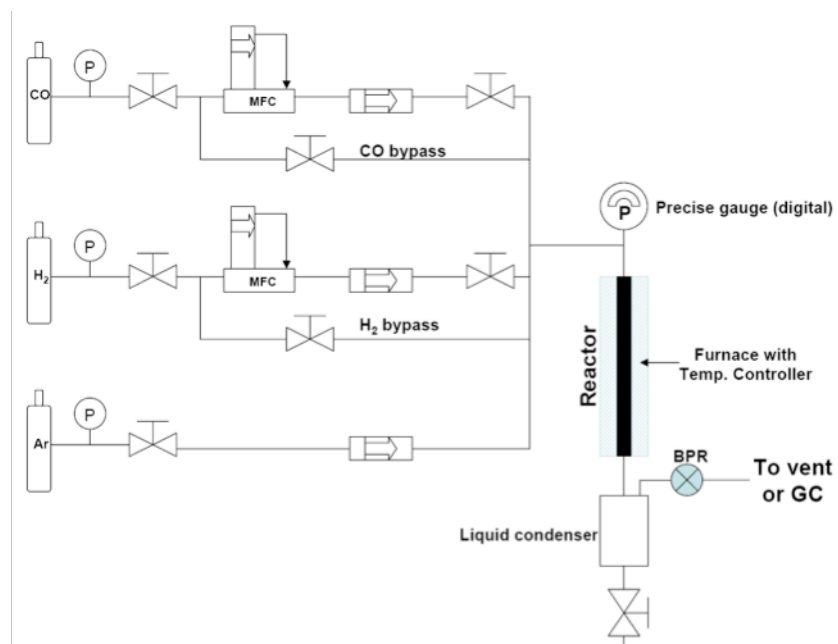


Figure 6. Flow diagram of a micro-tubular reactor

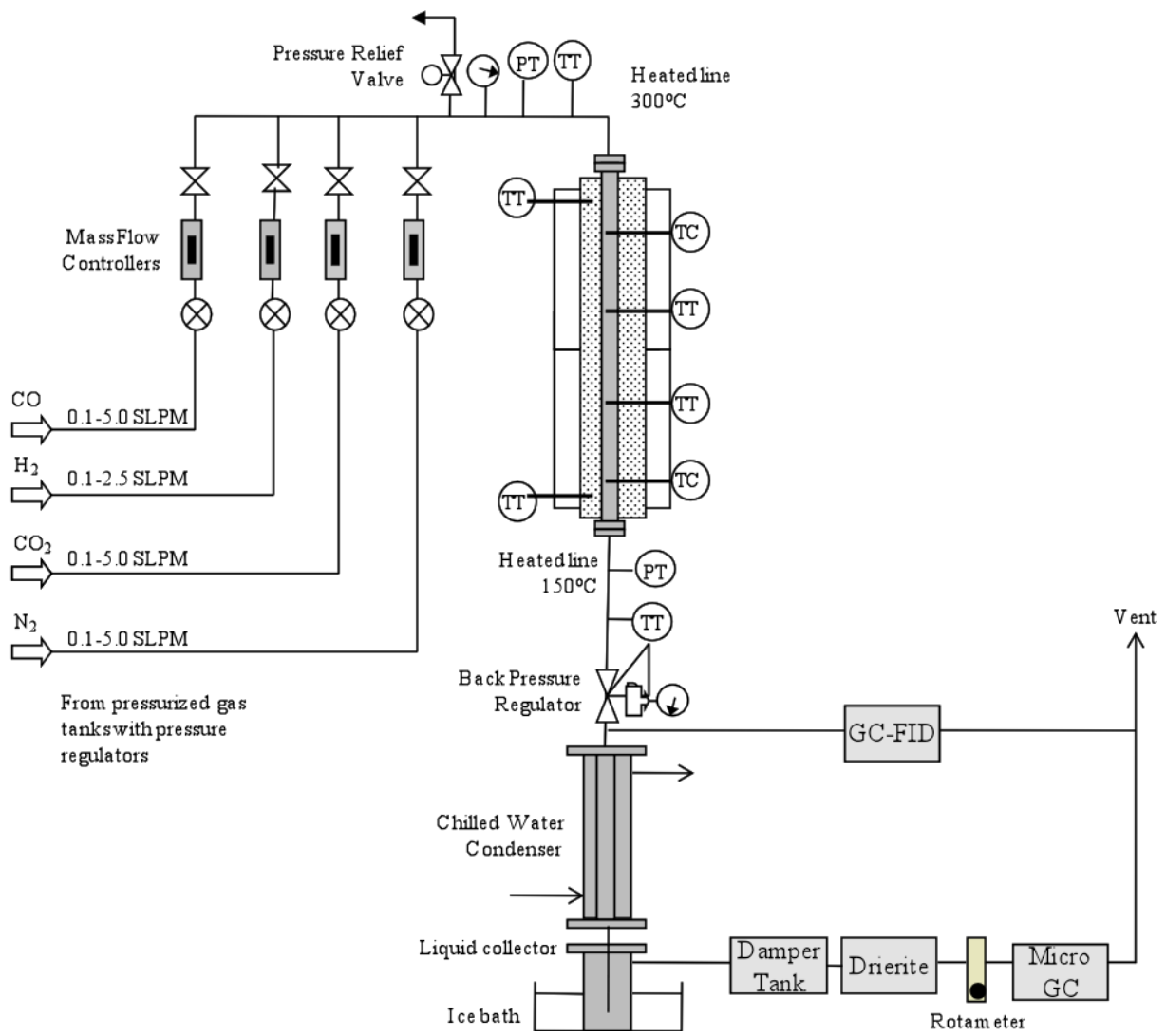


Figure 7. Schematic Diagram of the Fixed-Bed Reactor Setup

References

- (1) George, H.; Avelino, C. *Angew. Chem. Int. Ed.* **2007**, *46*, 7184.
- (2) Spivey, J. J.; Egbebi, A. *Chem. Soc. Rev.* **2007**, *36*, 1514.
- (3) Subramani, V.; Gangwal, S. K. *Energy & Fuels* **2008**, *22*, 814.
- (4) Ichikawa, M.; Fukushima, T. *J. Chem. Soc., Chem. Commun.* **1985**, 321.
- (5) Reuel, R. C.; Bartholomew, C. H. *J. Catal.* **1984**, *85*, 78.
- (6) Vannice, M. A. *J. Catal.* **1975**, *37*, 449.
- (7) Murchison, C. B.; Murdick, D. A. *Hydrocarb. Process.* **1981**, *60*, 159.
- (8) Tago, T.; Hanaoka, T.; Dhupatemiya, P.; Hayashi, H.; Kishida, M.; Wakabayashi, K. *Catal. Lett.* **2000**, *64*, 27.
- (9) Zhou, S. T.; Zhao, H.; Ma, D.; Miao, S. J.; Cheng, M. J.; Bao, X. H. *Z. Phys. Chemie-Int. J. Res. Phys. Chem. Chem. Phys.* **2005**, *219*, 949.
- (10) Gao, J.; Mo, X.; Chien, A. C.-Y.; Torres, W.; Goodwin Jr, J. G. *J. Catal.* **2009**, *262*, 119.
- (11) Chuang, S. S. C.; Stevens, R. W.; Khatri, R. *Top. Catal.* **2005**, *32*, 225.
- (12) Arakawa, H.; Takeuchi, K.; Matsuzaki, T.; Sugi, Y. *Chem. Lett.* **1984**, 1607.
- (13) Phillips, J.; Weigle, J.; Herskowitz, M.; Kogan, S. *Applied Catalysis A: General* **1998**, *173*, 273.
- (14) Pan, X.; Fan, Z.; Chen, W.; Ding, Y.; Luo, H.; Bao, X. *Nature Materials* **2007**, *6*, 507.
- (15) Kim, T.-W.; Chung, P.-W.; Slowing, I. I.; Tsunoda, M.; Yeung, E. S.; Lin, V. S. Y. *Nano Lett.* **2008**, *8*, 3724.
- (16) Rodriguez, N. M. *J. Mater. Res.* **1993**, *8*, 3233.
- (17) Banerjee, S.; Wong, S. S. *Nano Lett.* **2002**, *2*, 49.
- (18) Bazula, P. A.; Lu, A.-H.; Nitz, J.-J.; Schiøth, F. *Microporous Mesoporous Mater.* **2008**, *108*, 266.
- (19) Giordano, R.; Serp, P.; Kalck, P.; Kihn, Y.; Schreiber, J.; Marhic, C.; Duvail, J.-L. *Eur. J. Inorg. Chem.* **2003**, *2003*, 610.
- (20) Okabe, K.; Murata, K.; Mohammad, N.; Liu, Y.; Takahara, I.; Inaba, M. *Journal of the Japan Petroleum Institute* **2007**, *50*, 349.
- (21) Chen, W. M.; Ding, Y. J.; Jiang, D. H.; Pan, Z. D.; Luo, H. Y. *Catal. Lett.* **2005**, *104*, 177.
- (22) Hamada, H.; Funaki, R.; Kuwahara, Y.; Kintaichi, Y.; Wakabayashi, K.; Ito, T. *Applied Catalysis* **1987**, *30*, 177.
- (23) Bore, M. T.; Pham, H. N.; Ward, T. L.; Datye, A. K. *Chem. Commun.* **2004**, 2620.
- (24) Wang, Y.; Luo, H.; Liang, D.; Bao, X. *J. Catal.* **2000**, *196*, 46.
- (25) Watson, P. R.; Somorjai, G. A. *J. Catal.* **1981**, *72*, 347.
- (26) Watson, P. R.; Somorjai, G. A. *J. Catal.* **1982**, *74*, 282.

CHAPTER 5. FACILE SYNTHESIS OF MONODISPERSED SPHERICAL MCM-48 MESOPOROUS SILICA NANOPARTICLES WITH CONTROLLED PARTICLE SIZE

A paper to be submitted to *Chemistry of Materials*

*Tae-Wan Kim, Po-Wen Chung, and Victor S.-Y. Lin**

Abstract

A rapid and facile synthesis route to the monodispersed spherical MCM-48 mesoporous silica nanoparticles (MSN) with cubic $Ia-3d$ mesostructure is developed based on the modified Stöber method. The phase domain of MCM-48-type MSNs can be extended by controlling the stirring rate, and amount of silica source and the concentration of surfactant, correspondingly. The formation of monodispersed spherical MCM-48-type MSNs is obtained using triblock copolymer Pluronic F127 as a particle size designer. The average size of monodisperse spherical MSN can be controlled from 70 to 500 nm depending on the amount of F127. Moreover, the pore diameter of MSNs can be precisely controllable in pore diameters from 2.3 to 3.3 nm using different alkyl chain surfactant and simple post-hydrothermal treatment. Investigation of MCM-48-type MSN materials by powder X-ray diffraction, transmission electron microscopy, scanning electron microscopy, and nitrogen physisorption clearly reveals that MSNs show high specific surface area, high pore volumes, controllable morphological aspects, and tunable pore diameter. The MCM-48-type MSNs

are also demonstrated as a good hard template for preparation of non-siliceous nanoparticles such as mesoporous metal oxides. The present discovery of the extended synthesis conditions and the binary surfactant system in the MCM-48 synthesis offers to reproducible and facile synthesis of the monodisperse spherical MCM-48 mesoporous silica nanoparticles with precise structural control, providing vast prospects for future applications of ultra-fine mesostructured nanoparticle materials.

1. Introduction

Since the discovery of the M41S families in early 1990s,^{1,2} the field of ordered mesoporous materials using organic-inorganic self assembly has been considerably studied on the mesostructural diversity, compositional flexibility, and control of the pore size and morphology.³⁻⁹ In these researches, the synthesis of monodisperse mesoporous nanoparticles with controllable particle size should be important due to many potential applications of chromatography, cosmetics, catalyst, and adsorption^{3,5,6,9-12} because mesoporous nanoparticles provide greater pore accessibility and smooth molecular diffusion. Specially, ultrafine mesoporous nanoparticles below submicron size (normally, below 500 nm) could be used biomedical and pharmaceutical applications such as drug, gene, protein, imaging agents delivery, and biosensors.^{8,12-17}

To date, there are great efforts in the development of recipes for preparation of monodisperse mesoporous nanoparticles. The factors for control morphology and particle size of mesoporous nanoparticles are complicatedly connected to surface energy and cooperative organization between the template organics and inorganic source components.¹⁸

Thus, monodispersed mesoporous nanoparticles with the particle size from hundreds

nanometer to a few micrometer have been prepared *via* sol-gel process using various synthetic approaches, which involves extremely diluted reaction solutions, quenching procedures, complexing strategy, spray drying, emulsion confinement, ionic liquids templating, dry-gel conversion and binary surfactant system.^{5,11,14,19-37} Among these mesoporous silica nanoparticles (MSNs), monodisperse spherical MCM-41-type MSN materials with 2-dimensional (2-D) hexagonal $p6mm$ structure using cationic surfactant as a structural directing agent were demonstrated to act as a good intracellular carrier for biomedical and pharmaceutical applications.^{8,12-17}

Compared to 2-D hexagonal MCM-41 in M41S family, MCM-48 mesoporous silica with three-dimensional (3-D) cubic $Ia-3d$ mesostructure has interesting mesostructure, which consists of two interpenetrating continuous networks of chiral channels.^{1,2,38,39} These enantiomeric pair of porous channels are known as separated by an inorganic wall following exactly the gyroid (G -surface) infinite periodic minimal surface (IPMS).^{40,41} This unique 3-D network is able to provide a highly open porous host with high accessibility for guest species, thus facilitating inclusion or diffusion throughout the pore channels without pore blockage.³⁸ While their properties attract increasing attention for potential use as catalysts, adsorbent, and 'hard template' for the fabrication of nanomaterials,^{3,9,10,42-45} facile synthesis of monodisperse spherical MCM-48-type MSN materials with the cubic $Ia-3d$ mesophase still remains challenging. Conventionally, the synthesis of MCM-48 materials is carried out by hydrothermal routes, but the hydrothermal synthesis methods typically take a long time with high temperature in a narrow range of compositions.^{2,38,46} Moreover, large particle size above 1 μm with irregular morphologies would be observed. In contrast to the hydrothermal recipes, the modified Stöber method proposed by Schumacher *et. al.* needs short synthesis

time at room temperature.^{47,48} This recipe produces the spherical MCM-48 mesoporous silica nanoparticles below 1 μm , but those particles are not fully monodispersed and the particles size is too large to be employed in the intracellular bio-applications.

In the present work, we discovered that the monodisperse spherical MCM-48-type mesoporous silica nanoparticles could be synthesized under the conditions of low surfactant/silicon ratio with high stirring rate based on modified Stöber method. The phase domain for the cubic *Ia-3d* mesophase could be extended while the amounts of silica source and surfactant were changed correspondingly. Monodisperse spherical MCM-48 nanoparticles with controllable particle size were obtained by using Pluronic F127 as a dispersant agent, and the pore size can be tunable by using different alkyl chain length of surfactant and simple post-hydrothermal treatment. In addition, we demonstrated the synthesis of a series of mesoporous metal oxide nanoparticles by using the MCM-48-type MSNs as a hard template.

2. Experimental

2.1. Preparation of MCM-48

The preparation of MCM-48 ordered mesoporous silica nanoparticles was based on the modified Stöber method, previously reported.^{47,48} The MCM-48-type MSNs were synthesized under various synthetic conditions using a mixture of cetyltrimethylammonium bromide (CTAB, Aldrich) and ethanol as a structure-directing mixture. Tetraethyl orthosilicate (TEOS, Gelest Inc.) and triblock copolymer F127 (Pluronic F127, EO₁₀₆PO₇₀EO₁₀₆) are as a silica source and a particle dispersion agent, respectively.^{29,31} The molar composition of the reaction mixture was varied in the range of x TEOS: 0.4 CTAB:

$12.5 \times y$ NH₃: $54 \times y$ EtOH: $417 \times y$ H₂O: z F127 with $x = 1-4.25$, $y = 1-9$, and $z = 0-0.094$. The reaction temperature was fixed at room temperature, and further post-hydrothermal treatments were carried out at 403 K and 423 K.⁴⁹ A typical preparation of MCM-48-type MSN is as following: 0.5 g of CTAB and 2.05 g of F127 is dissolved in 96 mL of distilled water, 34 g of EtOH, and 10.05 g of 29 wt% ammonium hydroxide solution at room temperature. After complete dissolution, 1.8 g of TEOS is added into the mixture at once. After 1 min mechanical stirring with 1000 rpm, the mixture is under static condition for 24 h at RT for further silica condensation. The white solid product is recovered by ultra-high speed centrifuge (Sorvall Evolution Centrifuge), washing with water and dried at 343 K in air. The final template-free MCM-48 MSN materials are obtained after calcinations at 823 K in air. For the post-hydrothermal treatment, the centrifuged sample is placed in the Teflon lined autoclave with 8.5 ml of distilled water. The hydrothermal temperature is varied from 403 K to 423 K for 2 days under static condition.

For the pore size control using different alkyl chain length of surfactant, the same synthesis described above can be carried out using octadecyltrimethylammonium bromide (OTAB, Aldrich), instead of CTAB. The molar composition of the reaction mixture was varied in the range of 1.75 TEOS: 50 NH₃: 216 EtOH: 0.4 OTAB: 1668 H₂O: x F127 with $x = 0-0.047$.

2.2. Preparation of metal oxide nanoparticles

A series of mesoporous metal oxide nanoparticles, iron oxide (Fe₂O₃), cobalt oxide (Co₃O₄), cerium oxide (CeO₂), and indium oxide (In₂O₃), were prepared using MCM-48-type MSN with post-hydrothermal treatment at 423 K as a hard template. The metal oxides

synthesis was carried out with repeated impregnation-calcination process.^{50,51} For example, the detailed synthesis of mesoporous iron oxide nanoparticle is as followed: 0.15 g of calcined MCM-48 MSN is impregnated with 0.33 g of iron (III) nitrate nonahydrate ($\text{Fe}(\text{NO}_3)_2 \cdot 9\text{H}_2\text{O}$, Aldrich) in 0.33 mL of acetone. After drying at 333 K for 2 h, the impregnated sample is calcined at 623 K for 5 h. The sample was added with 0.28 g of $\text{Fe}(\text{NO}_3)_2 \cdot 9\text{H}_2\text{O}$ in 0.28 ml of acetone and heated again. The last impregnation was performed with 0.23 g of iron nitrate in 0.23 ml of acetone and heating up to 823 K for 5 h. The template MSN is removed by 1 M NaOH aqueous solution twice.

2.3. Characterization

Powder XRD patterns were recorded on a Scintag XDS-2000 instrument operated at 1.21 kW, using Cu K α radiation. The nitrogen adsorption isotherms were measured at liquid nitrogen temperature (77 K) using a Micromeritics ASAP2000 volumetric adsorption analyzer. The Brunauer-Emmett-Teller (BET) equation was used to calculate the apparent surface area from adsorption data obtained at P/P_0 between 0.05 and 0.2. The total volume of micro- and mesopores was calculated from the amount of nitrogen adsorbed at $P/P_0 = 0.95$, assuming that adsorption on the external surface was negligible compared to adsorption in pores. The pore size distributions (PSD) were calculated by analyzing the adsorption branch of the N_2 sorption isotherm using the Barret-Joyner-Halenda (BJH) method. Scanning electron micrograph (SEM) images were obtained with a JEOL 840A scanning electron microscope operating at 10 kV. The samples were coated with gold before SEM measurement. Transmission electron micrograph (TEM) images were taken from particles supported on a porous carbon grid, using a Tecnai G2 F20 equipment operated at 200 kV.

3. Results and discussion

3.1. Effect of CTAB concentration, stirring rate and time

Figure 1 shows powder XRD patterns of template-free mesoporous silica materials obtained by different amount of TEOS and CTAB, and stirring rate. It demonstrates the crucial role of the surfactant /silicon ratio and stirring rate on the formation of specific mesophase structure. The silica materials presented were synthesized using the digital magnetic stirrer (Corning Co.) for 4 h at room temperature with different stirring rate. From the powder XRD patterns in Figure 1 (a), it is clearly seen that the 3-D cubic *Ia-3d* mesophase is formed at the stirring rate between 450 to 850 rpm with the original modified Stöber method, (TEOS, diluted times) = (1.0, 1). Stirring rates in the range of 450–650 rpm lead to the formation of highly ordered cubic *Ia-3d* structures. In the case of 850 rpm, the *d*-spacings and peak shapes of XRD (211) and (220) reflections are decreased and broaden, which reflects the formation of low quality of cubic mesostructure. This quality control of MCM-48 synthesis at room temperature can be tuned by stirring rate, which is the similar results recently reported by Boote *et al.*⁵² The morphologies of these mesostructured MCM-48 silica materials with different stirring rates exhibited spherically but fused together. The particle size of each single spherical particle is varied between 150 to 600 nm. (Figure S1) In Figure 1 (b), the 4 times dilution of CTAB with lower silicon ratio, CTAB/TEOS = 0.16, affords 2-D hexagonal MCM-41-type mesoporous silica materials in low stirring rate below 650 rpm. However, the synthesis at the high stirring rate, 850 rpm, gives highly ordered 3-D cubic *Ia-3d* MCM-48 mesoporous silica. It prominently shows that such a structural transformation from 2-D hexagonal *p6mm* to 3-D cubic *Ia-3d* needs high stirring rate under

low surfactant/silicon ratio (CTAB/TEOS = 0.16) comparing to original modified Stöber method with high surfactant/silicon ratio (CTAB/TEOS = 0.4).^{47,48,52}

The phase formation of 2-D hexagonal mesophase under diluted condition of surfactant with the low stirring rate can be explained as follows: First, at an addition of more and more solvents of EtOH and H₂O, it will lead a diluting effect on the micelles making them less packed and small size, which naturally favors high surface curvature.⁵³ In addition, large amount of EtOH will be mostly act as a co-solvent in the mixture solution. It will make the hydrolysis of TEOS be slow down, and preferentially TEOS is solvated into EtOH. The suppression of TEOS hydrolysis decreased the amount of charged silicate moieties in the reaction solution, and subsequently increases repulsive force between adjacent head groups of the surfactant. Therefore, the effective headgroup area (a_0) becomes larger and it should be changed the surfactant packing parameter, g ($g = V/(a_0l)$ V : the total volume of the surfactant chain plus any cosolvent molecules between the chains, a_0 : the effective headgroup area at the organic-inorganic interface, and l : the surfactant chain length)^{7,54}, to decrease and favorably form 2-D hexagonal mesophase instead of 3-D cubic $Ia-3d$ mesophase.⁵⁵ However, at the high stirring rate under diluted surfactant conditions, TEOS hydrolysis can be more facilitated, and eventually it could lead to offset the factors for the formation 2-D hexagonal mesophase from cubic $Ia-3d$ mesophase described above. The synthetic recipe is currently the only available route to 3-D cubic $Ia-3d$ mesoporous silica allowing the use of kinetically controlled phase transformation by stirring rate in the modified Stöber method.

The mesostructure of 3-D cubic $Ia-3d$ symmetry can be readily obtained in a wide range of synthetic compositions by varying the combination of diluted condition for surfactant and amount of silica source at the high stirring rate. As shown in Figure 2, we can

make a map for the 3-D cubic *Ia-3d* phase region by changing these two synthetic variables, simultaneously. For this phase diagram, all syntheses were performed at room temperature with 850 rpm stirring rate for 4 h. As it can be seen, the region of obtaining a well-developed cubic *Ia-3d* phase is located between a region of 2-D hexagonal mesophase and a region of mixed phases. The poorly ordered mixed mesophase exhibiting several broad XRD diffraction peaks has been characterized mixed cubic-hexagonal phase.⁵⁶ (see Figure S2) The phase region for the cubic *Ia-3d* structure is reproducible and it indicates an approximately linear relationship between the amounts of TEOS and dilution times for CTAB surfactant. The synthesis interval ratios for the formation of the cubic *Ia-3d* phase are CTAB/TEOS = 0.4/1.0–6.1 in molar ratio with 1–9 times diluted surfactant conditions. For the formation of cubic *Ia-3d* mesophase under diluted CTAB concentration with high stirring rate, the relationship between dilution times and TEOS amount is dilution times/TEOS molar ratio = 1.4–1.6. It indicates the more diluted condition with high stirring rate needs the more amount of silica source for the formation of cubic *Ia-3d* mesostructure.

As shown in Figure 3, powder XRD patterns were measured on cubic *Ia-3d* MCM-48 materials synthesized according to the initial compositions taken in the cubic phase domain, with concurrent increase of the TEOS contents and dilution times for CTAB. All XRD diffraction patterns are all indexed to be cubic *Ia-3d* mesophase. However, it shows the differences in the shape and position of XRD peaks and its relative intensities with changing TEOS amount and dilution times for CTAB. These differences in the XRD diffraction patterns indicate the variation of structural properties and sample quality. The shape and relative intensity of XRD peak were gradually sharper and increased up to 4 times dilution condition, and then broaden and decreased, again. The nitrogen physisorption analyses

provide more detailed structural properties. The resultant sorption isotherms, depicted in Figure S3, are all type IV isotherms with a pronounced capillary condensation step around relative pressure $P/P_0 = 0.2\sim 0.3$. The sharpness of capillary condensation step is shown in the case of 1–4 times diluted condition for CTAB surfactant, but higher diluted CTAB leads less sharp capillary condensation which indicates poor development of mesostructure and low-quality mesoporous materials. The silica wall thickness is increased with the decrease of surfactant/TEOS molar ratio up to 4 times diluted condition. (Table S1) The low surfactant/silicon ratio gives rise to several advantages to synthesize the mesoporous silica materials comparing to high surfactant/silicon ratio: the improvement of the stability of whole mesostructure, the increase of framework thickness, and the requirement of small amount of surfactant.^{57,58} In the present synthetic recipe, the thicker wall of 4 times diluted condition with low surfactant/silicon ratio could provide stronger mesostructure and prevent the mesophase from structural collapse during the calcination with high temperature.

Low magnified SEM images (Figure S4 (a)–(e)) show the whole morphological aspect of each sample with different surfactant diluted condition. At the 4 times dilution (Figure S4 (c) and (f)), the whole feature of SEM image is still aggregated each single particles, but it forms smaller segments than the ones with the ones with 1 and 2 times diluted conditions (Figure S4 (a) and (b)). The more diluted CTAB concentration leads to the less aggregation of each particle. It indicates lower surfactant concentration leads to less aggregation of particles. In addition, the individual particle size is around 300–600 nm (mostly ca. 500 nm), which is more uniform than the one with high concentration of CTAB (150–600 nm, Figure S1). In Figure S4 (d)–(e) and (g) for more highly diluted CTAB conditions with lower surfactant/silicon ratio, the spherical particle size is similar to 4 times

dilution, but an amorphous silica phase appeared on the outside surface of particle. It is seemingly wrapped with other spherical particles and caused a high degree of aggregation. For the formation of cubic *Ia-3d* mesophase, the more diluted CTAB condition with high stirring rate needs the more amount of silica source per CTAB molar ratio. However, the amount of TEOS exceeds the amount of corresponding CTAB at highly diluted condition of CTAB (above 6 times dilution). The excess amount of TEOS makes the amorphous silica and low-quality mesoporous materials. The SEM results for highly diluted conditions are consistent with the powder XRD, as well as the nitrogen physisorption results. Above all, well-developed 3-D cubic *Ia-3d* mesoporous silica nanoparticles with less aggregation are able to be obtained when the syntheses are performed at 4 times diluted CTAB concentration with 2.5 TEOS molar ratio. This synthesis condition was employed to synthesis the materials described in as followings.

The stirring and aging time was varied between 30 sec–10 min and 0 min–24 h, respectively for a selected initial synthesis composition (4 times diluted condition: 2.5 TEOS: 50 NH₃:216 EtOH: 0.4 CTAB: 1668 H₂O) to explore the optimum synthesis condition for high quality of mesostructure and particle morphology. All samples were stirred at 1000 rpm by using digital mechanical stirrer (IKA Co.). The powder XRD patterns of the materials after filtration, washing, drying, and calcination at 823 K are reported in Figure 4. All silica samples synthesized with various stirring time and aging time exhibit diffraction patterns of the cubic *Ia-3d* mesostructure. The results show that MCM-48 mesostructure is built within very short time (~ 30 sec) under diluted CTAB condition with high stirring rate at 1000 rpm. The differences for XRD intensity and *d*-spacing revealed the stability and quality of sample. The *d*-spacing of all samples increased with longer time and the noticed increase also

occurred from 30 sec and 1 min in the case of stirring time experiment. (Figure 4 (a)) After addition of TEOS, facilitation of hydrolysis and condensation of silica source by longer stirring gives more stable and better quality of cubic mesostructure in the initial synthetic mixture. Nevertheless, particles aggregation would take place with longer stirring time at the high stirring rate. In Figure 4 (b), the longer aging time leads to increase d -spacing of samples after stopping of mechanical stirring at 1 min. The XRD patterns of as-synthesized samples have almost the same d -spacing (data are not shown), but the d -spacing was decreased more in the case of shorten aging time after calcination. It indicates longer agitation time was needed for further silica condensation, and it could avoid the shrinkage of the mesostructure during the calcination. The SEM images of short stirring and agitation time are mostly similar to the sample synthesized with 850 rpm for 4 h (Figure S4 (f)). Most particles are fused together even if changing the experimental facts: stirring and aging time. It shows that the particle morphology of MCM-48 at room temperature synthesis is determined at the initial synthesis time, and it did not depend on dilution of surfactant, stirring rate, and aging time so much.

3.2. Effect of F127 as a dispersion agent

For the synthesis of well size-defined and monodisperse MCM-48-type MSNs with controllable particle size below 500 nm, we studied on the binary surfactant system using different nonionic surfactants (OP-10 (poly(ethylene glycol) monoethylphenyl ether)),²⁶ PEG-4000 (polyethylene glycol),³⁷ and triblock copolymer Pluronic F127,^{29,31} and polymer (PVA (poly(vinyl) alcohol)³⁴ as particle grain-tailors. Except for Pluronic F127, the morphology of MCM-48 MSNs with the aforementioned inhibitors of grain growth still

indicated the aggregation of particles while using the 4 times diluted CTAB concentration (2.5 TEOS: 50 NH₃:216 EtOH: 0.4 CTAB: 1668 H₂O) with 1000 rpm for 1 min stirring. The addition of triblock copolymer Pluronic F127 as a nonionic surfactant decreased the size of the mesoporous silica particles produced by the assembly of the cationic surfactant and anionic silicate.^{29,31} The effect of the amount of F127 on the morphology and the size of the silica particles is investigated by TEM images. After the addition of certain amount of F127, the well-dispersed spherical particles were observed without aggregation shown in TEM micrographs in Figure 5 (b)-(d). The average particle size decreased from 500 to 70 nm with an increase of amount of F127. From the TEM images, the ranges of particle size are about 170–210 nm (most particle size: ca. 200 nm), 80–180 nm (ca. 130 nm), and 40–100 nm (ca. 70 nm) for [F127] = 0.047, 0.078, and 0.094, respectively. Powder XRD patterns and nitrogen physisorption isotherms for cubic *Ia-3d* MCM-48 MSNs with different amount of F127 molar ratio were shown in Figure 6. All powder XRD patterns shows the 3-D cubic *Ia-3d* mesophase, but the broadened XRD diffraction peaks were observed with an increase of F127 molar ratio above 0.047. This broadening of the diffraction peaks may be attributed to the decreasing mesophase domains owing to the decrease of particle size.³¹ The nitrogen isotherms illustrated the effect of the amount of F127 evidently. Each isotherm of MSN samples with different F127 amount exhibited two capillary condensation steps. The first step in a relative pressure range of 0.18–0.3 is attributed to the nitrogen condensation taking place at the internal mesopores, and the second step above 0.95 in adsorption branch is attributed to the interparticle voids, indirectly reflecting the size of particles. The higher step, the smaller particle is. The pore diameters templated by CTAB for all samples were almost similar around 2.2–2.3 nm (Table S2); however, the heights of both two capillary

condensation steps varied with an increasing amount of F127. With the lower amount of F127, the isotherm indicated the sharper step of the first capillary condensation but the smaller tailing in the second step. In contrast, the higher amount F127 gives rise to the lower amount of N₂ adsorption in the first step but the larger tailing in the second step. Based on these results, we are able to conclude that highly monodispersed and smaller particle size of MCM-48 type MSN materials can be synthesized with an increasing amount of F127. We can obtain the monodisperse MCM-48-type MSN without compromising structural properties by using triblock copolymer F127 as a good dispersant agent and grain size tailor in the binary surfactant system. It indicates that the present synthesis method, diluted CTAB concentration with high stirring rate could go through the route for cooperative assembly of silicate with the binary surfactant system.^{29,31} The cationic surfactant, CTAB, is assembled with anionic silicates through electrostatic interaction in a basic solution, producing a ordered mesophase. The nonionic surfactant, F127, interacting with silicates through the hydrogen bonds, limited the growth of the mesostructure particle grain. Therefore, the grain size of the resultant mesoporous silica can be determined by the inhibition caused by the interaction with F127.

For the reproducibility and scale-up test of the present synthesis recipe using diluted surfactant and low surfactant/silicon ratio with F127, the synthesis was carried out in a larger batch using, for instance, 4 g of CTAB in 1.2 L of F127-EtOH-NH₃-H₂O mixture solution. The powder XRD pattern and particle morphologies from TEM analysis of the large batch sample are similar to those of small batch one using 0.5 g of CTAB in 150 ml mixture solution. It indicates that the production of monodisperse spherical MCM-48 MSN materials

are able to be easily scaled up without any significant loss of sample quality due to kinetically controlled short synthesis time.

3.3. Pore size control

3.3.1. Synthesis of MCM-48 MSN using OTAB

For controlling the pore size of the MCM-48 MSNs, it is a well-known strategy to use different alkyl chain length cationic alkyltrimethylammonium surfactants *via* conventional hydrothermal synthesis route.⁵⁹ In addition to CTAB, a successful synthesis of MCM-48 MSNs using other cationic alkyltrimethylammonium surfactant *via* Stöber method has never been reported before.^{52,58} It should be noted that other different alkyl chain length surfactants were not suitable for the MCM-48 synthesis at room temperature under previous conditions of modified Stöber method. Figure 7 shows the XRD patterns of as-synthesized and calcined mesoporous silica materials using octadecyltrimethylammonium bromide (OTAB), which has longer alkyl chain length than CTAB. The samples were prepared with the present synthesis route as described previously: 4 times diluted surfactant concentration and mechanical stirring at 1000 rpm for 1 min, and then 1 d aging at room temperature. At the same surfactant/silicon molar ratio for the optimum synthesis condition using CTAB surfactant (surfactant/TEOS = 0.4/2.5), the mesophase from OTAB surfactant shows mix-phases of hexagonal and cubic. As decreasing the silica source from 2.5 to 1.75 in molar ratios, the mesophase is clearly transformed from mix-phase and highly ordered 3-D cubic *Ia-3d* mesophase. This is the first successful syntheses of MCM-48 templated by alkylammonium surfactants other than cetyltrimethylammonium at room temperature synthesis. The phase transformation is along the same trend as we discussed in phase

diagram for CTAB (Figure 2 and Figure S2), but the amount of silica source is decreased for synthesis of MCM-48 mesophase. The only difference from synthesis condition using CTAB is the chain length of the surfactant and it should also change the packing parameter, $g = V/(a_0l)$. The longer chain length of OTAB influences directly to decrease the value of g , which means mesophase was transformed to MCM-41 ($1/3 < g < 1/2$) from MCM-48 ($1/2 < g < 2/3$). However, the phase transformation goes through the different way from cubic $Ia-3d$ to mixed hexagonal and cubic phase at the OTAB/TEOS = 0.4/2.5 molar ratio. It means the mesophase formation using modified Stöber method under diluted surfactant condition with high stirring rate is different from conventional hydrothermal synthesis. The mesophase formation can be kinetically controlled by the degree of TEOS hydrolysis and silicate polymerization, which is one of the important factor for structural transformation by using high stirring rate, and then MCM-48 mesostructure is very quickly formed around 30 sec. (see Figure 1 (b) and (a)) The further study will be needed for phase transformation in the case of OTAB surfactant.

We also investigated the effect of F127 as a dispersion agent and particle size tailor in OTAB surfactant. MCM-48 mesoporous silica materials using OTAB were prepared as the molar ratio of 1.75 TEOS: 50 NH₃:216 EtOH: 0.4 OTAB: 1668 H₂O: 0~0.047 F127. As shown in Figure S5, all XRD patterns are highly ordered cubic $Ia-3d$ mesostructure. Interestingly, both the d -spacing and the pore size are increased after addition of F127. It supposes that a portion of F127 might be joined with OTAB surfactant during the assembly of the mesostructure because it might be more hydrophobic surfactant than CTAB. However, the reason for assembly F127 and OTAB is still unclear and we also need further investigation. The nitrogen isotherm of the sample without F127 also exhibited a distinct

capillary condensation step in the range of $P/P_0 > 0.95$ (Figure S5). The structural properties of the samples synthesized from OTAB surfactant are almost the same values, but pore size of the sample after addition of F127 is increased from 2.4 to 2.6 nm after addition of F127 (Table S3), like d -spacing from XRD patterns. Based on the TEM micrographs in Figure 8, the synthesis condition using OTAB template without F127 gives rise to higher degree of monodispersed MSNs than the synthesis condition using CTAB without F127. In the synthesis condition using OTAB, the relatively lower amount of silica source might reduce the possibility of fusing together among particles and then produced highly monodispersed MCM-48 MSNs. The particle size of MSN without F127 is about 200–230 nm with low degree of aggregation. With an increasing amount of F127, the number of aggregated particles decreased and finally monodispersed particles are shown above F127 = 0.031. In addition, the range of particle size gradually decreased as well from 200–230 nm to 160–200 nm with an increasing amount F127 from 0.016 to 0.047 in a molar ratio. It might be possible to obtain much smaller nanoparticles using more additional amount of F127, like the synthesis using CTAB surfactant.

3.3.2. Post-hydrothermal treatment

For the more precise tailoring of the textural parameters of the cubic $Ia-3d$ MCM-48 mesoporous silica nanoparticles, the post-hydrothermal treatments at 403 K and 423 K for 2 days were applied to a selected compositions (2.5 TEOS: 50 NH₃:216 EtOH: 0.4 CTAB: 1668 H₂O: 0.047 F127 and 1.75 TEOS: 50 NH₃:216 EtOH: 0.4 OTAB: 1668 H₂O: 0.031 F127). The XRD patterns of the calcined materials are reported in Figure 9. The MSNs synthesized after hydrothermal treatment all exhibited highly resolved diffraction patterns

characteristic of the cubic $Ia-3d$ mesostructure. A noticeable increase in the d -spacing and lattice parameters, occurs upon the increase of the temperature applied for the additional hydrothermal treatment compared to room temperature synthesis. Figure 10 shows the nitrogen sorption isotherms and pore size distributions for the same series of samples. The sorption isotherms for the different calcined samples remain type IV isotherms with a sharp capillary condensation step after hydrothermal treatment. The shift of the capillary condensation step to higher relative pressure with increasing temperature evidently demonstrated an increase in the mesopore size, as well as the pore size distribution curves. Structural and textural properties are summarized for these samples in Table 1. The pore volumes are shown to slightly increase, and the pore sizes range from 2.3 nm to 3.3 nm for the series of samples. The lattice parameter of the cubic mesophase increases from 8.07 nm at room temperature up to 10.3 nm for the mesoporous materials prepared at 423 K using CTAB surfactant. Moreover, the wall thickness is shown to increase with increasing post-hydrothermal temperature. It is noteworthy that a rearrangement of the silica framework has taken place at the high temperature during the hydrothermal treatment.⁴⁹ The morphology of MSNs still remains the separated spherical silica nanoparticles after post-hydrothermal treatment, but part of MSN particles shows low degree of aggregation. (Figure S6)

3.4. Mesoporous metal oxide nanoparticles

Various kinds of mesoporous metal oxide nanoparticles were successfully synthesized using MCM-48-type MSNs as a mold *via* a template synthesis route.⁶⁰ The synthesis of various mesoporous metal oxides was simply prepared by the repeated impregnation with desire metal precursors, and calcination process.^{50,51} As shown in Figure

S7, The XRD patterns of the mesoporous metal oxide nanoparticles, iron oxide (Fe_2O_3), cobalt oxide (Co_3O_4), cerium oxide (CeO_2), and indium oxide (In_2O_3), exhibited a single weak diffraction peak in the region of low angle, which can be indexed to (211) by the determination of the peak position. Each mesoporous metal oxide can be determined by the characteristic peaks of wide angle region. After removal of silica template, structurally-transformed mesoporous structures could be produced using MCM-48 templates, which is well-known phenomenon in the case of ordered mesoporous carbon CMK-1.^{39,42,60} This structure transformation can be determined from the appearing of the additional (110) diffraction peak below the 2 theta value of (211). However, we cannot distinguish any additional XRD peaks because of low intensity and low S/N ratio of XRD diffraction. It indicates these mesoporous metal oxide nanoparticles have small particle morphologies, or less ordering and structural deficiency, which are typically caused by the transformation from metal oxide precursors to metal oxides during the calcination.⁶¹ All metal oxides possess type IV isotherm shape with hysteresis loop and 4.8–6.3 nm of pore size. These larger pore diameters with broad pore size distribution comparing to ordered mesoporous carbon CMK-1 (ca. 2.3 nm in a diameter) might be attributed to large lattice contractions during the thermal treatment and less ordered mesostructures.⁶¹ As shown in Table S4, the BET areas and pore volumes of mesoporous metal oxide nanoparticles are 139–213 m^2/g and 0.15–0.32 cm^3/g , except In_2O_3 . The mesoporous Indium oxide nanoparticle has relatively small values of BET area (49 m^2/g) and pore volume (0.09 cm^3/g) than other metal oxides. As shown in Figure 11, the TEM images clearly show the morphology of mesoporous metal oxide nanoparticles as well as their mesostructural pore-ordering. The high magnified TEM images showed that all mesoporous metal oxide nanoparticles have well ordered mesopore arrangement. The

morphologies of all mesoporous metal oxides, except In_2O_3 , revealed mostly spherical nanoparticles, which is the same as a MCM-48 MSN template. It indicated the morphology of MSN can be well preserved in the mesoporous metal oxides during the replication process. But it also shows small irregular particles, which is attributed to incomplete filling of metal oxide precursors into the pores of MSN template. The rectangular particle shape and partially rectangular shape with highly ordered mesopore structures are shown in the case of In_2O_3 . From the low surface area and pore volume of mesoporous indium oxide nanoparticle in N_2 physisorption analysis, we could assume that this rectangular morphology is a growth of bulk indium oxide with a cubic crystalline morphology, which is located outside surface of MSN template and covered with the spherical mesoporous metal oxides. The high crystallinity of In_2O_3 in wide angle XRD pattern also provides the existence of the outside deposition of indium oxide. (Figure S7) It could be overcome to find an optimum amount of indium oxide precursor in the repeated impregnation-calcination process.

4. Conclusions

The preparation of monodisperse spherical MCM-48 mesoporous nanoparticles with 3-D cubic *Ia-3d* mesostructure, which is based on the modified Stöber method, is easy and highly reproducible. The synthesis is simply carried out by mechanical stirring of the basic surfactant template solution at 1000 rpm for 1 min at room temperature after addition of silica source. This method, kinetically controlled phase transformation by high stirring rate under low surfactant/silicon ratio, has become possible to synthesize the cubic *Ia-3d* mesophase in a wide range of mixture composition, and gives synthetic phase diagram in the

function of surfactant concentration and amount of silicon source. Most importantly, monodisperse spherical MCM-48 MSN with a precise control of the particle size was easily achieved by using triblock copolymer Pluronic F127 as a dispersant agent. In addition, the pore diameter of MCM-48 MSNs could be tunable using different alkyl chain surfactant and simple post-hydrothermal treatment. The MCM-48-type MSNs with tailored structural properties thus obtained can be used a versatile hard template for preparation of non-siliceous mesoporous nanoparticles such as metal, metal oxides, carbons, and polymers. Furthermore, 3-D enantiomeric pair of porous channel mesoporous structure with ultrafine nanoparticles is particularly suitable as materials for the applications of adsorption, delivery and release, and host-guests interactions.

References

- (1) Kresge, C. T.; Leonowicz, M. E.; Roth, W. J.; Vartuli, J. C.; Beck, J. S. *Nature* **1992**, *359*, 710.
- (2) Beck, J. S.; Vartuli, J. C.; Roth, W. J.; Leonowicz, M. E.; Kresge, C. T.; Schmitt, K. D.; Chu, C. T. W.; Olson, D. H.; Sheppard, E. W.; McCullen, S. B.; Higgins, J. B.; Schlenker, J. L. *J. Am. Chem. Soc.* **1992**, *114*, 10834.
- (3) Corma, A. *Chem. Rev.* **1997**, *97*, 2373.
- (4) Zhao, D.; Feng, J.; Huo, Q.; Melosh, N.; Fredrickson, G. H.; Chmelka, B. F.; Stucky, G. D. *Science* **1998**, *279*, 548.
- (5) Stein, A. *Adv. Mater.* **2003**, *15*, 763.
- (6) Hoffmann, F.; Cornelius, M.; Morell, J.; Fröba, M. *Angew. Chem. Int. Ed.* **2006**, *45*, 3216.
- (7) Wan, Y.; Zhao, D. Y. *Chem. Rev.* **2007**, *107*, 2821.
- (8) Trewyn, B. G.; Giri, S.; Slowing, I. I.; Lin, V. S. Y. *Chem. Commun.* **2007**, 3236.
- (9) L. F. Giraldo; B. L. López; L. Pérez; Urrego, S.; Sierra, L.; Mesa, M. *Macromol. Symp.* **2007**, *258*, 129.
- (10) Hartmann, M. *Chem. Mater.* **2005**, *17*, 4577.
- (11) Sun, J.; Zhang, H.; Tian, R.; Ma, D.; Bao, X.; Su, D. S.; Zou, H. *Chem. Commun.* **2006**, 1322.
- (12) Angelos, S.; Liang, M.; Choi, E.; Zink, J. I. *Chem Eng J* **2008**, *137*, 4.
- (13) Radu, D. R.; Lai, C. Y.; Jeftinija, K.; Rowe, E. W.; Jeftinija, S.; Lin, V. S. Y. *J. Am. Chem. Soc.* **2004**, *126*, 13216.
- (14) Trewyn, B. G.; Whitman, C. M.; Lin, V. S. Y. *Nano Lett.* **2004**, *4*, 2139.

- (15) Slowing, I.; Trewyn, B. G.; Lin, V. S.-Y. *J. Am. Chem. Soc.* **2006**, *128*, 14792.
- (16) Vallet-Regí, M.; Balas, F.; Arcos, D. *Angew. Chem. Int. Ed.* **2007**, *46*, 7548.
- (17) Torney, F.; Trewyn, B. G.; Lin, V. S. Y.; Wang, K. *Nat. Nanotechnol.* **2007**, *2*, 295.
- (18) Cho, E. B.; Kim, D.; Jaroniec, M. *J. Phys. Chem. C* **2008**, *112*, 4897.
- (19) Lu, Y.; Fan, H.; Stump, A.; Ward, T. L.; Rieker, T.; Brinker, C. J. *Nature* **1999**, 398, 223.
- (20) Grun, M.; Lauer, I.; Unger, K. K. *Adv. Mater.* **1997**, *9*, 254.
- (21) Cai, Q.; Luo, Z. S.; Pang, W. Q.; Fan, Y. W.; Chen, X. H.; Cui, F. Z. *Chem. Mater.* **2001**, *13*, 258.
- (22) Fowler, C. E.; Khushalani, D.; Lebeau, B.; Mann, S. *Adv. Mater.* **2001**, *13*, 649.
- (23) Sajanjikumari Sadasivan; Fowler, C. E.; Khushalani, D.; Mann, S. *Angew. Chem. Int. Ed.* **2002**, *41*, 2151.
- (24) Nooney, R. I.; Thirunavukkarasu, D.; Chen, Y.; Josephs, R.; Ostafin, A. E. *Chem. Mater.* **2002**, *14*, 4721.
- (25) Haskouri, J. E.; Zarate, D. O. d.; Guillem, C.; Latorre, J.; Caldes, M.; Beltran, A.; Beltran, D.; Descalzo, A. B.; Rodriguez-Lopez, G.; Martinez-Manez, R.; Marcos, M. D.; Amoros, P. *Chem. Commun.* **2002**, 330.
- (26) Zhao, W.; Li, Q. *Chem. Mater.* **2003**, *15*, 4160.
- (27) Areva, S.; Boissiere, C.; Grosso, D.; Asakawa, T.; Sanchez, C.; Linden, M. *Chem. Commun.* **2004**, 1630.
- (28) Zhang, H.; Sun, J.; Ma, D.; Bao, X.; Klein-Hoffmann, A.; Weinberg, G.; Su, D.; Schlogl, R. *J. Am. Chem. Soc.* **2004**, *126*, 7440.
- (29) Suzuki, K.; Ikari, K.; Imai, H. *J. Am. Chem. Soc.* **2004**, *126*, 462.
- (30) Han, Y.; Ying, J. Y. *Angew. Chem. Int. Ed.* **2005**, *44*, 288.
- (31) Ikari, K.; Suzuki, K.; Imai, H. *Langmuir* **2006**, *22*, 802.
- (32) de Zárate, D. O.; Gómez-Moratalla, A.; Guillem, C.; Beltrán, A.; Latorre, J.; Beltrán, D.; Amorós, P. *Eur. J. Inorg. Chem.* **2006**, *2006*, 2572.
- (33) Zhang, H.; Sun, J.; Ma, D.; Weinberg, G.; Su, D. S.; Bao, X. *J. Phys. Chem. B* **2006**, *110*, 25908.
- (34) Yamada, Y.; Yano, K. *Microporous Mesoporous Mater.* **2006**, *93*, 190.
- (35) Shen, S.; Chen, F.; Chow, P. S.; Phanapavudhikul, P.; Zhu, K.; Tan, R. B. H. *Microporous Mesoporous Mater.* **2006**, *92*, 300.
- (36) Garcia-Bennett, A. E.; Lund, K.; Terasaki, O. *Angew. Chem. Int. Ed.* **2006**, *45*, 2434.
- (37) Zhai, S.-R.; Ha, C.-S. *Microporous Mesoporous Mater.* **2007**, *102*, 212.
- (38) Monnier, A.; Schuth, F.; Huo, Q.; Kumar, D.; Margolese, D.; Maxwell, R. S.; Stucky, G. D.; Krishnamurty, M.; Petroff, P.; Firouzi, A.; Janicke, M.; Chmelka, B. F. *Science* **1993**, *261*, 1299.
- (39) Kim, T.-W.; Kleitz, F.; Paul, B.; Ryoo, R. *J. Am. Chem. Soc.* **2005**, *127*, 7601.
- (40) Carlsson, A.; Kaneda, M.; Sakamoto, Y.; Terasaki, O.; Ryoo, R.; Joo, S. H. *J. Electron Microsc.* **1999**, *48*, 795.
- (41) Alfredsson, V.; Anderson, M. W. *Chem. Mater.* **1996**, *8*, 1141.
- (42) Ryoo, R.; Joo, S. H. *Stud. Surf. Sci. Catal.* **2004**, *148*, 241.
- (43) Kim, T.-W.; Solovyov, L. A. *J. Mater. Chem.* **2006**, *16*, 1445.
- (44) Lee, J.; Kim, J.; Hyeon, T. *Adv. Mater.* **2006**, *18*, 2073.
- (45) Bronkema, J. L.; Bell, A. T. *J. Phys. Chem. C* **2007**, *111*, 420.

- (46) Vartuli, J. C.; Schmitt, K. D.; Kresge, C. T.; Roth, W. J.; Leonowicz, M. E.; McCullen, S. B.; Hellring, S. D.; Beck, J. S.; Schlenker, J. L.; Olson, D. H.; Sheppard, E. W. *Chem. Mater.* **1994**, *6*, 2317.
- (47) Schumacher, K.; Gr, M.; Unger, K. K. *Microporous Mesoporous Mater.* **1999**, *27*, 201.
- (48) Schumacher, K.; Ravikovitch, P. I.; Du Chesne, A.; Neimark, A. V.; Unger, K. K. *Langmuir* **2000**, *16*, 4648.
- (49) Sun, J.-H.; Coppens, M.-O. *J. Mater. Chem.* **2002**, *12*, 3016.
- (50) Tian, B.; Liu, X.; Solovyov, L. A.; Liu, Z.; Yang, H.; Zhang, Z.; Xie, S.; Zhang, F.; Tu, B.; Yu, C.; Terasaki, O.; Zhao, D. *J. Am. Chem. Soc.* **2004**, *126*, 865.
- (51) Jiao, F.; Harrison, A.; Jumas, J. C.; Chadwick, A. V.; Kockelmann, W.; Bruce, P. G. *J. Am. Chem. Soc.* **2006**, *128*, 5468.
- (52) Boote, B.; Subramanian, H.; Ranjit, K. T. *Chem. Commun.* **2007**, 4543.
- (53) Auvray, X.; Petipas, C.; Anthore, R.; Rico, I.; Lattes, A. *J. Phys. Chem.* **1989**, *93*, 7458.
- (54) Huo, Q.; Margolese, D. I.; Stucky, G. D. *Chem. Mater.* **1996**, *8*, 1147.
- (55) Liu, S. Q.; Cool, P.; Collart, O.; Van der Voort, P.; Vansant, E. F.; Lebedev, O. I.; Van Tendeloo, G.; Jiang, M. H. *J. Phys. Chem. B* **2003**, *107*, 10405.
- (56) Tan, B.; Rankin, S. E. *J. Phys. Chem. B* **2004**, *108*, 20122.
- (57) Yu, J.; Shi, J.-L.; Wang, L.-Z.; Gao, J.-H.; Yan, D.-S. *J. Mater. Sci. Lett.* **2000**, *19*, 1461.
- (58) Choma, J.; Pikus, S.; Jaroniec, M. *Appl. Surf. Sci.* **2005**, *252*, 562.
- (59) Kruk, M.; Jaroniec, M.; Ryoo, R.; Joo, S. H. *Chem. Mater.* **2000**, *12*, 1414.
- (60) Kim, T.-W.; Chung, P.-W.; Slowing, I. I.; Tsunoda, M.; Yeung, E. S.; Lin, V. S.-Y. *Nano Lett.* **2008**, submitted.
- (61) Kang, M.; Kim, D.; Yi, S. H.; Han, J. U.; Yie, J. E.; Kim, J. M. *Catal. Today* **2004**, *93-95*, 695.

Tables

Table 1. Structural parameters of the 3-D cubic $Ia-3d$ MCM-48 MSNs synthesized using different alkyl chain length surfactants and post-hydrothermal treatment.

Sample	a (nm)	S_{BET} ($\text{m}^2 \text{g}^{-1}$)	V_t ($\text{cm}^3 \text{g}^{-1}$)	w_{BJH} (nm)	d (nm)
CTAB-RT	8.07	1248	0.96	2.3	1.45
CTAB-423 K	10.3	994	1.00	3.3	1.72
OTAB-RT	8.36	1258	1.03	2.4	1.50
OTAB-403 K	9.83	1116	1.11	3.1	1.64

a , XRD unit cell parameter equals to $6^{1/2}d_{211}$; S_{BET} , apparent BET specific surface area deduced from the isotherm analysis in the relative pressure range from 0.05 to 0.20; V_t , total pore volume at relative pressure 0.95; w_{BJH} , the pore diameter calculated using the BJH method. d , wall thickness evaluated by $d = a/3.092 - w_{\text{BJH}}/2$.⁴⁸ The sample notations of CTAB-RT and CTAB-423 K mean MSNs are synthesized using CTAB at room temperature and CTAB with post-hydrothermal treatment at 423 K for 2 d, respectively. (see Figure 9 for the synthesis molar ratios)

Figure 1. Powder XRD patterns for the calcined mesoporous silica materials obtained using magnetic stirrer with different stirring rate for 4 h, and x TEOS: $12.5 \times y$ NH_3 : $54 \times y$ EtOH: 0.4 CTAB: $417 \times y$ H_2O . The molar ratio of TEOS (x) and diluted times (y) were (x, y) = (a) (1.0, 1) and (b) (2.5, 4).

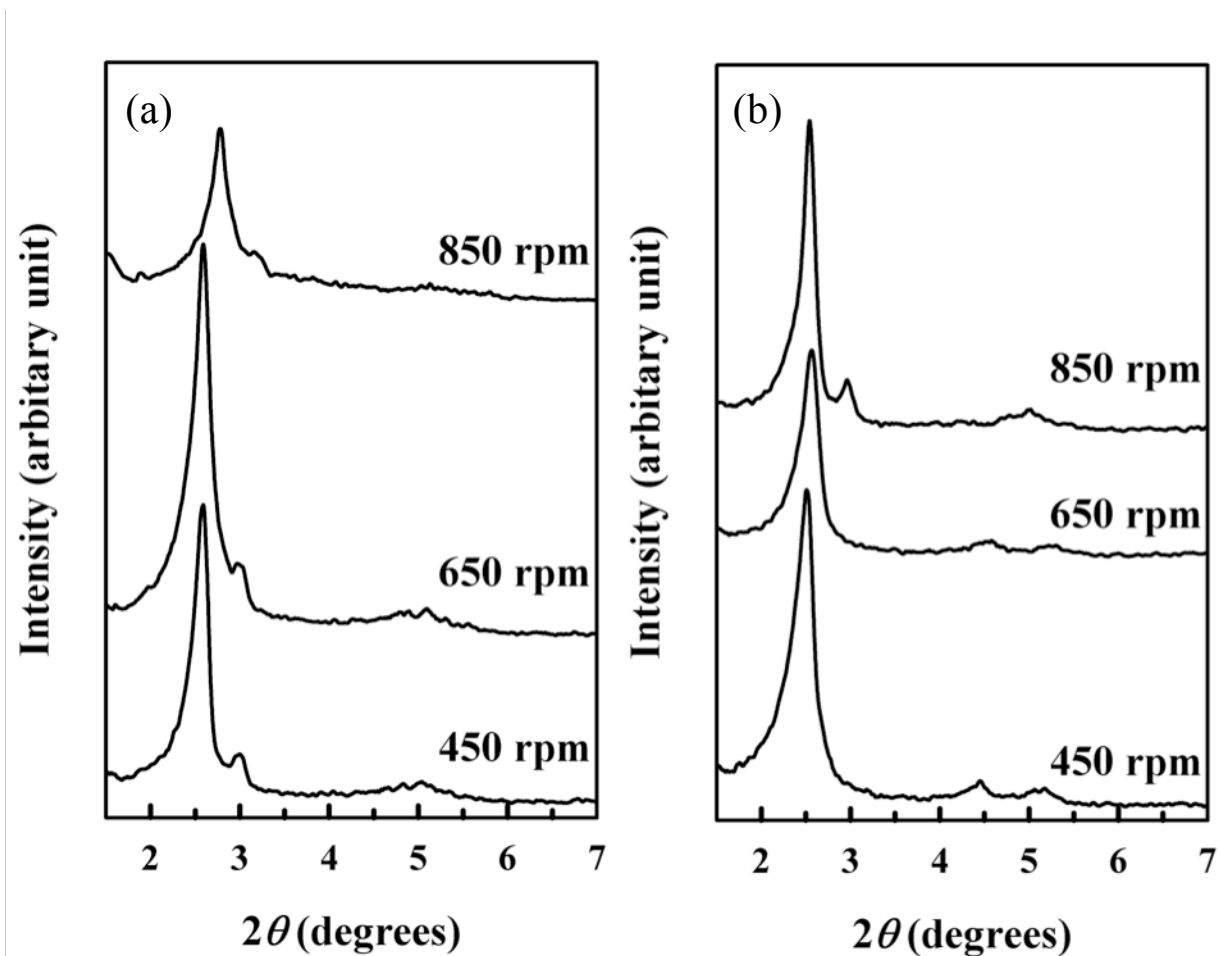


Figure 2. Phase diagram of mesophase structures established according to the XRD measurements. Each sample is prepared with a molar ratio of x TEOS: $12.5 \times y$ NH_3 : $54 \times y$ EtOH: 0.4 CTAB: $417 \times y$ H_2O and stirring rate at 850 rpm for 4 h.

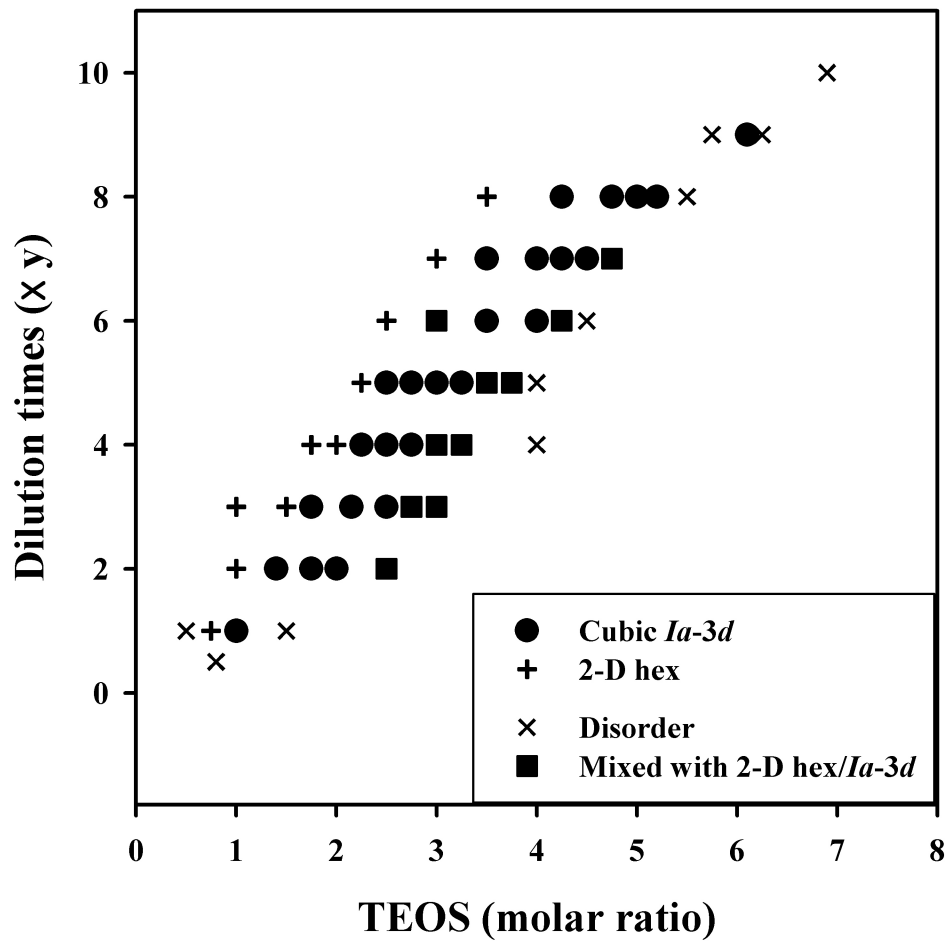


Figure 3. Powder XRD patterns for the calcined cubic $Ia-3d$ mesoporous MCM-48 silicas. Each sample was prepared as the molar ratio of x TEOS: $12.5 \times y$ NH_3 : $54 \times y$ EtOH: 0.4 CTAB: $417 \times y$ H_2O : $x, y =$ (a) 1.0, 1 (b) 1.4, 2, (c) 2.5, 4, (d) 4.0, 6, and (e) 5.2, 8.

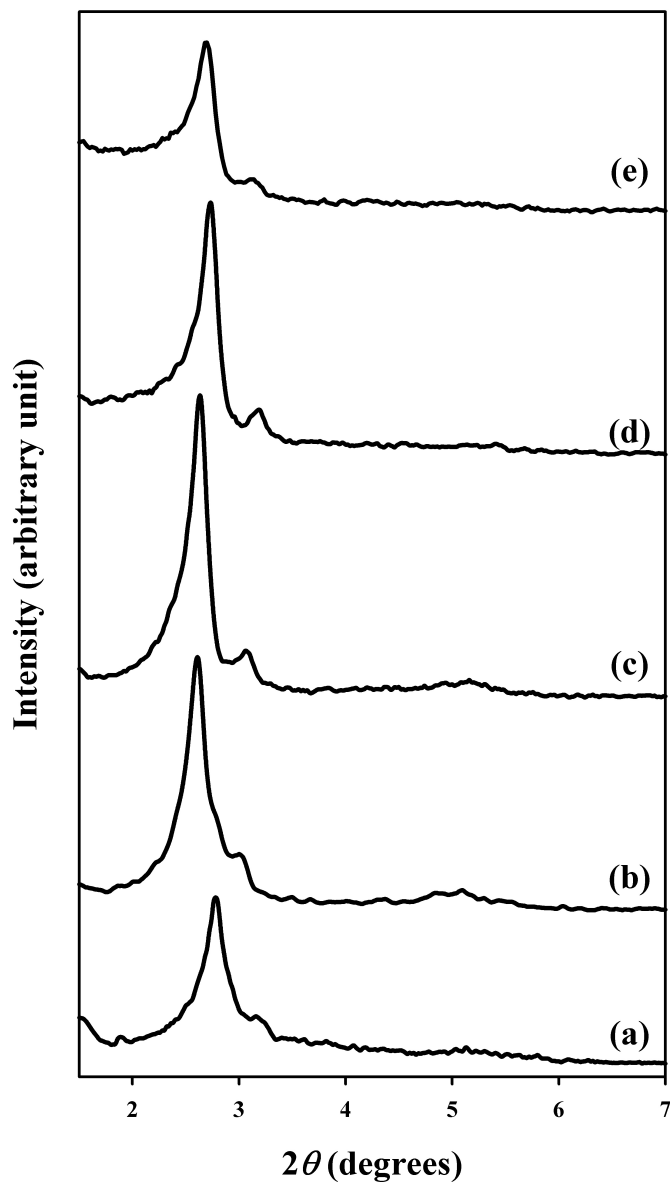


Figure 4. Powder XRD patterns for the calcined cubic $Ia-3d$ mesoporous MCM-48 silicas. Each sample was prepared as the molar ratio of 2.5 TEOS: 50 NH_3 :216 EtOH: 0.4 CTAB: 1668 H_2O . (a) Samples were obtained by different stirring time at 1000 rpm and aged 24 h, and (b) stirring for 1 min at 1000 rpm and different aging time.

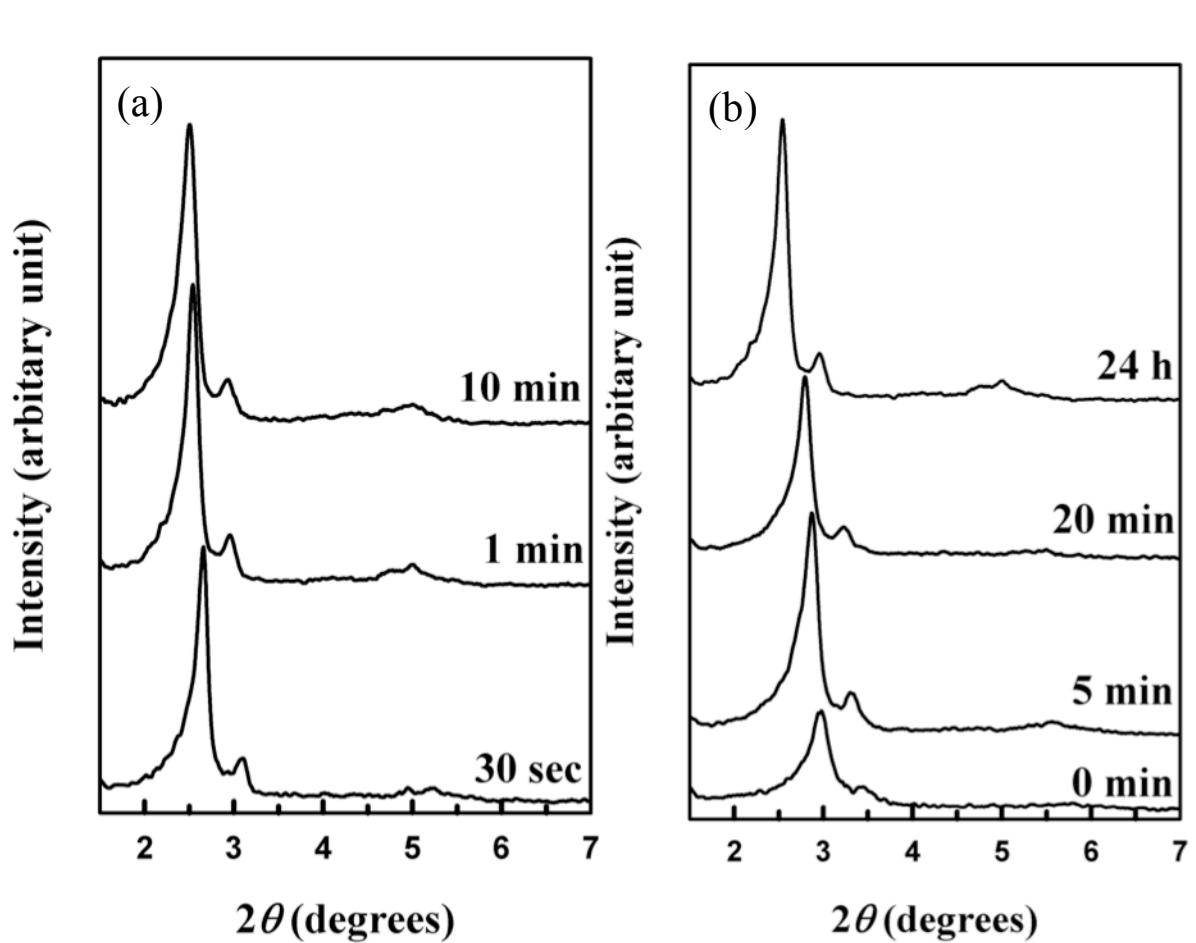


Figure 5. TEM images for calcined cubic *Ia-3d* MCM-48 mesoporous silica nanoparticles with different amount of the F127 under diluted CTAB concentration. F127 (in molar ratio) = (a) 0, (b) 0.047, (c) 0.078, and (d) 0.094.

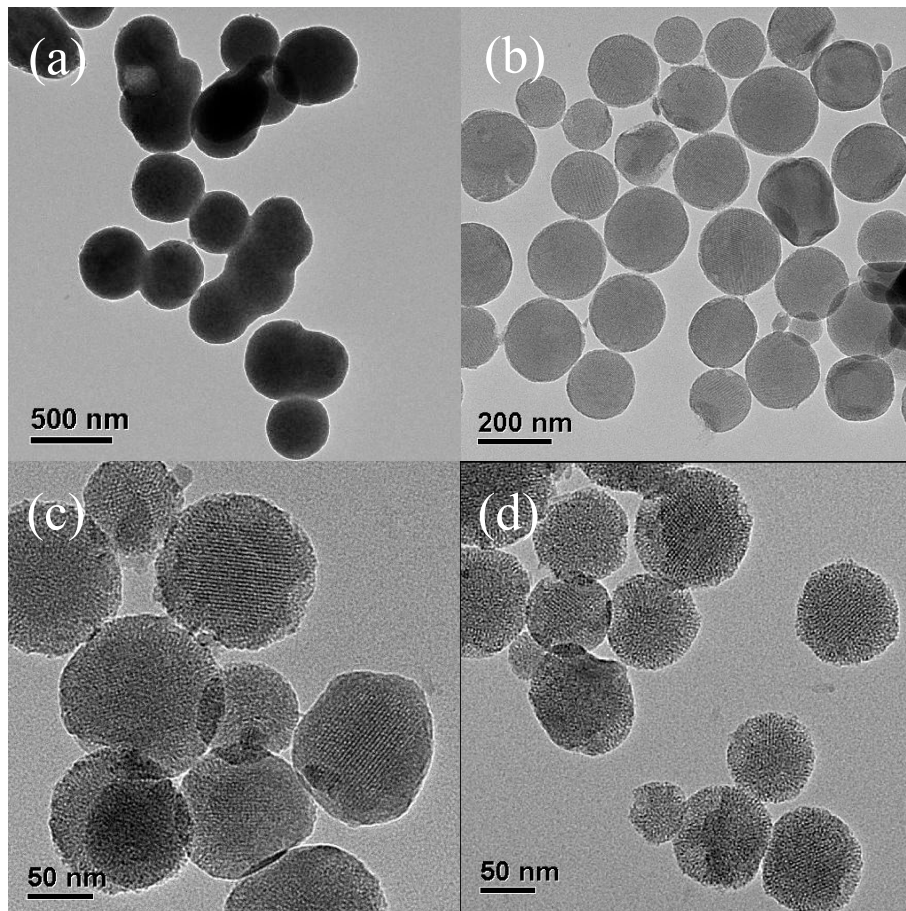


Figure 6. Powder XRD patterns (left) and nitrogen adsorption-desorption isotherm (right) for the calcined cubic *Ia-3d* mesoporous MCM-48 silicas. Each sample was prepared as the molar ratio of 2.5 TEOS: 50 NH₃:216 EtOH: 0.4 CTAB: 1668 H₂O: *x* F127: *x* = (a) 0.016, (b) 0.031, (c) 0.047, (d) 0.063, (e) 0.078, and (f) 0.094. The isotherms for (b), (c), (d), (e), and (f) samples are offset vertically by 200, 400, 600, 950 and 1200 cm³ STP g⁻¹, respectively.

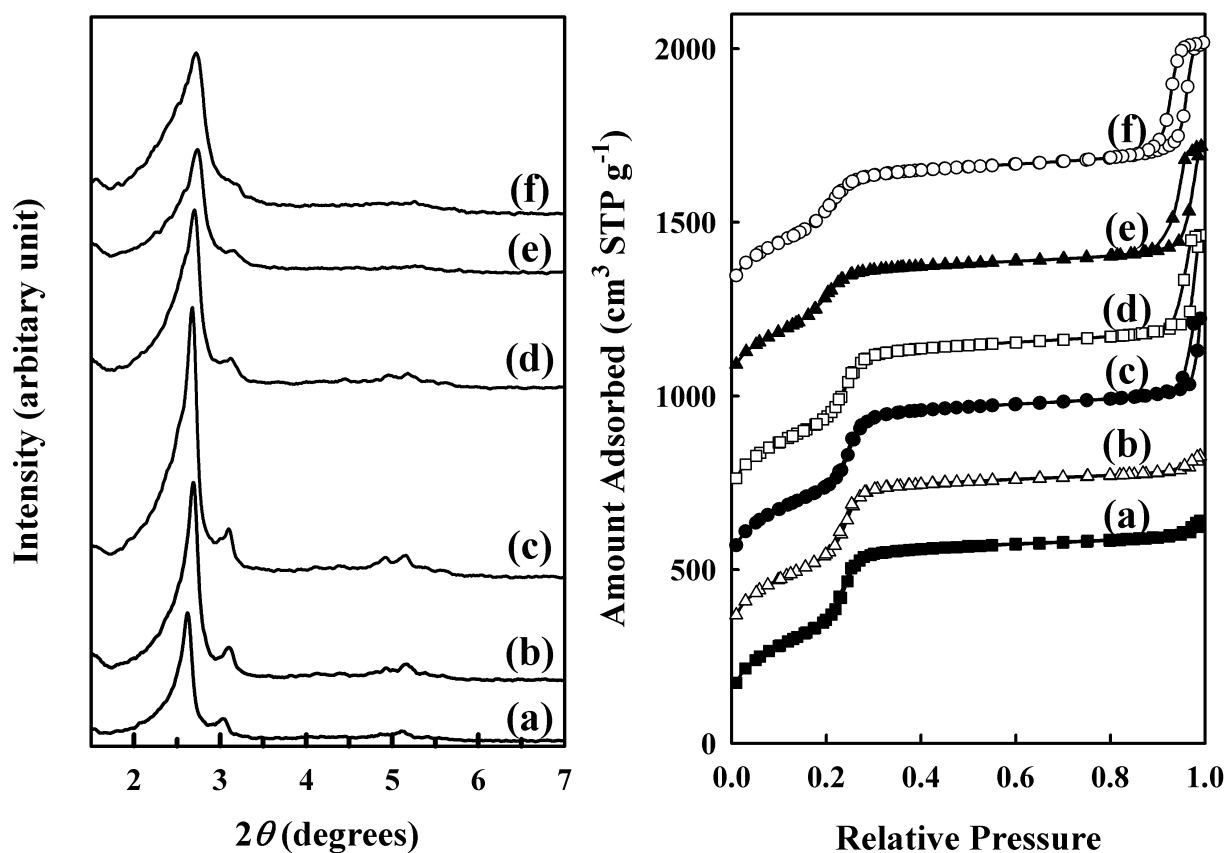


Figure 7. Powder XRD patterns for the as-synthesized (left) and calcined (right) cubic $Ia-3d$ mesoporous MCM-48 silicas using OTAB surfactant as a structure-directing agent. Each sample was prepared as the molar ratio of x TEOS: 50 NH_3 :216 EtOH: 0.4 OTAB: 1668 H_2O : $x =$ (a) 2.5 (b) 2.0, and (c) 1.75.

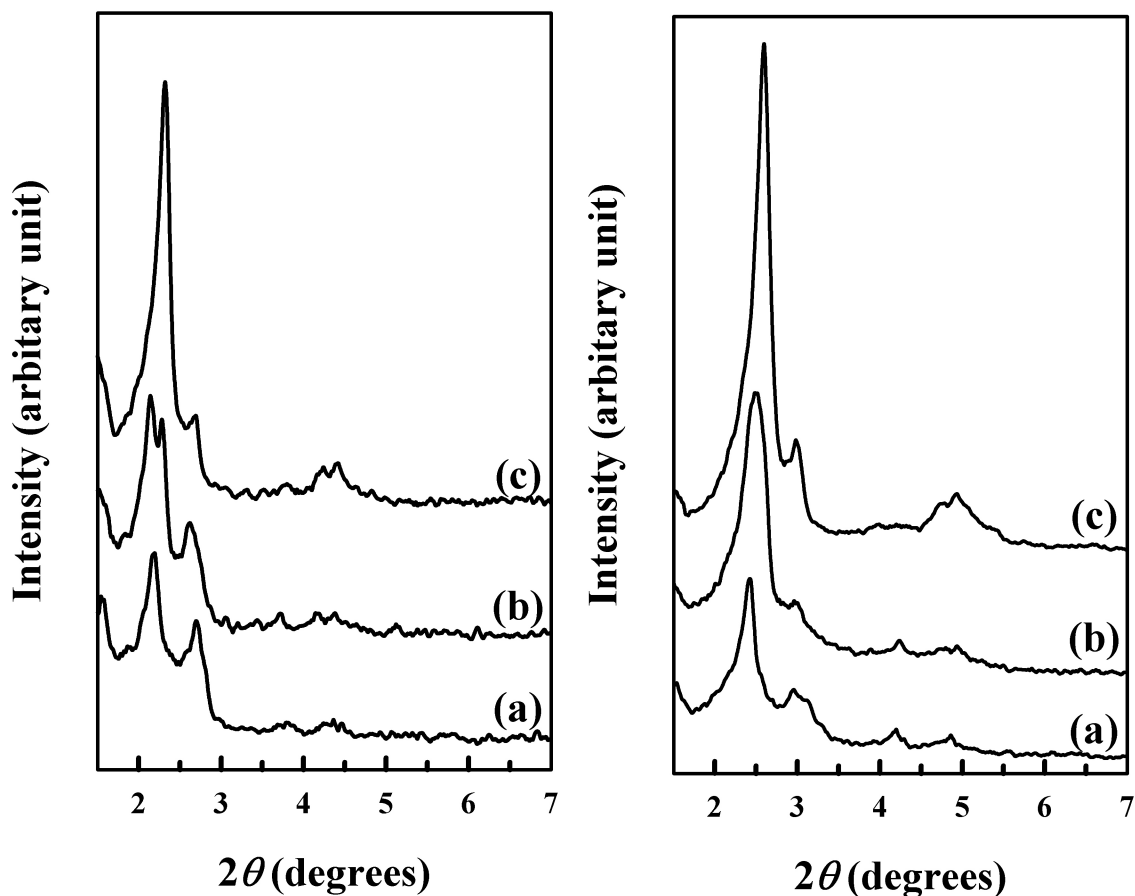


Figure 8. TEM images for the calcined cubic Ia-3d mesoporous MCM-48 silicas using OTAB surfactant as a structure-directing agent. Each sample was prepared as the molar ratio of 1.75 TEOS: 50 NH₃:216 EtOH: 0.4 OTAB: 1668 H₂O: x F127: x = (A) 0, (B) 0.016, (C) 0.031, and (D) 0.047.

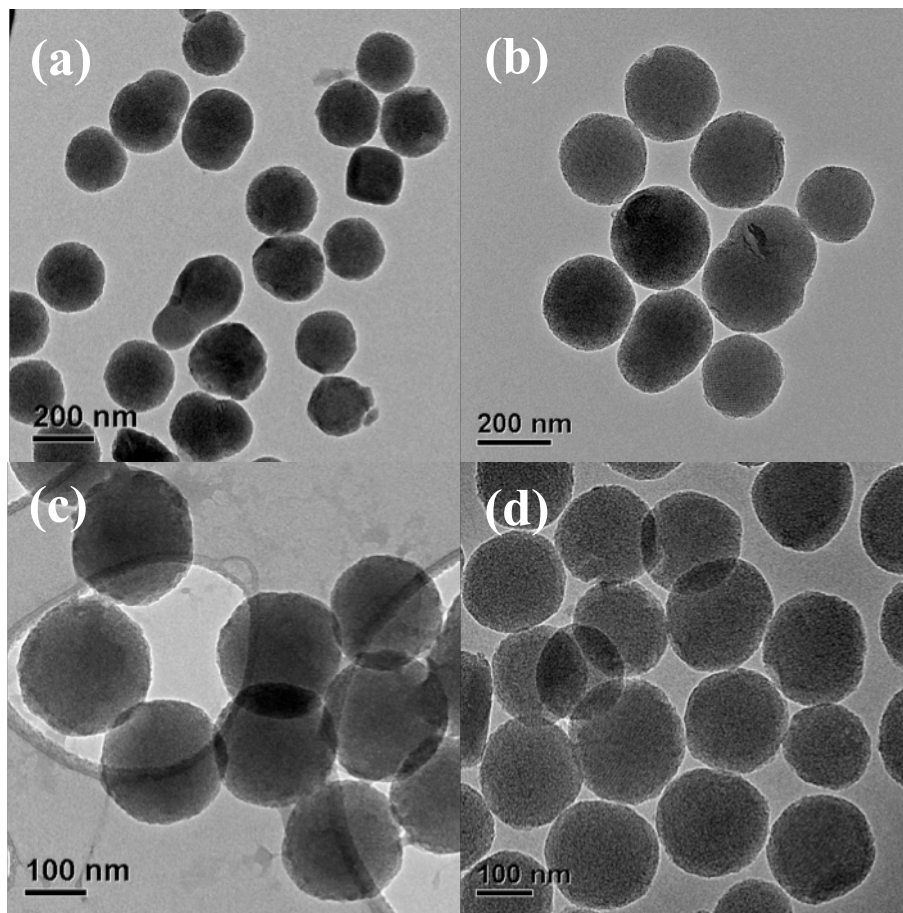


Figure 9. Powder XRD patterns for the calcined cubic *Ia-3d* mesoporous MCM-48 silicas synthesized with different temperature. The samples, (a), and (b) were prepared as the molar ratio of 2.5 TEOS: 50 NH₃:216 EtOH: 0.4 CTAB: 1668 H₂O: 0.047 F127, and (d) and (e) synthesized 1.75 TEOS: 50 NH₃:216 EtOH: 0.4 OTAB: 1668 H₂O: 0.031 F127. The samples (a) and (c) were synthesized at room temperature. The samples (b), and (d) were hydrothermally treated at 423 K and 403 K for 2 days, respectively.

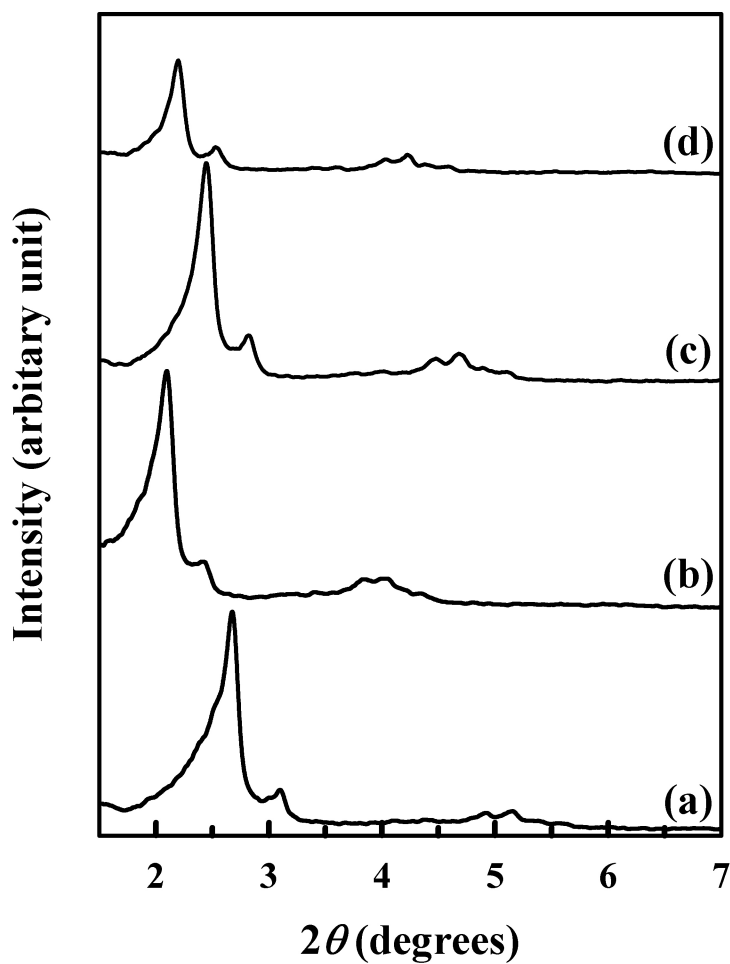


Figure 10. Nitrogen adsorption-desorption isotherm (left) and pore size distributions (right) for the calcined cubic *Ia-3d* mesoporous MCM-48 mesoporous silicas synthesized at different temperatures. The isotherms for (b), (c), and (d) samples are offset vertically by 300, 500, and 900 $\text{cm}^3 \text{STP g}^{-1}$, respectively. The pore size was analyzed with the adsorption branch using the BJH algorithm (see Figure 8 for sample composition).

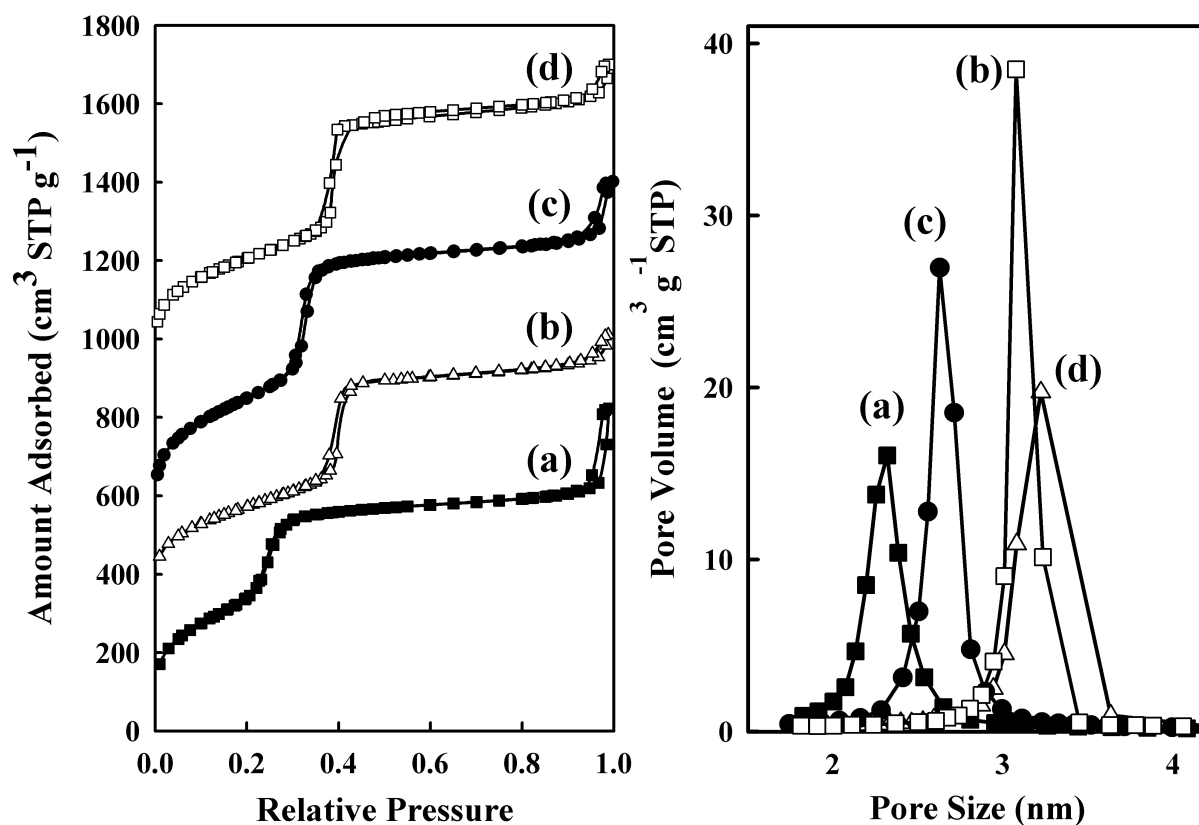
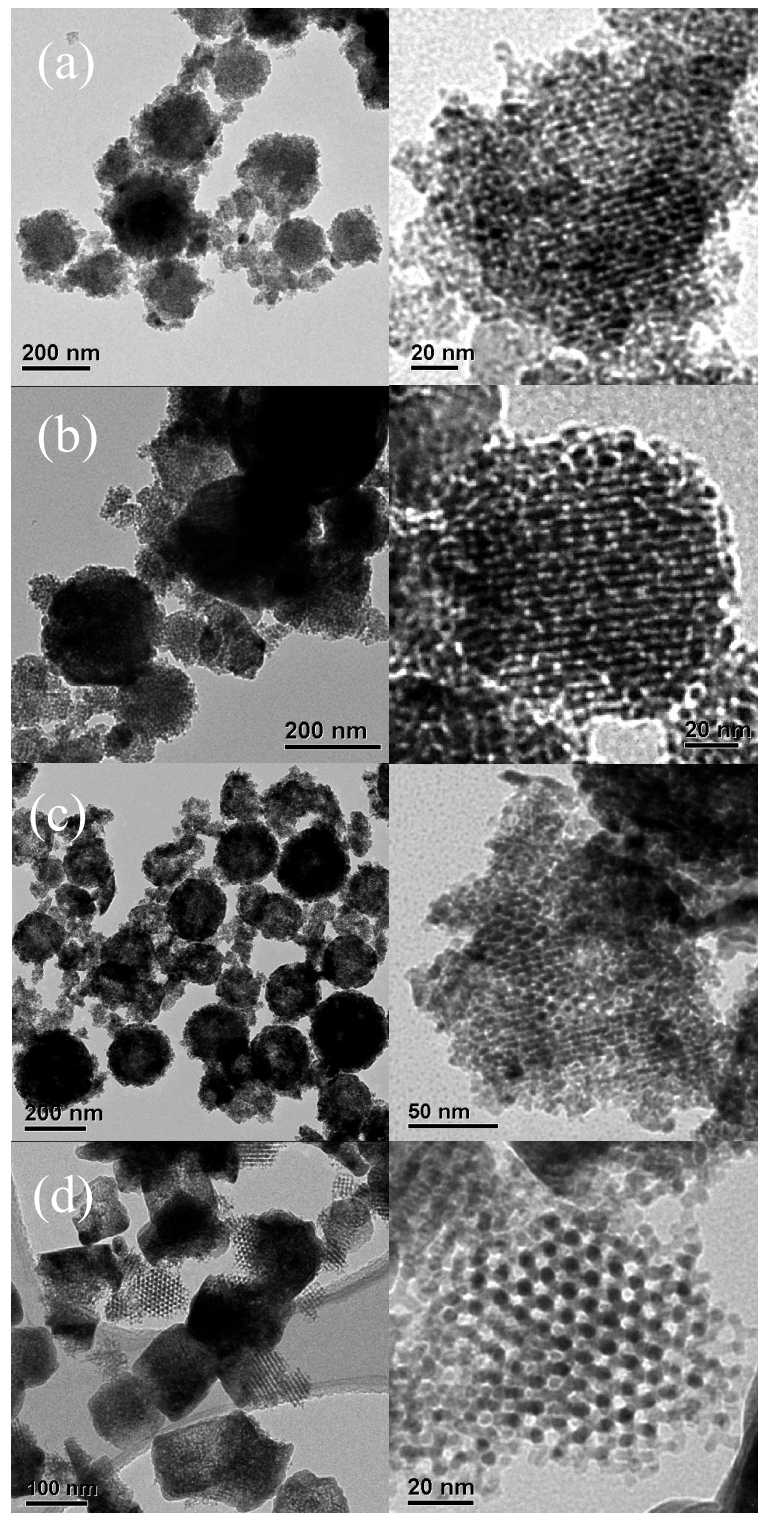


Figure 11. TEM images of (a) Fe_2O_3 ; (b) Co_3O_4 ; (c) CeO_2 and (d) In_2O_3



Supporting Information

Table S1. Structural parameters of the cubic $Ia-3d$ mesoporous silicas which were prepared as the molar ratio of x TEOS: $12.5 \times y$ NH_3 : $54 \times y$ EtOH: 0.4 CTAB: $417 \times y$ H_2O : $x, y = ()$ 1.0, 1 (b) 1.4, 2, (c) 2.5, 4, (d) 4.0, 6, and (e) 5.2, 8.

Sample	a (nm)	S_{BET} ($\text{m}^2 \text{g}^{-1}$)	V_t ($\text{cm}^3 \text{g}^{-1}$)	w_{BJH} (nm)	d (nm)
(a)	7.78	1385	0.91	2.5	1.23
(b)	8.26	1366	0.89	2.6	1.39
(c)	8.20	1495	0.90	2.3	1.53
(d)	7.96	1331	0.72	2.4	1.39
(e)	8.01	1062	0.71	2.3	1.43

a , XRD unit cell parameter equals to $6^{1/2}d_{211}$; S_{BET} , apparent BET specific surface area deduced from the isotherm analysis in the relative pressure range from 0.05 to 0.20; V_t , total pore volume at relative pressure 0.95; w_{BJH} , the pore diameter calculated using the BJH method. d , wall thickness evaluated by $d = a/3.092 - w_{\text{BJH}}/2$.

Table S2. Structural parameters of the cubic *Ia-3d* mesoporous silicas which were prepared as the molar ratio of 2.5 TEOS: 50 NH₃:216 EtOH: 0.4 CTAB: 1668 H₂O: *x* F127: *x* = (a) 0.016, (b) 0.031, (c) 0.047, (d) 0.063, (e) 0.078, and (f) 0.094.

Sample	<i>a</i> (nm)	<i>S</i> _{BET} (m ² g ⁻¹)	<i>V</i> _t (cm ³ g ⁻¹)	<i>w</i> _{BJH} (nm)	<i>d</i> (nm)
(a)	8.25	1302	0.93	2.3	1.53
(b)	8.04	1260	0.91	2.3	1.47
(c)	8.07	1248	0.96	2.3	1.45
(d)	8.00	1266	0.94	2.3	1.46
(e)	7.89	1288	0.77	2.2	1.43
(f)	7.95	1267	0.85	2.2	1.45

a, XRD unit cell parameter equals to $6^{1/2}d_{211}$; *S*_{BET}, apparent BET specific surface area deduced from the isotherm analysis in the relative pressure range from 0.05 to 0.20; *V*_t, total pore volume at relative pressure 0.95; *w*_{BJH}, the pore diameter calculated using the BJH method. *d*, wall thickness evaluated by $d = a/3.092 - w_{BJH}/2$.

Table S3. Structural parameters of the cubic *Ia-3d* mesoporous silicas which were prepared as the molar ratio of 1.75 TEOS: 50 NH₃:216 EtOH: 0.4 OTAB: 1668 H₂O: *x* F127: *x* = (a) 0, (b) 0.016, (c) 0.031, and (d) 0.047.

Sample	<i>a</i> (nm)	<i>S</i> _{BET} (m ² g ⁻¹)	<i>V</i> _t (cm ³ g ⁻¹)	<i>w</i> _{BJH} (nm)	<i>d</i> (nm)
(a)	8.36	1258	1.03	2.4	1.50
(b)	8.72	1272	1.15	2.6	1.50
(c)	8.79	1286	1.18	2.6	1.53
(d)	8.71	1280	1.17	2.6	1.50

a, XRD unit cell parameter equals to $6^{1/2}d_{211}$; *S*_{BET}, apparent BET specific surface area deduced from the isotherm analysis in the relative pressure range from 0.05 to 0.20; *V*_t, total pore volume at relative pressure 0.95; *w*_{BJH}, the pore diameter calculated using the BJH method. *d*, wall thickness evaluated by $d = a/3.092 - w_{BJH}/2$.

Table S4. Structural parameters of the mesoporous metal oxide nanoparticles.

Sample	S_{BET} ($\text{m}^2 \text{g}^{-1}$)	V_t ($\text{cm}^3 \text{g}^{-1}$)	w_{BJH} (nm)
Fe_2O_3	213	0.32	5.3
Co_3O_4	142	0.15	4.8
CeO_2	139	0.21	6.3
In_2O_3	49	0.09	5.9

S_{BET} , apparent BET specific surface area deduced from the isotherm analysis in the relative pressure range from 0.05 to 0.20; V_t , total pore volume at relative pressure 0.95; w_{BJH} , the pore diameter calculated using the BJH method.

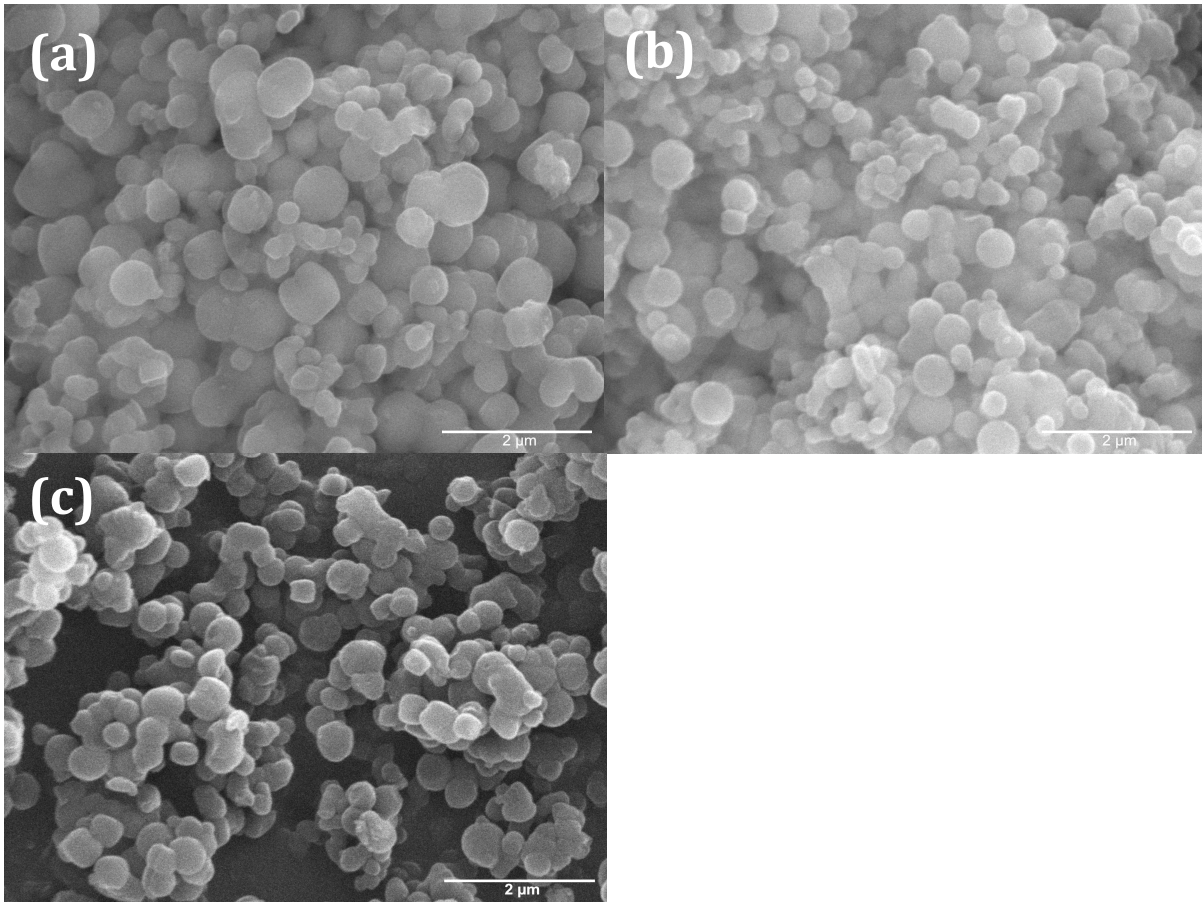


Figure S1. SEM images of the calcined mesoporous silica materials obtained using magnetic stirrer with different stirring rate, and 1 TEOS: 12.5 NH_3 : 54 EtOH: 0.4 CTAB: 417 H_2O . The stirring rate is varied: (a) 450 rpm, (b) 650 rpm, and (c) 850 rpm.

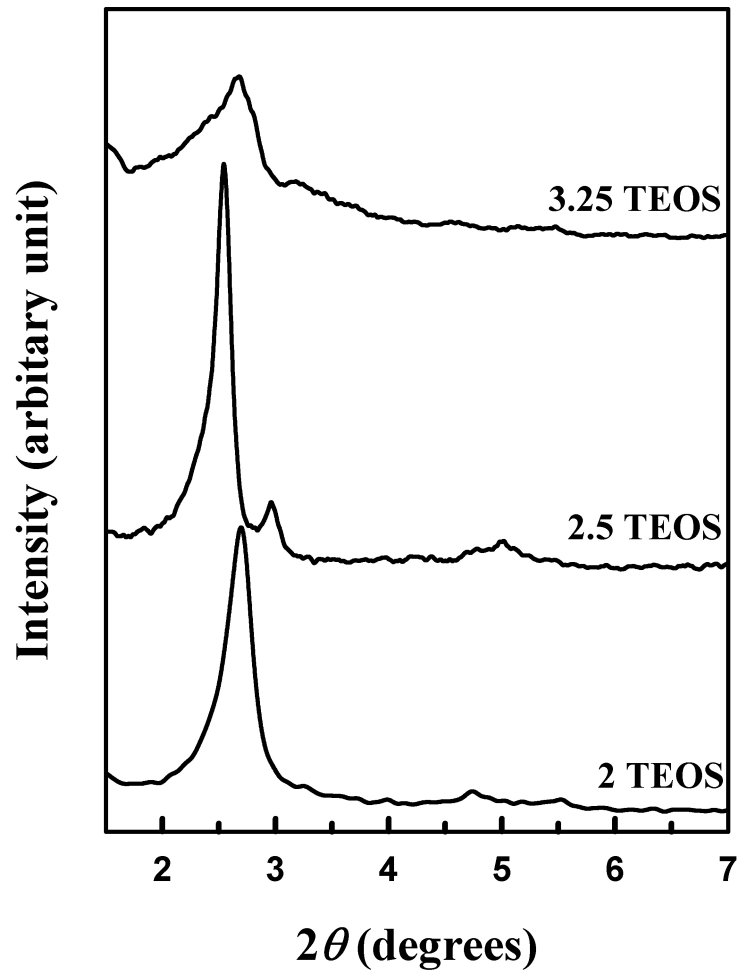


Figure S2. Powder XRD patterns for the calcined mesoporous silica materials obtained under 4 times dilution condition using magnetic stirrer at 850 rpm for 4h with different TEOS molar ratio. The molar ratio of TEOS was varied with 2~3.25.

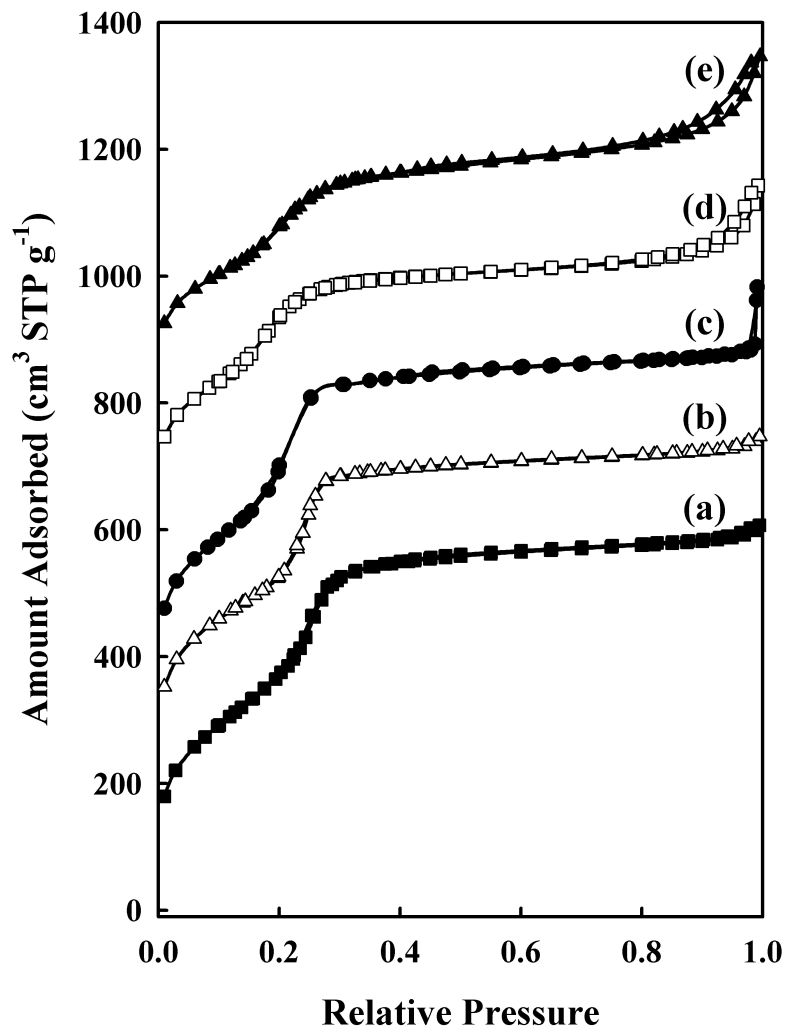


Figure S3. Nitrogen adsorption-desorption isotherm for the mesostructured silica materials obtained using x TEOS: $12.5 \times y$ NH_3 : $54 \times y$ EtOH: 0.4 CTAB: $417 \times y$ H_2O : $x, y =$ (a) 1.0, 1 (b) 1.4, 2, (c) 2.5, 4, (d) 4.0, 6, and (e) 5.2, 8. The isotherms for (b), (c), (d), and (e) samples are offset vertically by 150, 300, 600, and 800 $\text{cm}^3 \text{STP g}^{-1}$, respectively

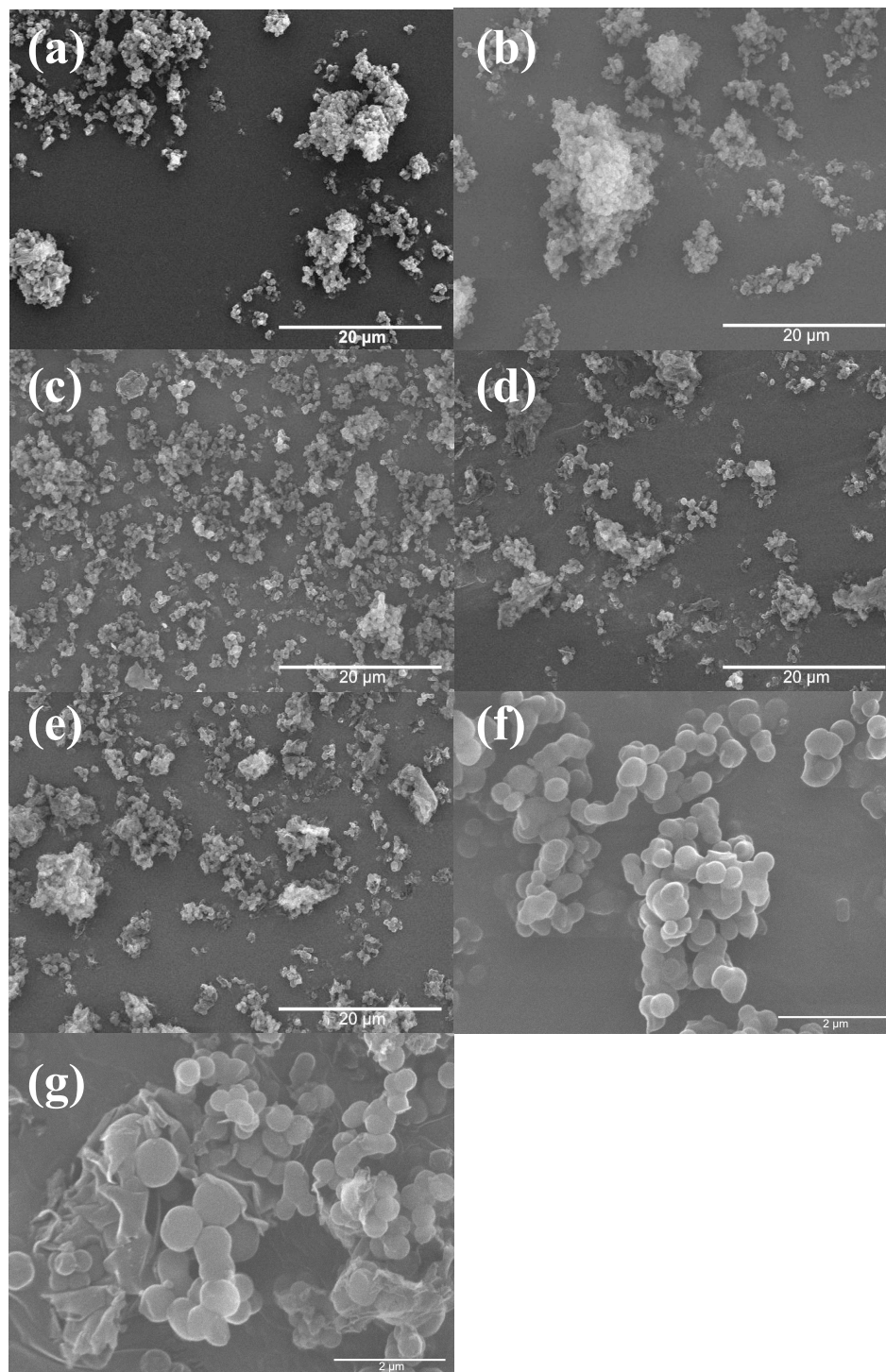


Figure S4. SEM images of the calcined mesoporous silica materials obtained using magnetic x TEOS: $12.5 \times y$ NH_3 : $54 \times y$ EtOH: 0.4 CTAB: $417 \times y$ H_2O : $x, y =$ (a) 1.0, 1 (b) 1.4, 2, (c)

2.5, 4, (d) 4.0, 6, and (e) 5.2, 8. High magnified SEM images for $x, y =$ (f) 2.5, 4 and (g) 5.2, 8.

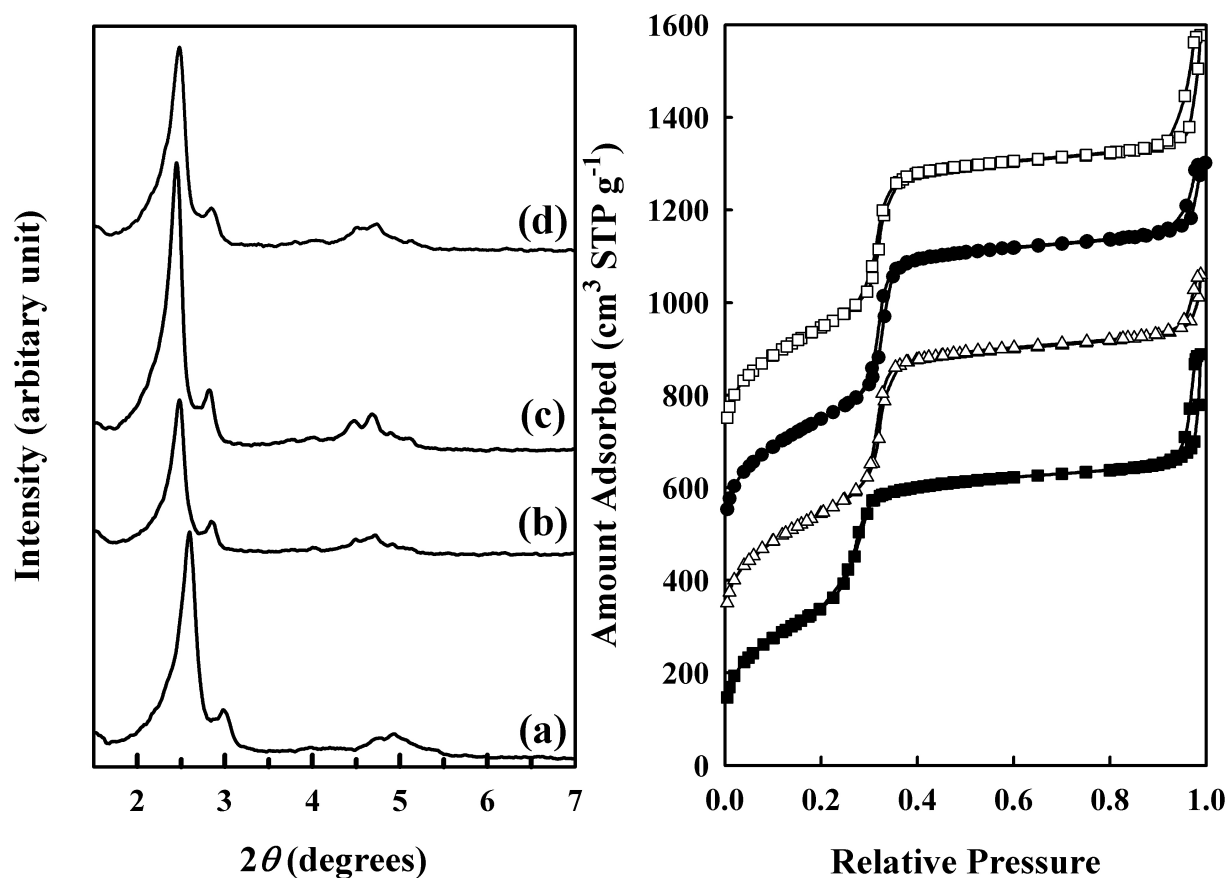


Figure S5. Powder XRD patterns (left) and nitrogen adsorption-desorption isotherm (right) for the calcined cubic Ia-3d mesoporous MCM-48 silicas. Each sample was prepared as the molar ratio of 1.75 TEOS: 50 NH₃:216 EtOH: 0.4 OTAB: 1668 H₂O: x F127: $x =$ (a) 0, (b) 0.016, (c) 0.031, and (d) 0.047. The isotherms for (b), (c), and (d) samples are offset vertically by 300, 500, and 900 cm³ STP g⁻¹, respectively.

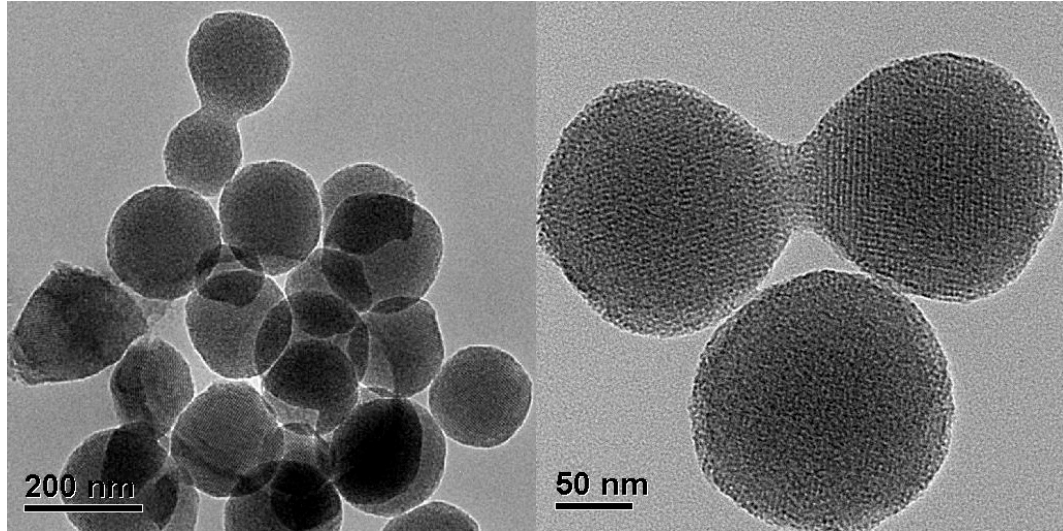


Figure S6. TEM images for the calcined cubic *Ia-3d* mesoporous MCM-48 MSN after post-hydrothermal treatment at 423 for 2 days. The sample was prepared as the molar ratio of 2.5 TEOS: 50 NH₃:216 EtOH: 0.4 CTAB: 1668 H₂O: 0.047 F127.

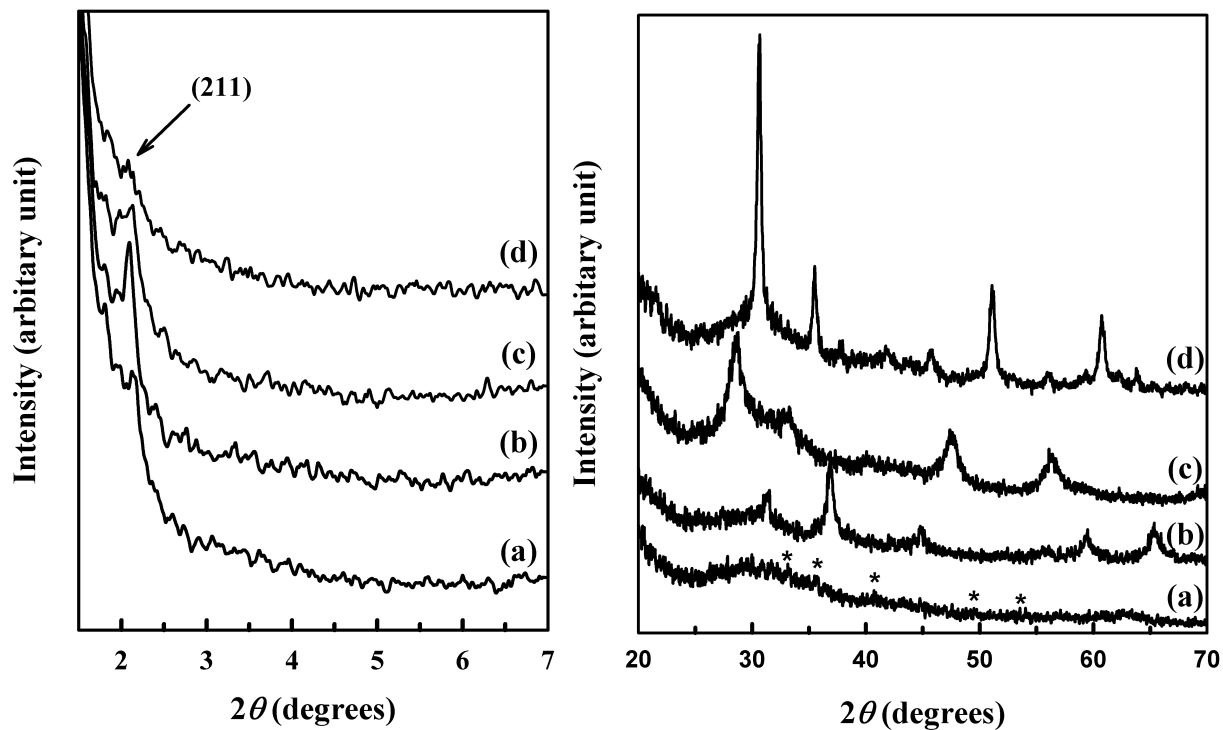


Figure S7. Low angle (left) and wide angle (right) XRD patterns for the mesoporous metal oxide materials: (a) Fe_2O_3 , (b) Co_3O_4 , (c) CeO_2 , and (d) In_2O_3 . The asterisks marks are characteristic peaks of Fe_2O_3 .

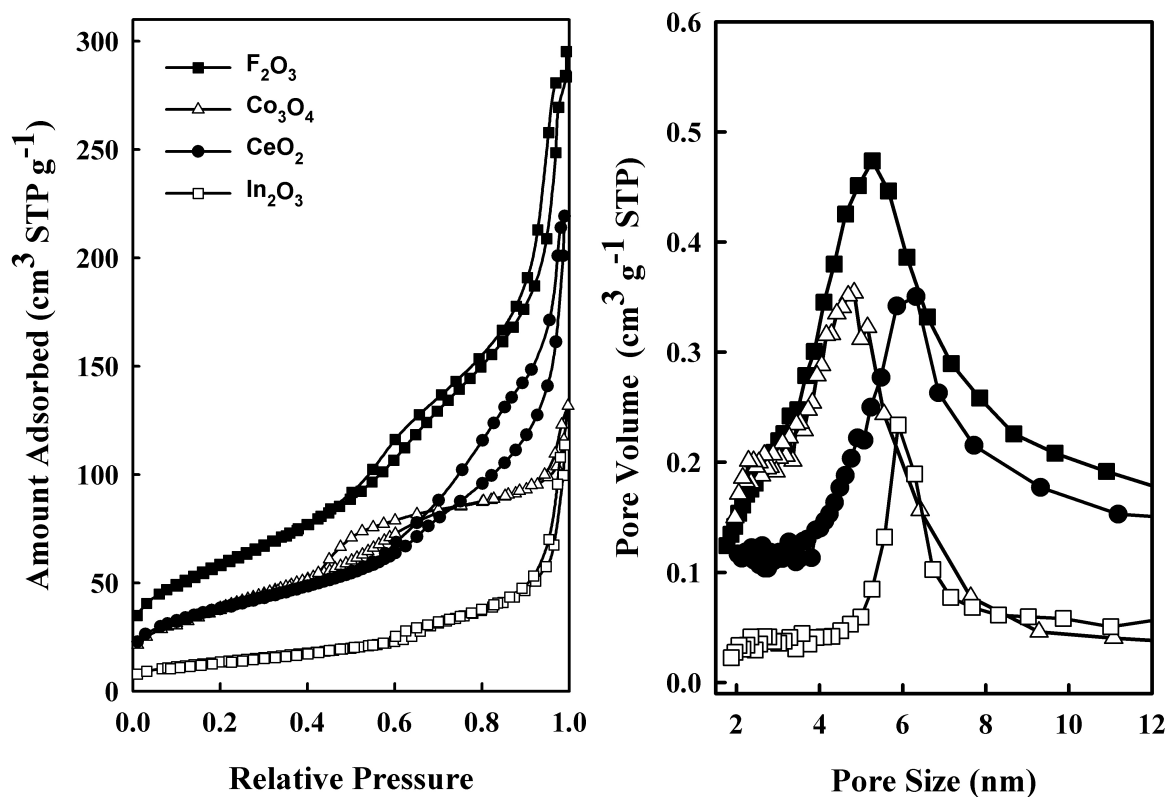


Figure S8. Nitrogen adsorption-desorption isotherm (left) and corresponding pore size distributions (right) for the mesoporous metal oxide materials. The pore size was analyzed with the adsorption branch using the BJH algorithm.

CHAPTER 6. GENERAL CONCLUSIONS

The research work I have accomplished since early 2005 was presented in this dissertation. The early goal of my research is selectively functionalize organic moiety on the exterior surface of mesoporous silica materials and to control the chemical properties of nanoparticles. As demonstrated in Chapter 2., the successful synthesis and characterization of a series of poly(*N*-isopropylacrylamide)-coated mesoporous silica nanoparticle materials were presented. We discovered that the surface-initiated RAFT polymerization of NiPAm on the MSN surface could be controlled and the degree of polymerization could also be tuned. In addition, we found that the thermally induced conformational changes of NiPAm polymer layer indeed altered the surface properties of these organic-inorganic hybrid nanoparticles, as manifested by the temperature dependent solution partition behavior of these core-shell materials in a biphasic toluene/ water solution.

In addition to the MCM-41 type mesoporous silica nanoparticles (MSNs), we also developed the facile synthesis of MSNs with different mesostructure. The preparation of monodisperse spherical MCM-48 mesoporous nanoparticles with 3-D cubic *Ia-3d* mesostructure, which is based on the modified Stöber method, is easy and highly reproducible. The synthesis is simply carried out by mechanical stirring of the basic surfactant template solution at 1000 rpm for 1 min at room temperature after addition of silica source. This method, kinetically controlled phase transformation by high stirring rate under low surfactant/silicon ratio, has become possible to synthesize the cubic *Ia-3d* mesophase in a wide range of mixture composition, and gives synthetic phase diagram in the function of surfactant concentration and amount of silicon source. Most importantly, monodisperse spherical MCM-48 MSN with a precise control of the particle size was easily

achieved by using triblock copolymer Pluronic F127 as a dispersant agent. In addition, the pore diameter of MCM-48 MSNs could be tunable using different alkyl chain surfactant and simple post-hydrothermal treatment. The MCM-48-type MSNs with tailored structural properties thus obtained can be used a versatile hard template for preparation of non-siliceous mesoporous nanoparticles such as metal, metal oxides, carbons, and polymers.

Apart from mesoporous silica materials, we also have demonstrated that a structurally stable mesoporous carbon nanoparticle (MCN) material with high surface area and defined particle and pore morphology could be successfully synthesized via nanocasting of MCM-48 nanoparticles. We discovered that this carbonaceous nanoparticle material could efficiently penetrate the plasmic membrane of live HeLa cells with low cytotoxicity. MCN nanoparticles could also serve as effective transmembrane delivery carriers for intracellular release of a cell-membrane impermeable dye and it will open a new horizon for a variety of biotechnological and biomedical applications.

As well as the demonstration of the biocompatibility, MCNs have been successfully employed as a catalytic support for CO hydrogenation and exhibited interesting effect on catalytic performance. Owing to the unique mesoporosity, catalytic metal particles were highly distributed over MCN and Rh-Mn/MCN might be able to suppress methane production on CO hydrogenation at higher reaction temperature. In order to study the impact of mesostructures, the reactivity and selectivity of CO hydrogenation on Rh-supported mesoporous carbon materials with different porous structures such as CMK-3, CMK-5 and CMK-8 will be continuously investigated in the near future.

Very recently, we developed mesoporous polymer-based materials possessing highly ordered mesoporous structure and were employed as a new drug delivery system. For instance, mesoporous poly(methacrylic acid)-based nanoparticles (MPNs) exhibited higher loading of Doxorubicin (Dox) than MSN and amorphous poly(methacrylic acid) owing to the abundant carboxylic acids well-distributed on the ordered porous surface. Furthermore, we also demonstrated that MPNs were able to deliver Dox into cancer cell via endocytosis and release the cargo inside the target cell. In order to open a whole new horizon, we believed we are able to modify the synthesis and create the biodegradable mesoporous materials in the near future. Therefore, I can essentially conclude that the nanomaterials I have reported in this dissertation are able to successfully provide a whole new platform of drug delivery application and catalyst support.

ACKNOWLEDGEMENTS

I would like to take this opportunity to express my thanks to those who helped me with various aspects of conducting research and the writing of this thesis. First and foremost, I would like to appreciate my major professor, Dr. Lin with all his guidance, patience and support throughout this research and the writing of this thesis. His insights and words of encouragement have often inspired me and renewed my hopes for completing my graduate education. I would also like to thank my committee members for their efforts and contributions to this work: Dr. Pruski, Dr. Kraus, Dr. Sadow and Dr. Kramer, who helped me a lot on TEM.